
Numerical Analysis of Tangential Slot Blowing on a Generic Chined Forebody

Roxana M. Agosta

September 1994



National Aeronautics and
Space Administration

Numerical Analysis of Tangential Slot Blowing on a Generic Chined Forebody

Roxana M. Agosta, Ames Research Center, Moffett Field, California

September 1994



National Aeronautics and
Space Administration

Ames Research Center
Moffett Field, California 94035-1000

Contents

	Page
List of Tables and Figures	v
Nomenclature	vii
Summary	1
1. Introduction	1
2. Governing Equations	2
Coordinate Transformation	3
Thin-Layer Approximation	5
Turbulence Modeling	6
Baldwin–Lomax turbulence model	6
Degani–Schiff modifications	7
3. Numerical Methods	8
Implicit Method and Time Linearization	8
Beam and Warming Algorithm	8
Flux Vector Splitting.....	9
Numerical Dissipation	10
Numerical Algorithm	10
Chimera Approach	10
4. Grid Generation Procedure and Boundary Conditions	11
Surface and Volume Grids	11
Slot Configuration	11
Chimera Overset Grid Scheme	11
Final Form of the Computational Grids	12
Boundary Conditions	12
Slot Boundary Conditions	12
5. Results and Discussion	13
Grid Sensitivity Study	13
No-Blowing Solutions	14
Blowing Solutions	14
Comparison of numerical and experimental results	14
Analysis of computational flow field	15
Effect of axial location of the blowing slot	16
Effect of circumferential location of the blowing slot	17
6. Conclusions	17
References	18

List of Tables and Figures

Table	Page
5.1 List of numerical solutions and jet exit conditions; $M_\infty = 0.2$, $Re_d = 2.81 \times 10^5$	21
 Figure	
1.1 Yaw control power	22
1.2 Forebody tangential slot blowing concept	22
1.3 Effects of tangential slot blowing on a chined forebody	23
1.4 Dimensions of the generic chined forebody wind tunnel model	24
2.1 Generalized transformation from the physical domain to the computational domain	25
2.2 Flow structure in the cross-flow plane	25
2.3 The behavior of $F(y)$ at large incidence	26
4.1 Portion of grid modeling generic chined forebody	27
4.2 Cross-sectional view of blowing slot showing the backward facing step	28
4.3 Cross section of forebody and slot grid overlap	29
4.4 Slot configurations for top and bottom slot blowing	30
4.5 Grid boundaries on the starboard side of the forebody	30
5.1 Surface grid lines of the cases used in the grid sensitivity test	31
5.2 Computed surface flow patterns and helicity density contours, coarse density grid, 50 × 63 × 50 points; $M_\infty = 0.2$, $\alpha = 30$ deg, $Re_d = 2.81 \times 10^5$	32
5.3 Computed surface flow patterns and helicity density contours, medium density grid, 50 × 123 × 50 points; $M_\infty = 0.2$, $\alpha = 30$ deg, $Re_d = 2.81 \times 10^5$	33
5.4 Computed surface flow patterns and helicity density contours, fine density grid, 50 × 243 × 50 points; $M_\infty = 0.2$, $\alpha = 30$ deg, $Re_d = 2.81 \times 10^5$	34
5.5 Computed surface flow patterns and helicity density contours, no-blowing; $M_\infty = 0.2$, $\alpha = 30$ deg, $Re_d = 2.81 \times 10^5$	35
5.6 Computed surface flow patterns and helicity density contours, no-blowing; $M_\infty = 0.2$, $\alpha = 40$ deg, $Re_d = 2.81 \times 10^5$	36
5.7 Comparison of numerical and experimental incremental side force data for <i>Slot I</i> ; $\alpha = 30$ deg, $Re_d = 2.81 \times 10^5$	37
5.8 Comparison of numerical and experimental incremental yawing moment data for <i>Slot I</i> ; $\alpha = 30$ deg, $Re_d = 2.81 \times 10^5$	37
5.9 Comparison of numerical and experimental incremental side force data for <i>Slot I</i> ; $\alpha = 40$ deg, $Re_d = 2.81 \times 10^5$	38
5.10 Comparison of numerical and experimental incremental yawing moment data for <i>Slot I</i> ; $\alpha = 40$ deg, $Re_d = 2.81 \times 10^5$	38
5.11 Effect of angle of attack on yawing moment produced by slot blowing; $Re_d = 2.81 \times 10^5$	39
5.12 Computed helicity density contours at fuselage station $f_S = 4.0$; $M_\infty = 0.2$, $Re_d = 2.81 \times 10^5$	40

5.13	Distribution of computed sectional side-force coefficient along the body; $M_\infty = 0.2$, $\alpha = 40$ deg, $Re_d = 2.81 \times 10^5$	41
5.14	Distribution of computed sectional yawing-moment coefficient along the body; $M_\infty = 0.2$, $\alpha = 40$ deg, $Re_d = 2.81 \times 10^5$	41
5.15	Computed surface flow patterns and helicity density contours; $M_\infty = 0.2$, $\alpha = 40$ deg, $Re_d = 2.81 \times 10^5$, $MFR = 0.23 \times 10^{-3}$	42
5.16	Computed surface flow patterns and helicity density contours; $M_\infty = 0.2$, $\alpha = 40$ deg, $Re_d = 2.81 \times 10^5$, $MFR = 1.49 \times 10^{-3}$	43
5.17	Computed surface flow patterns and helicity density contours; $M_\infty = 0.2$, $\alpha = 40$ deg, $Re_d = 2.81 \times 10^5$, $MFR = 4.17 \times 10^{-3}$	44
5.18	Surface flow patterns; $M_\infty = 0.2$, $\alpha = 40$ deg, $Re_d = 2.81 \times 10^5$	45
5.19	Computed helicity density contours at $f_s = 1.0$; $M_\infty = 0.2$, $\alpha = 40$ deg, $Re_d = 2.81 \times 10^5$	46
5.20	Off-surface instantaneous streamlines; $M_\infty = 0.2$, $\alpha = 40$ deg, $Re_d = 2.81 \times 10^5$	47
5.21	Comparison of numerical and experimental incremental side force data for <i>Slot 1</i> and <i>Slot 2</i> ; $Re_d = 2.81 \times 10^5$	48
5.22	Comparison of numerical and experimental incremental yawing moment data for <i>Slot 1</i> and <i>Slot 2</i> ; $Re_d = 2.81 \times 10^5$	48
5.23	Computed surface flow patterns and helicity density contours, <i>Slot 2</i> ; $M_\infty = 0.2$, $\alpha = 40$ deg, $Re_d = 2.81 \times 10^5$, $MFR = 1.49 \times 10^{-3}$	49
5.24	Computed helicity density contours at $f_s = 4.0$; $M_\infty = 0.2$, $\alpha = 40$ deg, $Re_d = 2.81 \times 10^5$, $MFR = 1.49 \times 10^{-3}$	50
5.25	Instantaneous streamlines; $M_\infty = 0.2$, $\alpha = 40$ deg, $Re_d = 2.81 \times 10^5$, $MFR = 1.49 \times 10^{-3}$	51
5.26	Comparison of numerical incremental side force data for blowing from the top surface and bottom surface, <i>Slot 1</i> ; $M_\infty = 0.2$, $\alpha = 40$ deg, $Re_d = 2.81 \times 10^5$	52
5.27	Comparison of numerical incremental yawing moment data for blowing from the top surface and bottom surface, <i>Slot 1</i> ; $M_\infty = 0.2$, $\alpha = 40$ deg, $Re_d = 2.81 \times 10^5$	52
5.28	Computed surface flow patterns and helicity density contours, bottom blowing; $M_\infty = 0.2$, $\alpha = 40$ deg, $Re_d = 2.81 \times 10^5$, $MFR = 1.49 \times 10^{-3}$	53

Nomenclature

a	speed of sound
c_n	sectional yawing moment coefficient
c_p	specific heat at constant pressure
c_v	specific heat at constant volume
c_Y	sectional side force coefficient
C_n	yawing moment coefficient, $C_n \equiv \frac{n}{q_\infty S_{ref} L_{ref}}$
C_Y	side force coefficient, $C_Y \equiv \frac{Y}{q_\infty S_{ref}}$
C_μ	momentum coefficient of blowing, $C_\mu \equiv \frac{\dot{m}_{jet} V_{jet}}{q_\infty S_{ref}}$
e	total energy per unit volume
e_I	internal energy per unit mass
f_s	fuselage station, measured from the nose of body
J	Jacobian
k	coefficient of thermal conductivity
L_{ref}	body reference length, $L_{ref} \equiv 8.086$ in.
n	yawing moment
\dot{m}	mass flow rate
\dot{m}_{jet}	jet mass flow rate, $\dot{m}_{jet} \equiv \rho_{jet} V_{jet} S_{jet}$
\dot{m}_{ref}	reference mass flow rate, $\dot{m}_{ref} \equiv \rho_\infty V_\infty S_{ref}$
M	Mach number
MFR	mass flow ratio, $MFR \equiv \frac{\dot{m}_{jet}}{\dot{m}_{ref}}$
p	pressure
Pr	Prandtl number, $Pr \equiv \frac{\mu c_p}{k}$
Pr_t	turbulent Prandtl number
q_∞	free-stream dynamic pressure, $q_\infty \equiv \frac{1}{2} \rho_\infty V_\infty^2$

R	gas constant
Re_d	Reynolds number based on free-stream conditions and body reference length, $Re_d \equiv \frac{\rho_\infty V_\infty L_{ref}}{\mu_\infty}$
S_{jet}	jet exit area, $S_{jet} \equiv 0.005$ in. ²
S_{ref}	body reference area, $S_{ref} \equiv 51.276$ in. ²
t	time
T	temperature
u, v, w	velocity components in the x, y, z directions
U, V, W	contravariant velocity components (eq. (2.23))
x, y, z	Cartesian coordinates
Y	side force
α	angle of attack
γ	ratio of specific heats, $\gamma \equiv \frac{c_p}{c_v}$
δ	central-difference operator
$\bar{\delta}$	mid-point operator
λ	coefficient of bulk viscosity
μ	coefficient of viscosity
$\mu\tau$	turbulent eddy viscosity coefficient
ξ, η, ζ	transformed coordinates
ρ	density
τ	computational time

Subscripts

a	ambient conditions
jet	jet exit conditions
ref	reference conditions
∞	free-stream values

Superscript

n	time level
-----	------------

Numerical Analysis of Tangential Slot Blowing on a Generic Chined Forebody

ROXANA M. AGOSTA

Ames Research Center

Summary

A numerical study is performed to investigate the effects of tangential slot blowing on a generic chined forebody. The Reynolds-averaged, thin-layer, Navier–Stokes equations are solved to obtain the high-angle-of-attack viscous flow field about a generic chined forebody. Tangential slot blowing is investigated as a means of forebody flow control to generate side force and yawing moment on the forebody. The effects of jet mass flow ratios, angle of attack, and blowing slot location in the axial and circumferential directions are studied. The computed results are compared with available wind tunnel experimental data. The solutions with and without blowing are also analyzed using helicity density contours, surface flow patterns, and off-surface instantaneous streamlines. The results of this analysis provide details of the flow field about the generic chined forebody, as well as show that tangential slot blowing can be used as a means of forebody flow control to generate side force and yawing moment.

1. Introduction

Future aircraft designs will make use of the fixed separation points of a diamond-shaped cross section or a chined forebody, as utilized on the YF-22 and the F-23 configurations. Wind tunnel tests have been conducted to compare a conventional forebody with a chined forebody (ref. 1). These tests show that the chined forebody produces more lift than the conventional forebody, even at post-stall angles of attack. This is due to the additional planform area and the suction produced by the strong forebody vortices. These forebody vortices also give the chined forebody improved lateral-directional stability, which can be attributed to the upward shift of the leeward vortex. Chined geometries have been shown to reduce the radar cross section of a body (ref. 2) and thus minimize radar detection.

As the flight envelope of present and future aircraft increases to include high-angle-of-attack flight, the need to understand the complex flow field of an aircraft flying in this regime increases. The flow field about a body at high angle of attack is dominated by large regions of three-dimensional separated flow. The boundary layer

separates from the body and rolls up on the leeward side of the body to form strong vortices (refs. 3–6). Possible vortex asymmetry in the flow field can produce side force and yawing and rolling moments, which may lead to aircraft instability. Furthermore, the vertical tails lie in the wake of the forebody and wings, which reduces the effectiveness of these control surfaces. As the aircraft angle of attack increases, the yaw control power required to coordinate a rolling maneuver increases to levels beyond what conventional rudders can provide (fig. 1.1). Forebody flow control has the potential of providing additional directional control power at large angles of attack.

Forebody flow control can be obtained using mechanical or pneumatic methods. Experimental and numerical investigations show that both methods produce similar results (refs. 1 and 7). One method currently being investigated is forebody tangential slot blowing (refs. 1, 8, and 9). In this method, air is blown tangential to the surface from a thin slot which is located on the forebody of the aircraft (fig. 1.2). In a “conventional,” smooth forebody, tangential slot blowing will move the primary cross-flow separation location toward the leeward symmetry plane on the blowing side, and there may or may not be a secondary separation on the blowing side. For a chined forebody, the primary separation will occur at the chine for the no-blowing case as shown in figure 1.3. Unlike a conventional, smooth forebody, blowing from a slot located on the top surface of the chined forebody does not move the primary separation line from its location at the chine line, but it does disturb the no-blowing flow field (fig. 1.3(a)), and draws the blowing-side vortex toward the surface while the nonblowing-side vortex moves away from the surface (fig. 1.3(b)). Blowing outboard from a slot located on the bottom surface (fig. 1.3(c)) has a similar, but mirror-image effect. Here the jet forces the blowing-side vortex away from the body surface, while the nonblowing-side vortex moves closer to the body. In contrast to a conventional forebody, the primary cross-flow separation remains located at the chine, and a secondary separation does exist. These changes in the flow field generate side forces and yawing moments which have the potential of being employed to control the aircraft at high angles of attack.

A small-scale wind tunnel experiment was performed (ref. 10) in the 3- by 4-Foot Low Speed Wind Tunnel at California Polytechnic State University (Cal Poly) to investigate the effectiveness of tangential slot blowing on a generic chined forebody. The dimensions of the wind tunnel model are shown in figure 1.4. The effects of varying slot lengths, jet mass flow ratios, and varying angles of attack were investigated. Experimental results obtained included measurement of total forces and moments, as well as limited flow visualization.

In this study, a complementary computational fluid dynamics (CFD) investigation of tangential slot blowing is performed on a generic chined forebody similar to the model used in the Cal Poly wind tunnel test. The primary objective is to numerically investigate tangential slot blowing on a generic chined forebody as a means of generating side force and yawing moment. The effects of jet mass flow ratios, angle of attack, and blowing slot location in the axial and circumferential directions are studied. The numerical results are compared with the data obtained in the Cal Poly wind tunnel experiment, and extend the results to slot configurations not tested in the wind tunnel.

This work is presented in the following sections. The governing equations and numerical methods are discussed in sections 2 and 3, respectively. Grid generation and boundary conditions are described in section 4. Section 5 analyzes the flow field about the generic chined forebody and the effects of jet mass flow ratios, angle of attack, and slot locations. Finally, section 6 summarizes the results and discussions.

I wish to express my appreciation to Russell M. Cummings, for his valuable advice and guidance throughout this study. I am also grateful to Jon A. Hoffmann, Ronald S. Mullisen, Lewis B. Schiff, and Ken Gee for their remarks and discussion. This study was funded in part by NASA Grant NCA2-626.

2. Governing Equations

The universal laws of the conservation of mass, momentum, and energy are the basis of the fundamental equations of fluid dynamics. These conservation laws are used to compose the three-dimensional Navier–Stokes equations which are the governing equations for a Newtonian fluid. A Newtonian fluid is a fluid where the stress is linearly dependent on the rate of strain. The Navier–Stokes equations are a set of five coupled, nonlinear partial differential equations which are the foundation of the science of viscous flow theory (ref. 11).

Upon assuming that body forces and the addition of external heat are negligible, the Navier–Stokes equations can be written in nondimensionalized conservation law form as

$$\frac{\partial \mathbf{Q}}{\partial t} + \frac{\partial \mathbf{E}}{\partial x} + \frac{\partial \mathbf{F}}{\partial y} + \frac{\partial \mathbf{G}}{\partial z} = \frac{1}{Re} \left(\frac{\partial \mathbf{E}_v}{\partial x} + \frac{\partial \mathbf{F}_v}{\partial y} + \frac{\partial \mathbf{G}_v}{\partial z} \right) \quad (2.1)$$

where \mathbf{Q} , \mathbf{E} , \mathbf{F} , and \mathbf{G} are the flux vectors given by

$$\begin{aligned} \mathbf{Q} &= \begin{bmatrix} \rho \\ \rho u \\ \rho v \\ \rho w \\ e \end{bmatrix} & \mathbf{E} &= \begin{bmatrix} \rho u \\ \rho u^2 + p \\ \rho uv \\ \rho uw \\ (e + p)u \end{bmatrix} \\ \mathbf{F} &= \begin{bmatrix} \rho v \\ \rho uv \\ \rho v^2 + p \\ \rho vw \\ (e + p)v \end{bmatrix} & \mathbf{G} &= \begin{bmatrix} \rho w \\ \rho uw \\ \rho vw \\ \rho w^2 + p \\ (e + p)w \end{bmatrix} \end{aligned} \quad (2.2)$$

where ρ is density, u , v , and w are the x , y , and z velocity components, respectively, p is pressure, and e is the total energy per unit volume. In equation (2.3), the Reynolds number, Re , is defined as

$$Re = \frac{\rho_\infty a_\infty L}{\mu_\infty} \quad (2.3)$$

where the subscript ∞ denotes free-stream values, a is the speed of sound, L is a reference length, and μ is the coefficient of viscosity. The Reynolds number indicates the relative importance of inertial and viscous effects in the fluid motion. The viscous flux vectors, \mathbf{E}_v , \mathbf{F}_v , and \mathbf{G}_v , are defined as

$$\begin{aligned} \mathbf{E}_v &= \begin{bmatrix} 0 \\ \tau_{xx} \\ \tau_{yx} \\ \tau_{zx} \\ \beta_x \end{bmatrix} & \mathbf{F}_v &= \begin{bmatrix} 0 \\ \tau_{xy} \\ \tau_{yy} \\ \tau_{zy} \\ \beta_y \end{bmatrix} & \mathbf{G}_v &= \begin{bmatrix} 0 \\ \tau_{xz} \\ \tau_{yz} \\ \tau_{zz} \\ \beta_z \end{bmatrix} \end{aligned} \quad (2.4)$$

where

$$\begin{aligned}
\tau_{xx} &= \lambda(u_x + v_y + w_z) + 2\mu u_x \\
\tau_{yy} &= \lambda(u_x + v_y + w_z) + 2\mu v_y \\
\tau_{zz} &= \lambda(u_x + v_y + w_z) + 2\mu w_z \\
\tau_{xy} &= \tau_{yx} = \mu(u_y + v_x) \\
\tau_{xz} &= \tau_{zx} = \mu(u_z + w_x) \\
\tau_{yz} &= \tau_{zy} = \mu(v_z + w_y) \\
\beta_x &= \gamma k Pr^{-1} \partial_x e_I + u\tau_{xx} + v\tau_{xy} + w\tau_{xz} \\
\beta_y &= \gamma k Pr^{-1} \partial_y e_I + u\tau_{yx} + v\tau_{yy} + w\tau_{yz} \\
\beta_z &= \gamma k Pr^{-1} \partial_z e_I + u\tau_{zx} + v\tau_{zy} + w\tau_{zz}
\end{aligned} \tag{2.5}$$

Here, the Prandtl number, Pr , is

$$Pr = \frac{\mu c_p}{k_\infty} \tag{2.6}$$

where c_p is the specific heat at constant pressure, and k is the coefficient of thermal conductivity. The Prandtl number is indicative of the relative ability of the fluid to diffuse momentum and internal energy by molecular mechanisms.

The internal energy, e_I , and the pressure, p , are given in terms of the other flow variables as

$$\begin{aligned}
e_I &= \frac{e}{\rho} - 0.5(u^2 + v^2 + w^2) \\
p &= (\gamma - 1) \left[e - 0.5\rho(u^2 + v^2 + w^2) \right]
\end{aligned} \tag{2.7}$$

The following procedure was followed in order to nondimensionalize the variables appearing in equations (2.1–2.7): the spatial coordinates, (x, y, z) , are divided by a reference length, L_{ref} ; the velocity is divided by the free-stream speed of sound; density and viscosity are divided by their free-stream values; time is divided by L_{ref}/a_∞ ; and the pressure is normalized by $\rho_\infty a_\infty^2$. Stokes hypothesis is applied, which states that for a gas the coefficient of bulk viscosity, λ , can be related to the coefficient of dynamic viscosity, μ , by the following relationship

$$\lambda = -\frac{2}{3}\mu \tag{2.8}$$

For turbulent flows, equation (2.1) can be considered to be the Reynolds-averaged Navier–Stokes equations, where the high frequency fluctuations of the turbulent flow field are time averaged. For turbulent flows, a turbulence model must be used to specify the coefficients of viscosity and heat conductivity which appear in the viscous terms in equation (2.5). This will be further discussed in a following subsection.

Coordinate Transformation

In order to apply the numerical algorithm and boundary conditions easily, the governing equations which are developed in the physical domain or Cartesian coordinates, (x, y, z) , must be transformed to the computational domain or generalized coordinates, (ξ, η, ζ) , as seen in figure 2.1 (ref. 11). In this study, ξ , η , and ζ are the coordinates in the axial, circumferential, and radial directions, respectively. The general transformation is of the form

$$\begin{aligned}
\xi &= \xi(x, y, z, t) \\
\eta &= \eta(x, y, z, t) \\
\zeta &= \zeta(x, y, z, t) \\
\tau &= t
\end{aligned} \tag{2.9}$$

and the inverse of the transformation is

$$\begin{aligned}
x &= x(\xi, \eta, \zeta, \tau) \\
y &= y(\xi, \eta, \zeta, \tau) \\
z &= z(\xi, \eta, \zeta, \tau) \\
t &= \tau
\end{aligned} \tag{2.10}$$

The transformation brings the body surface onto one computational plane ($\zeta = 1$). The computational domain is chosen to have equal spacing ($\Delta\xi = \Delta\eta = \Delta\zeta = 1$) to simplify the differencing. By using the chain rule of partial differentiation, the partial derivatives in the physical domain become

$$\begin{aligned}
\frac{\partial}{\partial x} &= \xi_x \frac{\partial}{\partial \xi} + \eta_x \frac{\partial}{\partial \eta} + \zeta_x \frac{\partial}{\partial \zeta} \\
\frac{\partial}{\partial y} &= \xi_y \frac{\partial}{\partial \xi} + \eta_y \frac{\partial}{\partial \eta} + \zeta_y \frac{\partial}{\partial \zeta} \\
\frac{\partial}{\partial z} &= \xi_z \frac{\partial}{\partial \xi} + \eta_z \frac{\partial}{\partial \eta} + \zeta_z \frac{\partial}{\partial \zeta} \\
\frac{\partial}{\partial t} &= \xi_t \frac{\partial}{\partial \xi} + \eta_t \frac{\partial}{\partial \eta} + \zeta_t \frac{\partial}{\partial \zeta} + \frac{\partial}{\partial \tau}
\end{aligned} \tag{2.11}$$

where $\tau_t = 1$ and the metrics τ_x, τ_y , and τ_z are equal to zero. The metrics ($\xi_x, \eta_x, \zeta_x, \xi_y, \eta_y, \zeta_y, \xi_z, \eta_z, \zeta_z, \xi_t, \eta_t, \zeta_t$) that appear in equations (2.10) are obtained in the following manner. The differential expressions are

$$\begin{aligned}
d\xi &= \xi_x dx + \xi_y dy + \xi_z dz + \xi_t dt \\
d\eta &= \eta_x dx + \eta_y dy + \eta_z dz + \eta_t dt \\
d\zeta &= \zeta_x dx + \zeta_y dy + \zeta_z dz + \zeta_t dt \\
d\tau &= dt
\end{aligned} \tag{2.12}$$

which can be written in matrix form as

$$\begin{bmatrix} d\xi \\ d\eta \\ d\zeta \\ d\tau \end{bmatrix} = \begin{bmatrix} \xi_x & \xi_y & \xi_z & \xi_t \\ \eta_x & \eta_y & \eta_z & \eta_t \\ \zeta_x & \zeta_y & \zeta_z & \zeta_t \\ 0 & 0 & 0 & 1 \end{bmatrix} \begin{bmatrix} dx \\ dy \\ dz \\ dt \end{bmatrix} \tag{2.13}$$

Similarly,

$$\begin{bmatrix} dx \\ dy \\ dz \\ dt \end{bmatrix} = \begin{bmatrix} x\xi & x\eta & x\zeta & x\tau \\ y\xi & y\eta & y\zeta & y\tau \\ z\xi & z\eta & z\zeta & z\tau \\ 0 & 0 & 0 & 1 \end{bmatrix} \begin{bmatrix} d\xi \\ d\eta \\ d\zeta \\ d\tau \end{bmatrix} \tag{2.14}$$

Therefore

$$\begin{bmatrix} \xi_x & \xi_y & \xi_z & \xi_t \\ \eta_x & \eta_y & \eta_z & \eta_t \\ \zeta_x & \zeta_y & \zeta_z & \zeta_t \\ 0 & 0 & 0 & 1 \end{bmatrix} = \begin{bmatrix} x\xi & x\eta & x\zeta & x\tau \\ y\xi & y\eta & y\zeta & y\tau \\ z\xi & z\eta & z\zeta & z\tau \\ 0 & 0 & 0 & 1 \end{bmatrix}^{-1} \tag{2.15}$$

Thus, the transformation metrics are

$$\begin{aligned}
\xi_x &= J(y\eta z\zeta - y\zeta z\eta) \\
\xi_y &= -J(x\eta z\zeta - x\zeta z\eta) \\
\xi_z &= J(x\eta y\zeta - x\zeta y\eta) \\
\eta_x &= -J(y\xi z\zeta - y\zeta z\xi) \\
\eta_y &= J(x\xi z\zeta - x\zeta z\xi) \\
\eta_z &= -J(x\xi y\zeta - x\zeta y\xi) \\
\zeta_x &= J(y\xi z\eta - y\eta z\xi) \\
\zeta_y &= -J(x\xi z\eta - x\eta z\xi) \\
\zeta_z &= J(x\xi y\eta - x\eta y\xi) \\
\xi_t &= -x_\tau \xi_x - y_\tau \xi_y - z_\tau \xi_z \\
\eta_t &= -x_\tau \eta_x - y_\tau \eta_y - z_\tau \eta_z \\
\zeta_t &= -x_\tau \zeta_x - y_\tau \zeta_y - z_\tau \zeta_z
\end{aligned} \tag{2.16}$$

where J is the Jacobian of the transformation, defined as

$$J = \frac{\partial(\xi, \eta, \zeta, \tau)}{\partial(x, y, z, t)} = \begin{vmatrix} \xi_x & \xi_y & \xi_z & \xi_t \\ \eta_x & \eta_y & \eta_z & \eta_t \\ \zeta_x & \zeta_y & \zeta_z & \zeta_t \\ 0 & 0 & 0 & 1 \end{vmatrix} \tag{2.17}$$

This may be simplified to

$$J = \frac{\partial(\xi, \eta, \zeta)}{\partial(x, y, z)} = \begin{vmatrix} \xi_x & \xi_y & \xi_z \\ \eta_x & \eta_y & \eta_z \\ \zeta_x & \zeta_y & \zeta_z \end{vmatrix} \tag{2.18}$$

which can be evaluated in the following manner

$$\begin{aligned}
J &= \frac{1}{J^{-1}} = \frac{1}{\frac{\partial(x, y, z)}{\partial(\xi, \eta, \zeta)}} = \begin{vmatrix} x\xi & x\eta & x\zeta \\ y\xi & y\eta & y\zeta \\ z\xi & z\eta & z\zeta \end{vmatrix}^{-1} \\
&= \begin{bmatrix} x\xi(y\eta z\zeta - y\zeta z\eta) - x\eta(y\xi z\zeta - y\zeta z\xi) \\ +x\zeta(y\xi z\eta - y\eta z\xi) \end{bmatrix}^{-1}
\end{aligned} \tag{2.19}$$

The metrics can be determined by using a finite-difference scheme in the computational domain.

Applying this generalized transformation to the Navier–Stokes equation (2.1), the following transformed equations are obtained

$$\frac{\partial \hat{\mathbf{Q}}}{\partial \tau} + \frac{\partial \hat{\mathbf{E}}}{\partial \xi} + \frac{\partial \hat{\mathbf{F}}}{\partial \eta} + \frac{\partial \hat{\mathbf{G}}}{\partial \zeta} = \frac{1}{Re} \left(\frac{\partial \hat{\mathbf{E}}_V}{\partial \xi} + \frac{\partial \hat{\mathbf{F}}_V}{\partial \eta} + \frac{\partial \hat{\mathbf{G}}_V}{\partial \zeta} \right) \quad (2.20)$$

where the inviscid flux terms are

$$\begin{aligned} \hat{\mathbf{Q}} &= J^{-1} \begin{bmatrix} \rho \\ \rho u \\ \rho v \\ \rho w \\ e \end{bmatrix} & \hat{\mathbf{E}} &= J^{-1} \begin{bmatrix} \rho U \\ \rho u U + \xi_x p \\ \rho v U + \xi_y p \\ \rho w U + \xi_z p \\ (e + p)U - \xi_t p \end{bmatrix} \\ \hat{\mathbf{F}} &= J^{-1} \begin{bmatrix} \rho V \\ \rho u V + \eta_x p \\ \rho v V + \eta_y p \\ \rho w V + \eta_z p \\ (e + p)V - \eta_t p \end{bmatrix} & \hat{\mathbf{G}} &= J^{-1} \begin{bmatrix} \rho W \\ \rho u W + \zeta_x p \\ \rho v W + \zeta_y p \\ \rho w W + \zeta_z p \\ (e + p)W - \zeta_t p \end{bmatrix} \end{aligned} \quad (2.21)$$

while the viscous flux terms are given by

$$\begin{aligned} \hat{\mathbf{E}}_V &= J^{-1} \begin{bmatrix} 0 \\ \xi_x \tau_{xx} + \xi_y \tau_{xy} + \xi_z \tau_{xz} \\ \xi_x \tau_{yx} + \xi_y \tau_{yy} + \xi_z \tau_{yz} \\ \xi_x \tau_{zx} + \xi_y \tau_{zy} + \xi_z \tau_{zz} \\ \xi_x \beta_x + \xi_y \beta_y + \xi_z \beta_z \end{bmatrix} \\ \hat{\mathbf{F}}_V &= J^{-1} \begin{bmatrix} 0 \\ \eta_x \tau_{xx} + \eta_y \tau_{xy} + \eta_z \tau_{xz} \\ \eta_x \tau_{yx} + \eta_y \tau_{yy} + \eta_z \tau_{yz} \\ \eta_x \tau_{zx} + \eta_y \tau_{zy} + \eta_z \tau_{zz} \\ \eta_x \beta_x + \eta_y \beta_y + \eta_z \beta_z \end{bmatrix} \\ \hat{\mathbf{G}}_V &= J^{-1} \begin{bmatrix} 0 \\ \zeta_x \tau_{xx} + \zeta_y \tau_{xy} + \zeta_z \tau_{xz} \\ \zeta_x \tau_{yx} + \zeta_y \tau_{yy} + \zeta_z \tau_{yz} \\ \zeta_x \tau_{zx} + \zeta_y \tau_{zy} + \zeta_z \tau_{zz} \\ \zeta_x \beta_x + \zeta_y \beta_y + \zeta_z \beta_z \end{bmatrix} \end{aligned} \quad (2.22)$$

In equations (2.21) U , V , and W are the contravariant velocity components defined as

$$\begin{aligned} U &= \xi_t + \xi_x u + \xi_y v + \xi_z w \\ V &= \eta_t + \eta_x u + \eta_y v + \eta_z w \\ W &= \zeta_t + \zeta_x u + \zeta_y v + \zeta_z w \end{aligned} \quad (2.23)$$

Thin-Layer Approximation

The thin-layer approximation to the Navier–Stokes equations is generally used with a body-oriented coordinate system, (ξ, η, ζ) , where one of the coordinates (usually ζ) is approximately normal to the surface of the body. The thin-layer approximation is formally derived from the complete Navier–Stokes equations by using the same principles employed in the derivation of the unsteady boundary-layer equations, where terms on the order of $1/(Re_L)^{1/2}$ and smaller are neglected. As a result, in the thin-layer approximation to the Navier–Stokes equations, the viscous terms containing derivatives in the directions parallel to the body surface are neglected.

The concept of thin-layer approximation also stems from examining typical high Reynolds number computations involving the complete Navier–Stokes equations (ref. 12). These computations involve highly stretched grids where the spacing in the streamwise direction is much larger than in the normal direction. As a consequence, the gradients parallel to the body surface are generally not resolved adequately even if the complete viscous terms are included in the computations (ref. 12). Thus, for high Reynolds number Navier–Stokes computations, the terms that are not being adequately resolved should be dropped, providing they are relatively small.

The thin-layer approximation to the transformed Navier–Stokes can be applied to a body in the computational domain, (ξ, η, ζ) , where ζ is the coordinate normal to the body surface. The approximation states that all viscous terms containing partial derivatives with respect to ξ and η are neglected (ref. 13). The resulting thin-layer governing equations are

$$\frac{\partial \hat{\mathbf{Q}}}{\partial \tau} + \frac{\partial \hat{\mathbf{E}}}{\partial \xi} + \frac{\partial \hat{\mathbf{F}}}{\partial \eta} + \frac{\partial \hat{\mathbf{G}}}{\partial \zeta} = \frac{1}{Re} \left(\frac{\partial \hat{\mathbf{S}}}{\partial \zeta} \right) \quad (2.24)$$

where $\hat{\mathbf{Q}}$, $\hat{\mathbf{E}}$, $\hat{\mathbf{F}}$, and $\hat{\mathbf{G}}$ are identical to those defined in equations (2.21), and the retained viscous terms are

$$\hat{\mathbf{S}} = \mathbf{J}^{-1} \begin{bmatrix} 0 \\ \mu(\zeta_x^2 + \zeta_y^2 + \zeta_z^2)u\zeta + \frac{\mu}{3}(\zeta_x u\zeta + \zeta_y v\zeta + \zeta_z w\zeta)\zeta_x \\ \mu(\zeta_x^2 + \zeta_y^2 + \zeta_z^2)v\zeta + \frac{\mu}{3}(\zeta_x u\zeta + \zeta_y v\zeta + \zeta_z w\zeta)\zeta_y \\ \mu(\zeta_x^2 + \zeta_y^2 + \zeta_z^2)w\zeta + \frac{\mu}{3}(\zeta_x u\zeta + \zeta_y v\zeta + \zeta_z w\zeta)\zeta_z \\ \left(\zeta_x^2 + \zeta_y^2 + \zeta_z^2 \right) \left[\frac{\mu}{2}(u^2 + v^2 + w^2)\zeta \right. \\ \left. + \frac{k}{Pr(\gamma - 1)}(a^2)\zeta \right] \\ \left. + \frac{\mu}{3}(\zeta_x u + \zeta_y v + \zeta_z w)(\zeta_x u\zeta + \zeta_y v\zeta + \zeta_z w\zeta) \right] \quad (2.25)$$

Even with the reductions in computer time due to the use of the reduced viscous terms, solution of the thin-layer Navier–Stokes equations about complex geometries still require a large amount of computer time, particularly in comparison with the time needed for solutions of the inviscid Euler equations. However, at a minimum, the thin-layer Navier–Stokes equations are needed to resolve the complex viscous flow physics for the cases under study. Studies have shown that using the full Navier–Stokes equations versus the thin-layer Navier–Stokes equations shows no significant improvement in the computational solutions for high-angle-of-attack flows. The thin-layer assumption remains valid for high-alpha flows about slender bodies since the flow field can be considered as a series of attached viscous boundary layers on the body surface, underneath the separated vortical external flow. Moreover, the grid spacing in the streamwise and circumferential directions is coarse when compared to the spacing in the normal direction within the viscous layers.

Turbulence Modeling

In order to predict turbulent flows by solving the thin-layer Navier–Stokes equations, closure assumptions must be made about the apparent turbulent stress and heat-flux quantities. The Boussinesq approximation, that the apparent turbulent shearing stresses might be related to the rate of mean strain through an apparent scalar turbulent or eddy viscosity, is used. In this study, the Baldwin–Lomax turbulence model (ref. 12) will be used, together with the Degani–Schiff modifications (ref. 13) for high-alpha flows.

Baldwin–Lomax turbulence model– The Baldwin–Lomax turbulence model (ref. 12) is a zero-equation, two-layer algebraic model which is widely used because of its simplicity, low computational time, and

accuracy. A study (ref. 14) was conducted to compare results obtained using the Baldwin–Lomax turbulence model with results from more complex models for turbulent flow about a prolate spheroid at high angles of attack. It was found that the more complex models gave no improvement in resolving the flow physics; thus, the Baldwin–Lomax model was used in this study.

The Baldwin–Lomax turbulence model is developed from an algebraic model developed by Cebeci (ref. 15), with modifications that avoid determining the edge of the boundary layer. This makes the Baldwin–Lomax turbulence model easier to use with finite-differencing schemes.

The effects of turbulence are simulated in terms of an eddy viscosity coefficient, μ_t , and a coefficient of thermal conductivity, k , in the Navier–Stokes equations. For turbulent-flow computations, the coefficients of viscosity and thermal conductivity are assumed to consist of the sum of the laminar-flow and the turbulent-flow coefficients

$$\mu = \mu_l + \mu_t \quad (2.26)$$

$$\frac{k}{c_p} = \frac{\mu_l}{Pr} + \frac{\mu_t}{Pr_t} \quad (2.27)$$

In equation (2.25), k and μ are related through the assumption of a constant Prandtl number. The laminar molecular viscosity, μ_l , is obtained from Sutherland's Law (ref. 12)

$$\mu_l = C_1 \frac{T^{3/2}}{T + C_2} \quad (2.28)$$

where T is the temperature (°R), and C_1 and C_2 are constants for a given gas. For air at moderate temperatures, $C_1 = 2.27 \times 10^{-8}$ lbf sec/ft² and $C_2 = 198.6$ °R.

The turbulent flow about a body is divided into an inner (near wall) region and an outer region. A different formula is used in each region to determine the turbulent molecular viscosity, μ_t , which is defined as

$$\mu_t = \begin{cases} \mu_{t,inner} & y \leq y_{crossover} \\ \mu_{t,outer} & y_{crossover} < y \end{cases} \quad (2.29)$$

where y is the normal distance from the wall and $y_{crossover}$ is the smallest value of y at which values from the inner and the outer formulas are equal.

The inner region turbulent viscosity coefficient is found by using the Prandtl–Van Driest formula

$$(\mu_t)_{inner} = \rho \ell^2 |\omega| \quad (2.30)$$

where ρ is density and

$$\ell = ky \left[1 - \exp(-y^+ / A^+) \right] \quad (2.31)$$

The magnitude of the vorticity, $|\omega|$, is expressed in Cartesian coordinates as

$$|\omega| = \sqrt{\left(\frac{\partial u}{\partial y} - \frac{\partial v}{\partial x} \right)^2 + \left(\frac{\partial v}{\partial z} - \frac{\partial w}{\partial y} \right)^2 + \left(\frac{\partial w}{\partial x} - \frac{\partial u}{\partial z} \right)^2} \quad (2.32)$$

In equation (2.31), k and A^+ are constants, and y^+ is defined as

$$y^+ = \frac{\rho_w u_{\tau} y}{\mu_w} = \frac{\sqrt{\rho_w \tau_w} y}{\mu_w} \quad (2.33)$$

The subscript w in equation (2.33) denotes values evaluated at the wall.

The outer region turbulent viscosity coefficient for attached boundary layers is determined by

$$(\mu_t)_{outer} = K C_{cp} F_{wake} F_{Kleb}(y) \quad (2.34)$$

where K is the Clauser constant, C_{cp} is an additional constant, and F_{wake} is determined by the relationship

$$F_{wake} = \min \{ (y_{max} F_{max}), (C_{wk} y_{max} u_{dif}^2 / F_{max}) \} \quad (2.35)$$

where

$$u_{dif} = \left(\sqrt{u^2 + v^2 + w^2} \right)_{max} - \left(\sqrt{u^2 + v^2 + w^2} \right)_{min} \quad (2.36)$$

The second term in u_{dif} is set equal to zero except in wakes. The function $F_{Kleb}(y)$ is the Klebanoff intermittency factor given by

$$F_{Kleb}(y) = \left[1 + 5.5 \left(\frac{C_{Kleb} y}{y_{max}} \right)^6 \right]^{-1} \quad (2.37)$$

In equation (2.35), F_{max} is the maximum value of the following function in the local profile

$$F(y) = y |\omega| \left[1 - \exp(-y^+ / A^+) \right] \quad (2.38)$$

and y_{max} is the value of y at which this maximum occurs from the body surface.

The constants in equations (2.34–2.38) were determined (ref. 12) by requiring agreement with the Cebeci (ref. 16) formulation for constant pressure boundary layers at transonic speeds. The values are reported (ref. 12) as

$$\begin{aligned} A^+ &= 26 & k &= 0.4 \\ C_{cp} &= 1.6 & K &= 0.0168 \\ C_{Kleb} &= 0.3 & Pr &= 0.72 \\ C_{wk} &= 0.25 & Pr_t &= 0.9 \end{aligned} \quad (2.39)$$

Degani–Schiff modifications– The flow fields of a body at high angles of attack are complex and generally contain regions of three-dimensional cross-flow separation as shown in figure 2.2 (ref. 13). Cross-flow separation appears when fluid flowing circumferentially from the windward to the leeward side of the body separates from the sides of the body along a separation line that is nominally parallel to the longitudinal axis of the body. Then the fluid rolls up to form a well defined vortex structure on the leeward side of the body (ref. 13). The amount of cross-flow separation increases as the angle of attack increases. Thus, accurate resolution of the cross-flow separation line on the leeward side of the body is important when computing high-angle-of-attack flows.

When applying the original Baldwin–Lomax turbulence model in regions of cross-flow separation, it is difficult to correctly determine the values for y_{max} in the separated regions. In the outer region, the original method led to unrealistic values of μ_t . Both y_{max} and $(\mu_t)_{outer}$ are overly predicted, causing the flow structures on the body surface to disappear. In the resulting numerical solutions, this overprediction leads to the inability to determine secondary or tertiary separation lines and causes the primary vortices to be much smaller than those observed experimentally (ref. 13).

This can be illustrated further by examining $F(y)$ in equation (2.38) at two stations: one on the windward side at $\phi = \phi_1$ and the other on the leeward side at $\phi = \phi_2$. The boundary layer remains attached on the windward side as shown in figure 2.2, and the corresponding profile of $F(y)$ has a single peak (fig. 2.3(a)). However, for the profile on the leeward side, two peaks exist, where the larger peak is not the desired one within the boundary layer. The original implementation of the Baldwin–Lomax turbulence model would have selected the largest value of $F(y)$ which would result in an overprediction of y_{max} and F_{max} and thus determine a value of μ_t that is too large. As a result, the computed turbulent viscosity coefficients behind the primary separation point would be too high and would wash out the details of the leeward flow field.

In order to correct this problem, Degani and Schiff (ref. 13) developed a scheme that stops the search for F_{max} once the first maximum is reached. The function $F(y)$ is calculated along a ray normal to the surface at each surface grid point. The scheme finds the first peak in

$F(y)$ and then stops. A peak or local maximum is defined when $F(y)$ drops to 90% of the local maximum value.

In the region close to a separation line, a further criterion is needed. Near the separation line the separated vortex sheet (the second maximum of $F(y)$) lies close to the first maximum, and therefore, the cutoff criterion as described above would select the second maximum of $F(y)$ to be the correct maximum instead of the desired first one. Hence, a second criterion must be used to solve this dilemma. A search cutoff distance is specified based upon the y_{max} from the previous ray such that

$$y_{cutoff}(\phi) = c y_{max}(\phi = 0) \quad (2.40)$$

where c is a constant nominally set between 3 and 5. In the present study, $c = 3.0$. The rays are searched sequentially from the windward to the leeward side in the circumferential direction. If no maximum is found in $F(y)$ from $y \leq y_{cutoff}$ then the values of F_{max} , y_{max} from the previous ray are used. This assumption can be justified since the conditions of the attached and separated boundary layers must be related and should vary in a smooth, continuous manner circumferentially around the body.

3. Numerical Methods

In this study the algorithm employed to solve the thin-layer Navier–Stokes equations is the F3D code reported by Steger, Ying, and Schiff (ref. 16). This algorithm is a two-factor, implicit, finite-difference algorithm utilizing an approximate-factored, partially flux-split scheme. The scheme uses upwind differencing in the streamwise direction, ξ , and central differencing in the circumferential, η , and radial, ζ , directions. The F3D code can have either first-order or second-order accuracy in time and has second-order accuracy in space.

Implicit Method and Time Linearization

The fine grid spacing needed to resolve the viscous terms in the normal direction prescribes the use of implicit, rather than explicit methods. It is well known that the maximum time step that is allowed for stability in explicit time-marching schemes is proportional to the minimum grid spacing. Thus, the explicit time-step limit that is imposed by stability is excessively small for the viscous grids used in this study. Implicit methods overcome this restriction and permit a much larger time step. As a result, implicit methods require less computer time to obtain a viscous solution, even though the operation count per time step is high. In order to use a noniterative implicit algorithm for the solution of the thin-layer Navier–Stokes equations, a time linearization of the nonlinear vectors

must be performed. The linearization procedure is easily accomplished since the equations are written in conservation-law form. Taylor series expansion of the vectors $\hat{\mathbf{E}}$, $\hat{\mathbf{F}}$, $\hat{\mathbf{G}}$, and $\hat{\mathbf{S}}$ about $\hat{\mathbf{Q}}$ is performed

$$\begin{aligned} \hat{\mathbf{E}}^{n+1} &= \hat{\mathbf{E}}^n + \hat{\mathbf{A}}^n (\hat{\mathbf{Q}}^{n+1} - \hat{\mathbf{Q}}^n) + O(\Delta t^2) \\ \hat{\mathbf{F}}^{n+1} &= \hat{\mathbf{F}}^n + \hat{\mathbf{B}}^n (\hat{\mathbf{Q}}^{n+1} - \hat{\mathbf{Q}}^n) + O(\Delta t^2) \\ \hat{\mathbf{G}}^{n+1} &= \hat{\mathbf{G}}^n + \hat{\mathbf{C}}^n (\hat{\mathbf{Q}}^{n+1} - \hat{\mathbf{Q}}^n) + O(\Delta t^2) \\ \hat{\mathbf{S}}^{n+1} &= \hat{\mathbf{S}}^n + \hat{\mathbf{M}}^n (\hat{\mathbf{Q}}^{n+1} - \hat{\mathbf{Q}}^n) + O(\Delta t^2) \end{aligned} \quad (3.1)$$

where $\hat{\mathbf{A}}$, $\hat{\mathbf{B}}$, $\hat{\mathbf{C}}$, and $\hat{\mathbf{M}}$ are the Jacobian metrics defined by

$$\begin{aligned} \hat{\mathbf{A}}^n &= \left(\frac{\partial \hat{\mathbf{E}}}{\partial \hat{\mathbf{Q}}} \right)^n & \hat{\mathbf{B}}^n &= \left(\frac{\partial \hat{\mathbf{F}}}{\partial \hat{\mathbf{Q}}} \right)^n \\ \hat{\mathbf{C}}^n &= \left(\frac{\partial \hat{\mathbf{G}}}{\partial \hat{\mathbf{Q}}} \right)^n & \hat{\mathbf{M}}^n &= \left(\frac{\partial \hat{\mathbf{S}}}{\partial \hat{\mathbf{Q}}} \right)^n \end{aligned} \quad (3.2)$$

and the superscript n denotes evaluation at the n th time step where $t = n\Delta t$.

Applying the first-order Euler implicit formula and the linearizations of equation (3.1) to equation (2.24) results in a linear system

$$\begin{aligned} \left[\mathbf{I} + h \left(\frac{\partial}{\partial \xi} \hat{\mathbf{A}}^n + \frac{\partial}{\partial \eta} \hat{\mathbf{B}}^n + \frac{\partial}{\partial \zeta} \hat{\mathbf{C}}^n - \frac{1}{Re} \frac{\partial}{\partial \zeta} \hat{\mathbf{M}}^n + \right) \right] \Delta \hat{\mathbf{Q}} \\ = -h \left(\frac{\partial \hat{\mathbf{E}}}{\partial \xi} + \frac{\partial \hat{\mathbf{F}}}{\partial \eta} - \frac{\partial \hat{\mathbf{G}}}{\partial \zeta} - \frac{1}{Re} \frac{\partial \hat{\mathbf{S}}}{\partial \zeta} \right)^n + O(\Delta t^2) \end{aligned} \quad (3.3)$$

where \mathbf{I} is defined as the identity matrix, $h = \Delta t$, $\Delta \hat{\mathbf{Q}}^n = \hat{\mathbf{Q}}^{n+1} - \hat{\mathbf{Q}}^n$, and $\partial/\partial \xi$, $\partial/\partial \eta$, and $\partial/\partial \zeta$ are approximated by finite differencing.

Beam and Warming Algorithm

Replacing the spatial derivatives in equation (3.3) with central finite difference approximations produces a linear system which is a block heptadiagonal matrix with non-adjacent diagonals. In order to directly solve this system, an inversion of a block matrix which is proportional to the computational mesh is required. However, this is a very costly process and a simplification is performed which does not alter the accuracy of equation (3.3). Approximate factorization of the left-hand-side operator reduces the inversion to a sequence of one-dimensional inversions. Beam and Warming (ref. 17) developed a

factored algorithm to be applied to the two-dimensional Euler gasdynamic equations. The viscous terms were then added and the algorithm was applied to the two-dimensional compressible Navier–Stokes equations (ref. 18). The scheme was then applied to the transformed equations by Steger (refs. 19 and 20) to compute the flow around arbitrary two-dimensional geometries. The algorithm was later extended to solve the three-dimensional transformed thin-layer Navier–Stokes equations (ref. 21). The following form of the algorithm applies to both Euler implicit first-order and trapezoidal second-order time accuracy.

$$(\mathbf{I} + h\delta_\xi \hat{\mathbf{A}}^n)(\mathbf{I} + h\delta_\eta \hat{\mathbf{B}}^n) \times (\mathbf{I} + h\delta_\zeta \hat{\mathbf{C}}^n - hRe^{-1}\bar{\delta}_\zeta \hat{\mathbf{M}}^n) \Delta \hat{\mathbf{Q}}^n = \hat{\mathbf{R}}^n \quad (3.4)$$

where $\hat{\mathbf{R}}$ is

$$\hat{\mathbf{R}}^n = -\Delta t (\delta_\xi \hat{\mathbf{E}}^n + \delta_\eta \hat{\mathbf{F}}^n + \delta_\zeta \hat{\mathbf{G}}^n - Re^{-1}\bar{\delta}_\zeta \hat{\mathbf{S}}^n)^n \quad (3.5)$$

The numerical scheme has second-order spatial accuracy and either first- or second-order time accuracy. The first-order-accurate Euler implicit form is produced when h is equal to Δt , and the second-order-accurate trapezoidal form is produced when h is equal to $\Delta t/2$. Central differencing and a midpoint operator are denoted by δ and $\bar{\delta}$, respectively.

A series of three one-dimensional inversions is performed in order to advance the solution from time-step n to time-step $n + 1$.

$$\begin{aligned} (\mathbf{I} + h\delta_\xi \hat{\mathbf{A}}^n) \Delta \hat{\mathbf{Q}}^1 &= \hat{\mathbf{R}}^n \\ (\mathbf{I} + h\delta_\eta \hat{\mathbf{B}}^n) \Delta \hat{\mathbf{Q}}^2 &= \Delta \hat{\mathbf{Q}}^1 \\ (\mathbf{I} + h\delta_\zeta \hat{\mathbf{C}}^n - hRe^{-1}\bar{\delta}_\zeta \hat{\mathbf{M}}^n) \Delta \hat{\mathbf{Q}}^n &= \Delta \hat{\mathbf{Q}}^2 \\ \hat{\mathbf{Q}}^{n+1} &= \hat{\mathbf{Q}}^n + \Delta \hat{\mathbf{Q}}^n \end{aligned} \quad (3.6)$$

Each inversion requires solution of a linear system which is a block tridiagonal matrix. However, inversion of the three-tridiagonal equations is much faster than direct solution of the block heptadiagonal system. The factorized scheme can be optimized for vector computers by performing concurrent multiple line inversions and thereby further reducing the computation time per time step.

Flux Vector Splitting

Finite difference algorithms used to solve the conservation law form of the unsteady inviscid gasdynamic equations in subsonic flow regimes have a

limited class of spatial difference approximations that can be properly used. Only central difference operators lead to schemes that are simultaneously stable for both the positive and negative characteristic speeds or eigenvalues. In contrast, schemes based on one-sided difference operators are stable only for equations with single-signed eigenvalues. However, these schemes contain better dissipative and dispersive properties. The governing equations have eigenvalues of mixed signs in subsonic flow regimes and thus the flux vectors must be split prior to using the one-sided spatial difference operators.

Flux vector splitting can be performed since the flux vectors of equations (2.24) (for example \mathbf{E}) and its Jacobian matrix (in this case \mathbf{A}) are homogeneous function of degree one in \mathbf{Q} . That is

$$\mathbf{E}(\alpha \mathbf{Q}) = \alpha \mathbf{E}(\mathbf{Q}) \quad (3.7)$$

Applying Euler's theorem for homogeneous functions yields

$$\mathbf{E} = \frac{\partial \mathbf{E}}{\partial \mathbf{Q}} \mathbf{Q} = \mathbf{A} \mathbf{Q} \quad (3.8)$$

where \mathbf{A} is the Jacobian matrix equal to $\partial \mathbf{E} / \partial \mathbf{Q}$. Now the flux vector can be split into two subvectors

$$\mathbf{E} = \mathbf{E}^+ + \mathbf{E}^- \quad (3.9)$$

where \mathbf{E}^+ and \mathbf{E}^- correspond to the subvector associated with the positive and negative eigenvalues of \mathbf{A} , respectively (ref. 22). Any eigenvalue, λ_l , can be written as

$$\lambda_l = \lambda_l^+ + \lambda_l^- \quad (3.10)$$

where

$$\lambda_l^+ = \frac{\lambda_l + |\lambda_l|}{2} \quad \lambda_l^- = \frac{\lambda_l - |\lambda_l|}{2} \quad (3.11)$$

The subvectors \mathbf{E}^+ and \mathbf{E}^- can be differenced individually by using the appropriate one-sided scheme.

Now that flux vector splitting has been performed, upwind differencing is used in the streamwise direction for the flux-split term, while central differencing is retained in the circumferential and radial directions. This leads to a two-factored, partially flux-split algorithm.

$$\begin{aligned} & \left[\mathbf{I} + h\delta_\xi^b \left(\hat{\mathbf{A}}^+ \right)^n + h\delta_\zeta \hat{\mathbf{C}}^n - hRe^{-1}\bar{\delta}_\zeta \hat{\mathbf{M}}^n \right] \\ & \times \left[\mathbf{I} + h\delta_\xi^f \left(\hat{\mathbf{A}}^- \right)^n + h\delta_\eta \hat{\mathbf{B}}^n \right] \Delta \hat{\mathbf{Q}}^n = \hat{\mathbf{R}}^n \end{aligned} \quad (3.12)$$

where

$$\hat{\mathbf{R}}^n = -\Delta t \begin{bmatrix} \delta_\xi^b (\hat{\mathbf{E}}^+)^n + \delta_\xi^f (\hat{\mathbf{E}}^-)^n + \delta_\eta \hat{\mathbf{F}}^n \\ + \delta_\zeta \hat{\mathbf{G}}^n - Re^{-1} \bar{\delta}_\zeta \hat{\mathbf{S}}^n \end{bmatrix} \quad (3.13)$$

where $h = \Delta t$ for first-order time accuracy or $h = \Delta t/2$ for second-order time accuracy. The operators δ^b and δ^f are backward and forward three-point difference operators.

Similar to the procedure used to advance the Beam and Warming algorithm, two inversions are used to advance the solution from time-step n to time-step $n + 1$

$$\begin{aligned} \begin{bmatrix} \mathbf{I} + h\delta_\xi^b (\hat{\mathbf{A}}^+)^n + h\delta_\zeta \hat{\mathbf{C}}^n \\ -hRe^{-1} \bar{\delta}_\zeta \hat{\mathbf{M}}^n \end{bmatrix} \Delta \hat{\mathbf{Q}}^1 &= \hat{\mathbf{R}}^n \\ \begin{bmatrix} \mathbf{I} + h\delta_\xi^f (\hat{\mathbf{A}}^-)^n + h\delta_\eta \hat{\mathbf{B}}^n \end{bmatrix} \Delta \hat{\mathbf{Q}}^n &= \Delta \hat{\mathbf{Q}}^1 \\ \hat{\mathbf{Q}}^{n+1} &= \hat{\mathbf{Q}}^n + \Delta \hat{\mathbf{Q}}^n \end{aligned} \quad (3.14)$$

Numerical Dissipation

As mentioned, the finite difference scheme uses upwind differencing in the streamwise direction (ξ). This differencing has natural numerical dissipation since it is a one-sided method. In the circumferential (η) and radial (ζ) directions, the F3D code uses central differencing, which does not have natural numerical dissipation. Therefore, numerical dissipation terms, D_i and D_e , must be added in the η and ζ directions.

The numerical dissipation terms are a combination of second-order and fourth-order and are of the form (ref. 22)

$$\begin{aligned} D_e|_\eta &= (\Delta t)J^{-1} \left\{ \varepsilon_2 \bar{\delta} |\hat{\mathbf{B}}| \beta \bar{\delta} + \varepsilon_4 \bar{\delta} \frac{|\hat{\mathbf{B}}|}{1+\beta} \bar{\delta}^3 \right\} \bigg|_\eta \\ D_i|_\eta &= (\Delta t)J^{-1} \left\{ \varepsilon_2 \bar{\delta} |\hat{\mathbf{B}}| \beta \bar{\delta} + 2.5\varepsilon_4 \bar{\delta} \frac{|\hat{\mathbf{B}}|}{1+\beta} \bar{\delta}^3 \right\} \bigg|_\eta \end{aligned} \quad (3.15)$$

where

$$\beta = \frac{|\bar{\delta}^2 p|}{|(1 + \bar{\delta}^2)p|} \quad (3.16)$$

and where $\hat{\mathbf{B}}$ is the absolute value of the matrix $\hat{\mathbf{B}}$.

An analogous smoothing operator is applied in the ζ direction. In equations (3.15–3.16), $\bar{\delta}$ is a midpoint operator used with the viscous terms. Also p is the nondimensional fluid pressure and ε_2 is of $O(1 + M_\infty^\gamma)$ while ε_4 is of $O(0.01)$. The second-order dissipation terms are used to control numerical oscillations across shock waves, whereas the fourth-order terms are used elsewhere. The accuracy of the solution is improved by further scaling the fourth-order numerical smoothing terms by the nondimensional local velocity ratio, q/q_∞ . This reduces the numerical dissipation in the viscous layer of the body surface, where viscous dissipation controls the dispersion. Large amounts of numerical smoothing in this region may in fact modify the physical viscous terms and adversely affect the solution.

Numerical Algorithm

After applying linearization, approximate factorization, flux splitting, and numerical dissipation, the following implicit scheme for the thin-layer Navier–Stokes equations is obtained

$$\begin{aligned} &\left[\mathbf{I} + h\delta_\xi^b (\hat{\mathbf{A}}^+)^n + h\delta_\zeta \hat{\mathbf{C}}^n - hRe^{-1} \bar{\delta}_\zeta \hat{\mathbf{M}}^n - D_i|_\zeta \right] \\ &\times \left[\mathbf{I} + h\delta_\xi^f (\hat{\mathbf{A}}^-)^n + h\delta_\eta \hat{\mathbf{B}}^n - D_i|_\eta \right] \Delta \hat{\mathbf{Q}}^n \\ &= -\Delta t \left\{ \delta_\xi^b (\hat{\mathbf{E}}^+)^n + \delta_\xi^f (\hat{\mathbf{E}}^-)^n + \delta_\eta \hat{\mathbf{F}}^n + \delta_\zeta \hat{\mathbf{G}}^n - Re^{-1} \bar{\delta}_\zeta \hat{\mathbf{S}}^n \right\} \\ &\quad - \left(D_e|_\eta + D_e|_\zeta \right) \hat{\mathbf{Q}}^n \end{aligned} \quad (3.17)$$

The computations presented are run until a steady state solution is obtained. The convergence criteria are that the 1–2 norms should drop two to three orders of magnitude and the body forces should level off. The numerical algorithm can be fully vectorized to run on the Cray Y-MP/C90. F3D has been used successfully to model the flow over bodies of revolution at high incidence and the flow field over the F-18 aircraft (refs. 9, 23–27). Additional details of the development of this code can be found in references 16, 22, and 28.

Chimera Approach

The Chimera overset-grid scheme (refs. 29–31) is used to allow treatment of the multiple-zone grid (discussed in the next chapter). The Chimera overset method allows the use of different grid densities, flow solvers, or turbulence

models in the different zones of the flow depending on the physical requirement. In the Chimera approach there may be arbitrary “holes” in the grids or, in other words, points that lie within a body from another grid. The hole points may also include bordering points (ref. 31) which are later updated by interpolating the solution from the overset grid about the body which created the hole. At these points the partial difference equations are not used so that the points are changed. An array of values i_b is introduced to shut off the differencing scheme at hole points. At normal grid points $i_b = 1$, whereas at hole points $i_b = 0$. In the algorithm, the i_b array multiplies the dissipation terms and h ; that is

$$\begin{aligned} & \left[\mathbf{I} + i_b h \delta_\xi^b (\hat{\mathbf{A}}^+)^n + i_b h \delta_\zeta \hat{\mathbf{C}}^n - i_b h Re^{-1} \bar{\delta}_\zeta \hat{\mathbf{M}}^n - i_b D_i|_\zeta \right] \\ & \times \left[\mathbf{I} + i_b h \delta_\xi^f (\hat{\mathbf{A}}^-)^n + i_b h \delta_\eta \hat{\mathbf{B}}^n - i_b D_i|_\eta \right] \Delta \hat{\mathbf{Q}}^n \\ & = -i_b \Delta t \left\{ \delta_\xi^b (\hat{\mathbf{E}}^+)^n + \delta_\xi^f (\hat{\mathbf{E}}^-)^n + \delta_\eta \hat{\mathbf{F}}^n + \delta_\zeta \hat{\mathbf{G}}^n - Re^{-1} \bar{\delta}_\zeta \hat{\mathbf{S}}^n \right\} \\ & - i_b \left(D_e|_\eta + D_e|_\zeta \right) \hat{\mathbf{Q}}^n \end{aligned} \quad (3.18)$$

At a hole point, $i_b = 0$ and the algorithm reduces to

$$\Delta \hat{\mathbf{Q}}^n = 0 \quad (3.19)$$

or $\hat{\mathbf{Q}}^{n+1} = \hat{\mathbf{Q}}^n$ and thus $\hat{\mathbf{Q}}$ is unchanged.

4. Grid Generation Procedure and Boundary Conditions

A numerical simulation of forebody tangential slot blowing is performed on a generic chined forebody in support of a small-scale wind tunnel experiment. The experiment is performed (ref. 10) at the Cal Poly 3- by 4-Foot Low Speed Wind Tunnel. The dimensions of the wind tunnel model are shown in figure 1.4. The overall length of the model is 20.25 in. At the base the height and width are 8.086 in., and this value is used to as the reference length. The body reference area, 51.276 in.², is the area of a circle having a diameter equal to 8.086 in.

Surface and Volume Grids

The grid used for numerical prediction of the flow field about the generic chined forebody is shown in figure 4.1. The surface geometry and surface grid for the chined forebody are generated by spline representations using the S3D code (ref. 32), with grid point redistribution in both

the axial and the circumferential directions. The surface grid is clustered in regions where the flow gradients are expected to be the greatest. These regions include the chine area, where the flow is expected to separate. Next, the HYPGEN code (refs. 33 and 34) is used to generate a three-dimensional volume grid about the surface grid. This is accomplished by solving the three-dimensional hyperbolic grid generation equations, two orthogonal relations and one cell volume constraint.

Slot Configuration

The features of the wind tunnel model are resolved by the computational grid. The model contained a blowing slot on each side of the forebody. The slot was located on the upper surface of the model, behind a backward facing step of height 0.03 in., and oriented to blow toward the body leeward plane of symmetry (fig. 4.2). The total length of the blowing slot is 6 in., while the width is 0.005 in. Each slot was divided into six segments (each of 1 in. length), which were individually connected to valves. As a result, the length and location of the active slot could be varied. The first segment or blowing region, closest to the nose, is referred to *Slot 1*; the second segment as *Slot 2*, etc.

The computational slot geometry is modeled after the experimental blowing slot. In the computations, there is a slot grid on each side of the body grid. The computational slot grids are created in the same manner as the body grids, as described above. The blowing slot grids model the physical length and width of the experimental slots and the height of the backward-facing step. The active jet length is varied in the computations through the use of appropriate boundary conditions. A typical cross section of the top blowing slot grid overlapping the body grid is shown in figure 4.3.

Only one circumferential slot location, on the upper chine surface and blowing inboard, was tested in the experiment of reference 10. In order to determine whether an alternative circumferential slot location could be more effective in developing side forces and yawing moments on the body, computations were also carried out for a slot located on the lower chine surface and blowing tangentially outboard (fig. 4.4). This slot had the same axial location and extent of *Slot 1* (fig. 4.1) and was modeled on both sides of the body.

Chimera Overset Grid Scheme

Even with the large memory size available on the Cray YMP/C90 computer, it is not practical to use a single-zone, or single-block, body grid. Thus, a multi-zone grid will be used for the computations of the

forebody. The body grid is broken into four grids to decrease the required run-time core memory. The Chimera overset grid scheme (refs. 29–31) is used to unite the four body grids and the two slot grids into a single six-zone grid. Figure 4.5 shows the grid boundaries on the right half of the forebody. In addition, the Chimera method simplifies the creation of computational grids about complex geometries by dividing the physical domain into smaller regions which then can be more easily modeled. The overset grid method requires only that neighboring grids overlap each other. The overset method can also be used where there are regions which overlap only slightly; thus, the current implementation can also function in a blended overset and patched code (ref. 24). The Pegasus code (ref. 35) is used to establish communications among the interconnecting grids and to blank out any unwanted regions.

Final Form of the Computational Grids

The four-zone body volume grid system is symmetric about the plane of symmetry. Each of the two front body grids consists of 40 axial points, 123 circumferential points, and 50 normal points, whereas each of the two back body grids consists of 12 axial points, 123 circumferential points, and 50 normal points. The grid extends eight reference lengths normal to the body; thus, the outer boundary is sufficiently far away so that the effect of the outer boundary on the flow is minimized. The grid extends seven body lengths upstream from the nose.

In the current study, two different multi-zone grids, each with six zones, are created: one for the slot located on the top surface of the body to match the experimental model and one for the slot located on the bottom surface for numerical analysis. Both slot configurations are included on both sides of the body. To model the experimental slot configuration, two slot grids are added on the upper surface of the body, one on each side of the body. Each of the two slot grids on the top surface consists of 55 axial points, 40 circumferential points, and 39 normal points. The six-zone computational grid modeling the top slot has a total of 811,200 points. Similarly, to model outward blowing on the bottom surface, two bottom slot grids are added to the four-zone body grid. Each of the two slot grids located on the bottom surface consists of 55 axial points, 86 circumferential points, and 39 normal points, and the resulting six-zone grid contains a total of 1,008,540 points.

Boundary Conditions

In this numerical simulation, the boundary conditions applied are no-slip with no normal velocity at the body surface, which corresponds to the $\zeta = 1$ plane. Free-stream conditions are maintained at the outer boundaries. The exit boundary uses a simple zero-axial-gradient extrapolation condition. The outer boundary is sufficiently far away from the generic chined forebody, thereby minimizing the effects of the outer boundary on the flow of the chined forebody. Chimera (refs. 29–31) and Pegasus (ref. 35) are used to obtain boundary conditions at grid boundaries that overlap neighboring grids. In the slot grids' outer boundaries, an overlap of approximately one grid point is used except at the surface. In order to reduce the computational time required to converge a solution with blowing, the no-blowing case solution is used as the initial flow conditions for the blowing computations.

Slot Boundary Conditions

Jet mass flow ratios, MFR , equal to those used in the experiment (ref. 10) are used in the numerical study. MFR is defined as

$$MFR = \frac{\dot{m}_{jet}}{\dot{m}_{ref}} = \frac{\rho_{jet} V_{jet} S_{jet}}{\rho_{\infty} V_{\infty} S_{ref}} \quad (4.1)$$

where V is velocity, S is area, the subscript ref denotes a reference value, and the subscript ∞ denotes free-stream conditions. The current forebody computations utilize boundary conditions that are physically realistic. The jet in the slot grids is modeled computationally by using boundary conditions to introduce the jet exit conditions into the flow field. If the jet exit Mach number is less than sonic, the jet total pressure and total temperature are inputs to the flow solver. The exit pressure is obtained by extrapolating the pressure from the local external flow pressure at the jet exit. The jet exit Mach number is then obtained by using the isentropic relations for one-dimensional flow of inviscid gas (ref. 36). For sonic jets, the flow is assumed to choke at the exit and the jet pressure is obtained from isentropic relations using the jet total pressure and the total temperature as inputs. In either case, in order to match the experimental mass flow ratios, the total pressure of the jet is increased, thereby increasing the jet density, until the desired jet mass flow rate is obtained.

5. Results and Discussion

Flow at high angle of attack is dominated by large regions of three-dimensional separated flows, as discussed in section 1. This leads to a loss of aircraft control power as the conventional control surfaces become engulfed in the separated flow. However, forces and moments can be generated by manipulating the strong vortices and used to control the aircraft. Forebody tangential slot blowing is one method of vortex manipulation, where air is blown from a thin slot located on the forebody tangential to the surface. The jet forces the flow field to change about the aircraft, which generates a side force and yawing moment that can be used to control the aircraft.

A study of this flow control method is performed on a generic chined forebody using computational fluid dynamics. The F3D code is used to solve the flow field about a generic chined forebody at two high angles of attack, $\alpha = 30$ deg and $\alpha = 40$ deg at $M_\infty = 0.2$ and a Reynolds number (based on free-stream conditions and body reference length) of $Re_d = 2.81 \times 10^5$. Comparisons are made with experimental data obtained at $\alpha = 30$ deg and $\alpha = 40$ deg at $M_\infty = 0.06$ and $Re_d = 2.81 \times 10^5$. The computational Mach number was chosen to be higher than the experimental value to reduce computational convergence time. However, since the Mach numbers are low, the flows are essentially incompressible (ref. 36) and thus the results can be compared. In all cases presented, the computed flow is treated as being fully turbulent.

The results of the study are presented in the following subsections. The first subsection presents a grid sensitivity study. In the next subsection, the no-blowing solutions, which illustrate the main features of the flow field about the generic chined forebody and provide baselines for comparison with the blowing cases, are discussed. The last subsection discusses the results of the blowing solutions, such as comparing experimental and numerical data as MFR and angle of attack increase, analyzing flow patterns and helicity density contours, and, last, the effects of slot position, both axially and circumferentially. Table 5.1 shows the numerical solutions computed, along with the labels which will be used to refer to them.

Grid Sensitivity Study

A grid sensitivity study is conducted to determine the grid density required in the circumferential (η) direction to resolve the physical flow features. For this particular study, a half-body, single-zone grid is used. In all other remaining studies a full-body, six-zone grid is utilized. No-blowing solutions obtained using the F3D flow solver at flow conditions of $\alpha = 30$ deg, $M_\infty = 0.2$, and

$Re_d = 2.81 \times 10^5$ are examined. Three grids are used in the computations (fig. 5.1): a coarse grid consisting of 50 axial \times 63 circumferential \times 50 radial points; a medium density grid with $50 \times 123 \times 50$ points; and a fine density grid with $50 \times 243 \times 50$ points. The medium grid is obtained by doubling the points in the η direction of the coarse grid, and the fine grid is obtained by doubling the η direction points of the medium grid.

Massless particles are released just above the surface and are integrated in time using the velocity field to determine the subsequent motion. The particles are restricted to stay close to the surface. This effectively produces limiting streamlines which illustrate the surface flow topology. The computed surface flow pattern obtained from the coarse grid solution is shown in figure 5.2. As discussed in section 1, the chined forebody has a fixed primary separation line at the chine which is not clearly shown in figure 5.2. The surface flow pattern shows a secondary separation line and a small tertiary separation line near the aft of the body. Figure 5.3 shows the solution for the medium density grid. Here, the secondary separation line and the tertiary separation line are well defined. Reattachment lines are also shown clearly in the medium density grid.

Helicity density is defined (ref. 37) as the scalar product of the velocity and vorticity vectors and is used to illustrate the size and shape of the vortices in the flow field. The helicity density contours provide some insight into the behavior of the vortices. The contour lines represent the strength of the vortices. Helicity density contours shown in cross sections normal to the body at fuselage station $f_s = 1.0, 4.0$, and 15.5 in figures 5.2 and 5.3 indicate that the medium density grid solution resolves the tertiary vortex as seen in the second and third forebody stations, whereas the coarse density grid solution does not. It should be noted that the forebody stations are slightly magnified to clearly show the helicity density contours.

Increasing grid density further shows no further improvement in the surface flow topology or helicity density contours (fig. 5.4). The surface flow patterns obtained from the medium and fine density grid solutions are similar, resolving the secondary and tertiary separation lines. There are small local differences near the aft of the body; however, these differences are slight and do not affect the overall physics of the flow. The helicity density contours in figures 5.3 (medium density grid) and 5.4 (fine density grid) indicate both grids resolve the same vortex structure and strength. The main features of the flow field are clearly resolved using the medium density grid. Thus, in order to minimize the CPU time required to

converge a solution, the medium density grid will be used for all further no-blowing and blowing cases.

No-Blowing Solutions

Solutions of the flow field about the generic chined forebody without blowing are computed assuming fully turbulent flow and used as baseline solutions from which to compute the blowing solutions. A full body, multi-zone grid is used in the following studies. The major features of the computed no-blowing flow field about the forebody at $\alpha = 30$ deg are shown in figure 5.5. Primary cross-flow separation lines occur at the chine line, and extend along the entire length of the body. In addition, the secondary and tertiary cross-flow separation lines extend from the nose of the forebody to the end of the forebody. Surface flow patterns are almost identical to those of the half-body, single-zone solution (fig. 5.3) except that a discontinuity in the secondary separation line appears near the middle of the body. This discontinuity is a result of the post-processor, which has limitations in dealing with multi-zone grids. However, the computed secondary separation line is, in fact, continuous.

Helicity density contours at three fuselage stations, $f_s = 1.0, 4.0$, and 15.5 at $\alpha = 30$ deg, are shown in figure 5.5. The helicity density contours show that the flow field is symmetric. The primary vortices grow larger and more diffuse in the axial direction. The primary vortices also move away from the forebody. The secondary vortex, which is smaller and weaker, lies underneath the primary vortex and rotates in the opposite direction of the primary one.

When the angle of attack is increased to $\alpha = 40$ deg, the surface flow patterns show that the flow field is similar to the $\alpha = 30$ deg solution except that a fourth cross-flow separation line appears near the back of the forebody (fig. 5.6). The helicity density contours for $\alpha = 40$ deg are shown in figure 5.6 at the same contour levels as in figure 5.5. By comparing the helicity density contours, it is shown that the vortices are stronger in the $\alpha = 40$ deg case. The increased strength of the vortices and the fixed position of the primary vortex are such that a fourth separation line appears near the back of the forebody for $\alpha = 40$ deg.

Blowing Solutions

Solutions were computed for flow with tangential slot blowing from the starboard side (pilot's view) of the body. The blowing slot is 1 in. in length, starting 0.5 in. from the nosetip and extending aft. The slot is located on the upper surface of the chine (fig. 1.4) and the blowing was directed inboard toward the leeward symmetry plane,

matching one of the slot configurations tested in the small-scale wind tunnel (ref. 10) test. The computational jet mass flow ratios (MFR) were chosen equal to those of the experiment.

In this subsection, computational and experimental data are compared to determine the effect of MFR and angle of attack on blowing effectiveness. Next, the computational solutions are analyzed using surface flow patterns, helicity density contours, and off-surface instantaneous streamlines. Finally, the effect of slot placement, axially and circumferentially, will be presented.

Comparison of numerical and experimental results–

As discussed, blowing perturbs the nominally symmetric no-blowing forebody flow field, resulting in development of a side force and yawing moment. The variation of the incremental of side-force coefficient (ΔC_Y) with MFR for $\alpha = 30$ deg is shown in figure 5.7. ΔC_Y is defined to be

$$\Delta C_Y = (C_Y)_{blowing} - (C_Y)_{no-blowing} \quad (5.1)$$

The coefficient of side force is

$$C_Y = \frac{Y}{q_\infty S_{ref}} \quad (5.2)$$

where Y is the side force, q_∞ is the free-stream dynamic pressure, and S_{ref} is the reference area (fig. 1.4). The computational and experimental results show the same trends: as the MFR increases, ΔC_Y also increases. However, the computational results underpredict the magnitude of ΔC_Y .

Similarly, the incremental yawing moment coefficient, ΔC_n , is defined to be

$$\Delta C_n = (C_n)_{blowing} - (C_n)_{no-blowing} \quad (5.3)$$

where

$$C_n = \frac{N}{q_\infty S_{ref} L_{ref}} \quad (5.4)$$

Here, N is the yawing moment and L_{ref} is the reference length (fig. 1.4). The moments are taken about a moment center located at the rear of the forebody (fig. 1.4). The variation of ΔC_n with MFR for $\alpha = 30$ deg is shown in figure 5.8. The incremental yawing moment increases as the mass flow ratios increase for both the experimental and computational data. Again, the computational results underpredict the yawing moment. The discrepancy in the yawing moment is proportionally greater than that in the side force. This indicates that the differences are greater toward the nose of the forebody, in the blowing region, since the moment center is located at the back of the body.

Figures 5.9 and 5.10 show the analogous variation of ΔC_Y and ΔC_n with MFR for $\alpha = 40$ deg. For $\alpha = 40$ deg, the experimental data show trends similar to those seen at $\alpha = 30$ deg. The experimental ΔC_Y and ΔC_n increase smoothly with increasing MFR . The computed results, however, show three distinct regions of effectiveness. In the first region (denoted as Region I), low blowing rates produce a negative ΔC_Y and ΔC_n . In Region II, ΔC_Y and ΔC_n increase with increasing MFR until a maximum is reached. In Region III, further increases in MFR cause a reduction in ΔC_Y and ΔC_n . Similar trends are observed in experiments using the F/A-18 with jet and slot blowing (ref. 38). These regions will be discussed further in the following subsection. At this angle of attack, the numerical results overpredict ΔC_Y and ΔC_n . In general, the computed results are in better agreement with experiment than at $\alpha = 30$ deg, except at the low MFR values.

As the angle of attack of the forebody is increased, the flow field becomes more sensitive to perturbations. This effect is shown in figure 5.11, which summarizes the data shown in figures 5.8 and 5.10. As the angle of attack is increased, a greater change in the incremental yawing moment is produced for a given MFR . Both the present computations and the experiment results show this trend. Similar trends were observed in experiments using the F/A-18 (ref. 38) and another chined forebody (ref. 39). However, the experimental results for the present configuration do not show as great an increase in sensitivity as displayed by the computed results.

As stated above, a fixed strength jet becomes increasingly effective as the angle of attack is increased. This is apparent in the helicity density contours shown in figure 5.12. Helicity density contours in a cross-flow plane at fuselage station $f_s = 4.0$ are shown for no-blowing and blowing solutions for $\alpha = 30$ deg and $\alpha = 40$ deg. In the no-blowing solutions, the vortices are stronger at $\alpha = 40$ deg (fig. 5.12(b)) than at $\alpha = 30$ deg (fig. 5.12(a)). When blowing is turned on, the $\alpha = 30$ deg case (fig. 5.12(c)) shows that the primary vortex on the blowing side (left side of figure 5.12(c)) moves toward the surface, whereas the primary vortex on the non-blowing side moves away from the surface and becomes weaker as compared to the no-blowing solution (fig. 5.12(a)). In the $\alpha = 40$ deg case (fig. 5.12(d)), movement of the primary vortex is similar to $\alpha = 30$ deg case, except that the changes in the strength of the vortices are larger. This bigger change, in turn, leads to larger values of ΔC_Y and ΔC_n . For tangential slot blowing it appears that changes in both strength and position of the vortices are important in the effectiveness of blowing. This is different from outward blowing where the

change in vortex position is more effective than manipulating vortex strength (ref. 40).

Analysis of computational flow field– In order to understand the flow physics causing the curious reversal of the yawing moment at low blowing rates, and the drop-off in yawing moment at the largest blowing rates, blowing solutions from each region shown in figures 5.9 and 5.10 are analyzed. These include flows for $MFR = 0.23 \times 10^{-3}$ (Region I), $MFR = 1.49 \times 10^{-3}$ (Region II), and $MFR = 4.17 \times 10^{-3}$ (Region III). The sectional side-force coefficient distributions along the body, c_Y (fig. 5.13), and sectional yawing-moment coefficient distributions, c_n (fig. 5.14), show the effect of blowing in each region. At the lowest MFR (Region I), c_Y is negative for all stations along the body, and thus the total C_Y is negative, as seen in figure 5.9. For $MFR = 1.49 \times 10^{-3}$ (Region II), the sectional side force is always positive and increases in the axial direction. For $MFR = 4.17 \times 10^{-3}$ (Region III), the sectional side force is negative in the blowing region and then becomes positive downstream of the slot. However, the positive sectional c_Y is much smaller than for $MFR = 1.49 \times 10^{-3}$. The sectional yawing-moment distribution (fig. 5.14) shows similar results.

The behavior of the sectional side-force distributions can be explained in part by examining the surface flow patterns and helicity density contours. Upon comparing the computed surface flow patterns for solutions with $MFR = 0.23 \times 10^{-3}$ (fig. 5.15), $MFR = 1.49 \times 10^{-3}$ (fig. 5.16), and $MFR = 4.17 \times 10^{-3}$ (fig. 5.17) with the no-blowing solution (fig. 5.6), it is seen that the largest changes in the flow field occur in the blowing region near the nose. The separation lines aft of the blowing region do not appear to greatly change positions. Recall that the blowing slot is located on the right side of the body (left side of the body in the helicity density contours). A closer examination of the surface flow patterns near the nose (fig. 5.18) shows that at the lowest MFR (fig. 5.18(b)) the secondary cross-flow separation occurs inboard of the location observed in the no-blowing solution (fig. 5.18(a)). The attachment lines appear to remain in approximately the same positions. In Region II, the surface flow pattern shows that the jet remains attached due to the Coanda effect. The interaction between the upper surface flow and the jet causes an entrainment of the lower momentum upper surface boundary layer flow (refs. 41–43). In the attached region, the surface pressure is lower than that at corresponding points on the non-blowing side, which causes a side force toward the blowing side. Finally, in Region III, the secondary

separation line on the blowing side near the tip of the nose has been severely altered. There are no visible changes on the nonblowing side. The attachment lines move toward the nonblowing side of the forebody.

The corresponding helicity density contours for the three MFR s of figures 5.13 and 5.14 are shown in cross-flow planes at three axial locations on the forebody in figures 5.15–5.17. All three cases show that the helicity density contours grow larger and more diffuse in the axial direction. The first fuselage station, $f_s = 1.0$, is located in the middle of the blowing region. The helicity density contours at $f_s = 4.0$ and $f_s = 15.5$ for the lowest MFR ($MFR = 0.23 \times 10^{-3}$) show that the effect from blowing is less downstream than upstream (fig. 5.15). The contours for fuselage station $f_s = 4.0$ and $f_s = 15.5$ for $MFR = 1.49 \times 10^{-3}$ (fig. 5.16) show that the blowing side vortices move closer to the surface and the nonblowing side vortices move away from the surface when compared to the no-blowing solution (fig. 5.6) which causes tangential slot blowing to be effective in this region. At the highest MFR ($MFR = 4.17 \times 10^{-3}$), the helicity contours at fuselage station $f_s = 4.0$ (fig. 5.17) show that the under-expanded jet separates and reattaches to form a vortex in the middle of the forebody.

A close-up view of the helicity density contours in the cross-flow plane at fuselage station $f_s = 1.0$ for the no-blowing and the three blowing solutions is shown in figure 5.19. The no-blowing case (fig. 5.19(a)) is symmetric as described in the previous subsection. At $MFR = 0.23 \times 10^{-3}$ (fig. 5.19(b)), the low-energy jet causes the primary vortex on the blowing side to move away from the surface, and the strength of the vortex is reduced. At the same time, the nonblowing side vortex moves toward the surface, producing a small side force and yawing moment toward the nonblowing side of the body. For $MFR = 1.49 \times 10^{-3}$ (fig. 5.19(c)), the primary vortex on the blowing side is entrained by the jet and moves downward toward the surface due to the Coanda effect. The nonblowing side vortex moves away from the surface. Here the movement of the vortices and the resulting lower pressure region on the blowing side cause a side force and yawing moment toward the blowing side. At the highest MFR , $MFR = 4.17 \times 10^{-3}$, the jet is so strong that it acts to separate, rather than entrain, the blowing-side vortex flow (fig. 5.19(d)). The blowing-side vortex moves away from the surface and the nonblowing-side vortex moves toward the surface. This causes c_Y and c_n to be negative in the region of the jet, as shown in figures 5.13 and 5.14, respectively. At this high mass flow ratio, the pressure at the jet exit is about ten times greater than the free-stream pressure. Hence the jet rapidly expands after leaving the blowing slot (ref. 43),

which causes the jet to separate, thereby pushing the primary vortex away from the surface.

The behavior of the primary vortex is shown in figure 5.20 using off-surface instantaneous streamlines. The black and dark gray particle traces represent the blowing side and nonblowing side vortices, respectively. The light gray streamlines represent streamlines emanating from the blowing slot. For $MFR = 0.23 \times 10^{-3}$ (fig. 5.20(b)), the jet is entrained into the blowing side primary vortex and there appears to be no visible effect on the nonblowing side vortex. For $MFR = 1.49 \times 10^{-3}$ (fig. 5.20(c)), the Coanda effect is clearly seen as the blowing jet moves along the surface merging with the nonblowing-side vortex and entrains the blowing side primary vortex. The position of the nonblowing-side vortex moves outboard. For the highest MFR , $MFR = 4.17 \times 10^{-3}$ (fig. 5.20(d)), the blowing jet separates from the surface near the centerline and creates a vortex in the middle of the forebody which entrains streamlines from the primary blowing side vortex. The nonblowing side vortices are hardly affected.

Effect of axial location of the blowing slot– It is recognized (refs. 1, 6, 10, and 44) that perturbations located close to the nose are more effective in developing asymmetric flows over the body than distances located farther downstream. In the wind tunnel experiment conducted at Cal Poly (ref. 10), it was found that the most effective slot configuration of those tested on the generic chined forebody was a slot 1 in. long located 0.5 in. from the tip of the nose (referred to as *Slot 1*) and blowing tangentially toward the leeward symmetry plane. To investigate the effect of axial slot location computationally, solutions were obtained for an additional slot configuration (which had also been tested experimentally). This slot (referred to as *Slot 2*) had the same 1 in. length as *Slot 1*, but extended rearward from a point 1.5 in. from the tip of the nose. The slot configurations are shown in figure 1.4.

The variations of ΔC_Y (fig. 5.21) and ΔC_n (fig. 5.22) with MFR for the two slot configurations are similar. The computed results for both slot configurations show a force reversal at low MFR s, followed by increasing ΔC_Y and ΔC_n with increasing MFR . *Slot 1* produces a larger magnitude of ΔC_Y and ΔC_n for a given MFR than does *Slot 2*. This trend is clearly seen at the higher MFR s and was seen in both the numerical and experimental results. It is also consistent with results obtained by Degani and Schiff, who conducted a numerical analysis on a slender body of revolution and found that small disturbances near the tip of the nose produce greater effects on the flow field than disturbances placed farther aft (ref. 45).

The computed surface flow pattern for *Slot 2* with $MFR = 1.49 \times 10^{-3}$ (fig. 5.23) shows the effect of the jet to be localized about the blowing region. The separation lines aft of the blowing region are in essentially the same location as seen in the no-blowing case (fig. 5.6) and for blowing from *Slot 1* at the same MFR (fig. 5.16). Figure 5.23 also shows the helicity density contours for three forebody stations. The first fuselage station is located forward of the blowing region and thus does not show any asymmetry due to the jet. The contours at fuselage stations $f_s = 4.0$ and $f_s = 15.5$ both show that the blowing-side vortex moves closer to the surface and the nonblowing-side vortex moves away. As was seen for blowing from *Slot 1*, this effect again decreases in the axial direction.

The helicity density contours at $f_s = 4.0$ (fig. 5.24) show that blowing from *Slot 1* (fig. 5.24(b)) causes a greater change from the symmetric no-blowing case (fig. 5.24(a)) than does blowing from *Slot 2* (fig. 5.24(c)). Not only did the blowing-side and nonblowing-side vortices move closer and away from the surface, respectively, but the Coanda effect is stronger in *Slot 1*, since more of the flow is entrained and moves closer to the middle of the forebody. This can be also be seen in the instantaneous streamlines in figure 5.25 where more of the blowing side vortices are entrained by the blowing jet from *Slot 1* than from *Slot 2*.

Effect of circumferential location of the blowing slot

Only one circumferential slot location, on the upper chine surface and blowing inboard, was tested in the Cal Poly wind tunnel experiment (ref. 10). In order to determine whether an alternative circumferential slot location could be more effective in developing side forces and yawing moments on the body, computations were carried out for a slot located on the lower chine surface and blowing tangentially outboard (fig. 4.4). This slot had the same axial location and extent as *Slot 1*.

As discussed in section 1, the typical effect of tangential slot blowing from the top surface is to move the blowing-side vortex closer to the surface and the nonblowing side vortex away. However, if blowing is from the bottom surface, the opposite occurs (fig. 1.3). Outboard blowing from the bottom slot moves the blowing-side vortex away from the body, and thus produces a side force and yawing moment directed away from the blowing side.

Blowing from the upper slot produces a greater change in side force and yawing moment for a given MFR than does blowing from the bottom slot, as shown in figures 5.26 and 5.27. As seen earlier, at the low MFR s blowing from the upper slot produces a force reversal; however, this is not found in the bottom-blowing results. This is probably due to the different method by which force is generated.

Blowing from the bottom does not require entrainment of the vortex toward the surface. Therefore, with bottom blowing, at low MFR values, the blowing-side vortex is still pushed away from the surface.

Figure 5.28 presents the surface flow pattern and helicity density contours for bottom slot blowing at $MFR = 1.49 \times 10^{-3}$, analogous to those shown for upper-slot blowing in figure 5.16. Comparing the surface flow patterns for blowing from the top (fig. 5.16) and from the bottom (fig. 5.28) slots, for the bottom-blowing case, the secondary and tertiary separation lines immediately aft of the blowing region are moved toward the leeward plane of symmetry. In both blowing cases, the separation line locations in the aft portion of the forebody do not differ substantially from the no-blowing results. The helicity density contours obtained for the bottom-blowing case (fig. 5.28) show that in contrast to the upper-slot blowing case (fig. 5.16), the blowing-side vortex moves away from the surface and the nonblowing-side vortex moves closer to the surface.

6. Conclusions

A computational investigation of tangential slot blowing for forebody flow control on a generic chined forebody has been performed. The effects of several parameters on the ability of pneumatic flow control to generate side forces and yawing moments on a forebody with fixed separation lines were studied. These parameters include jet mass flow ratios, angle of attack, and slot position in the axial and circumferential direction. The computed results were compared with available wind tunnel test data to determine the accuracy of the numerical analysis.

Solutions were obtained by solving the Reynolds-averaged, thin-layer, Navier–Stokes equations. A grid sensitivity test was conducted using nonblowing solutions to determine the appropriate circumferential grid density. A total of twenty-eight blowing solutions have been obtained, using three blowing slot locations near the tip of the body; two located above the chine, the other below the chine. Two angles of attack are studied, $\alpha = 30$ deg and $\alpha = 40$ deg. Various jet mass flow ratios are investigated for each slot location and angle of attack.

The computed results were compared to results from a low-speed, low-Reynolds-number experiment. The computed results show reasonable agreement with the trends observed in the experiment.

The computational and experimental results indicate that, at a given mass flow rate, the side forces and yawing moments generated by slot blowing increase as the body angle of attack increases. At high angles of attack, the

flow becomes highly sensitive to small changes in the geometry or flow field. Therefore, for a given perturbation, in this case the jet, a larger change was produced as the angle of attack increases.

In general, the computations indicated that the side forces and yawing moments generated by slot blowing increased as the jet mass flow ratio increased for $\alpha = 30$ deg. At the higher angle of attack $\alpha = 40$ deg, three distinct regions were observed in the results computed for the slot located above the chine and closest to the tip of the nose. The first region showed that at low *MFR*s tangential slot blowing produced a negative side force and nose-left yawing moment. This was caused by the inability of the jet to move the vortices on the blowing side close to the surface. The next region showed that ΔC_Y and ΔC_n were positive and increased as *MFR* increased due to the Coanda effect. The last region shows a decrease in ΔC_Y and ΔC_n at the high *MFR*s which was caused by the blowing jet being underexpanded.

The computational and experimental results showed that, for the slots located above the chine, greater changes of side forces and yawing moments were produced by the slot located closest to the tip of the nose. This agreed with the results of previous work which reported that small disturbances near the tip of the nose produced greater effects on the flow field than if placed farther aft.

Tangential slot blowing from the bottom surface produced a nose-left yawing moment when blowing was from the right side of the forebody. In contrast, blowing from the slot on the top surface produced a nose-right yawing moment when the blowing was from the right side. At a given mass flow ratio and angle of attack, tangential slot blowing from the top surface was found to be more efficient at generating yawing moments than blowing from the bottom surface. It appears to be more efficient to generate a side force and yawing moment by moving the blowing side vortices closer to the surface and moving the nonblowing side vortices away, as is the case with blowing from the top.

Numerical analysis shows that tangential slot blowing on a generic chined forebody can be used as a means of forebody flow control to generate side force and yawing moment. Forebody flow control will improve the performance of future aircraft designs.

References

1. Boalbey, R. E.; Ely, W.; and Hahne, D. E.: High Angle of Attack Stability and Control Concepts for Supercruise Fighters. NASA CP-3149, High-Angle-of-Attack Technology, 1992, pp. 759–784.
2. Fuhs, A. E.: Radar Cross-Section Lectures. American Institute of Aeronautics and Astronautics, New York.
3. Schiff, L. B.; Cummings, R. M.; Sorenson, R. L.; and Rizk, Y. M.: Numerical Simulation of High-Incidence Flow Over the Isolated F-18 Fuselage Forebody. *J. Aircraft*, vol. 28, no. 10, 1991, pp. 609–617.
4. Gee, K.: Investigation of Three-Dimensional Separated Flow About a Geometrically Simple Body. Master of Science Thesis, California Polytechnic State University, June 1990.
5. Cummings, R. M.; Rizk, Y. M.; Schiff, L. B.; and Chaderjian, N. M.: Navier–Stokes Predictions of the Flowfield Around the F-18 (HARV) Wing and Fuselage at Large Incidence. AIAA Paper 90-0099, Jan. 1990.
6. Lanser, W. R.; and Meyn, L. A.: Forebody Flow Control on a Full-Scale F/A-18 Aircraft. AIAA Paper 92-2674, June 1992.
7. Rao, D. M.. and Puram, C. K.: Chine Forebody Vortex Manipulation by Mechanical and Pneumatic Techniques on a Delta Wing Configuration. AIAA Paper 91-1812, June 1991.
8. Malcolm, G. N.; and Ng, T. T.: Aerodynamic Control of Fighter Aircraft by Manipulation of Forebody Vortices. AGARD-CP-497, Manoeuvring Aerodynamics, Paper 15, 1991.
9. Gee, K.; Rizk, Y.; Murman, S. M.; Lanser, W. R.; Meyn, L. A.; and Schiff, L. B.: Analysis of a Pneumatic Forebody Flow Control Concept About a Full Aircraft Geometry. AIAA Paper 92-2678, June 1992.
10. Cummings, R. M.; Schiff, L. B.; and Duino, J.: Experimental Investigation of Tangential Slot Blowing on a Generic Chined Forebody. AIAA Paper 94-3477, Aug. 1994.

11. Anderson, D. A.; Tannehill, J. C.; and Pletcher, R. H.: Computational Fluid Dynamics and Heat Transfer. Hemisphere Publishing Co., 1984.
12. Baldwin, B.; and Lomax, H.: Thin-Layer Approximation and Algebraic Model for Separated Turbulent Flows. AIAA Paper 78-257, Jan. 1978.
13. Degani, D.; and Schiff, L. B.: Computation of Turbulent Supersonic Flows Around Pointed Bodies Having Crossflow Separation. *J. Computational Physics*, vol. 66, no. 1, 1966, pp. 173–196.
14. Gee, K.; Cummings, R. M.; and Schiff, L. B.: Turbulence Model Effects on Separated Flow About a Prolate Spheroid. *AIAA J.*, vol. 30, no. 3, 1992, pp. 655–664.
15. Cebeci, T.: Calculation of Compressible Turbulent Boundary Layers with Heat and Mass Transfer. AIAA Paper 70-741, June 1970.
16. Steger, J. L.; Ying, S. X.; and Schiff, L. B.: A Partially Flux Split Algorithm for Numerical Simulation of Compressible Inviscid and Viscous Flow. Proceedings, Workshop on Numerical Methods in Fluid Dynamics, Davis, Calif., July 1986.
17. Beam, R. M.; and Warming, R. F.: An Implicit Finite-Difference Algorithm for Hyperbolic Systems in Conservation Law Form. *J. Computational Physics*, vol. 22, no. 1, 1978, pp. 87–110.
18. Beam, R. M.; and Warming, R. F.: An Implicit Factored Scheme for the Compressible Navier–Stokes Equations. *AIAA J.*, vol. 16, no. 4, 1978, pp. 393–402.
19. Steger, J. L.: Implicit Finite Difference Simulation of Flow About Arbitrary Geometries with Application to Airfoils. AIAA Paper 77-665, June 1977.
20. Steger, J. L.: Implicit Finite-Difference Simulations of Flow About Arbitrary Two-Dimensional Geometries. *AIAA J.*, vol. 16, no. 7, 1978, pp. 679–686.
21. Pulliam, T. H.; and Steger, J. L.: Implicit Finite-Difference Simulations of Three-Dimensional Compressible Flow. *AIAA J.*, vol. 18, no. 2, 1980, pp. 159–167.
22. Ying, S. X.; Bagonoff, D.; Steger, J. L.; and Schiff, L. B.: Numerical Simulation of Unsteady, Viscous, High Angle-of-Attack Flows Using Partially Flux-Split Algorithm. AIAA Paper 86-2179-CP, Aug. 1986.
23. Rizk, Y. M.; Schiff, L. B.; Gee, K.; and Cummings, R. M.: Numerical Simulation of the Viscous Flow Around the F-18 at High Angles of Attack. AIAA Paper 90-2999, Aug. 1990.
24. Rizk, Y. M.; and Gee, K.: Numerical Prediction of the Unsteady Flowfield Around the F-18 Aircraft at Large Incidence. AIAA Paper 91-0020, Jan. 1991.
25. Gee, K.; Rizk, Y. M.; and Schiff, L. B.: Effect of Forebody Tangential Slot Blowing on Flow About a Full Aircraft Geometry. AIAA Paper 93-2962, July 1993.
26. Murman, S. M.; Schiff, L. B.; and Rizk, Y. M.: Numerical Simulation of the Flow About an F-18 Aircraft in the High-Alpha Regime. AIAA Paper 93-3405, Aug. 1993.
27. Murman, S. M.: Computational Investigation of Slot Blowing for Fuselage Forebody Flow Control. Master of Science Thesis, California Polytechnic State University, 1991.
28. Ying, S. X.: Three-Dimensional Implicit Approximately Factored Schemes for Equations in Gasdynamics. Doctor of Philosophy Thesis, Stanford University, 1986. (Also SUDAAR 557, June 1986.)
29. Benek, J. A.; Buning, P. G.; and Steger, J. L.: A 3-D Chimera Grid Embedding Technique. AIAA Paper 85-1523, July 1985.
30. Steger, J. L.; and Benek, J. A.: On the Use of Composite Grid Schemes in Computational Aerodynamics. *Computational Methods in Applied Mechanics and Engineering*, vol. 64, Oct. 1987, pp. 301–320.
31. Buning, P. G.; Chiu, J. T.; Obayashi, S.; Rizk, Y. M.; and Steger, J. L.: Numerical Simulations of the Integrated Space Shuttle Vehicle in Ascent. AIAA Paper 88-4359, Aug. 1988.
32. Luh, R. C.: Surface Grid Generation for Complex Three-Dimensional Geometries. NASA TM-100009, Feb. 1988.

33. Steger, J. L.; and Rizk, Y. M.: Generation of Three-Dimensional Body-Fitted Coordinates Using Hyperbolic Partial Differential Equations. NASA TM-86753, 1985.
34. Chan, W. M.; and Steger, J. L.: A Generalized Scheme for Three-Dimensional Hyperbolic Grid Generation. AIAA Paper 91-1588, June 1991.
35. Benek, J. A.; Steger, J. L.; Dougherty, F. C.; and Buning, P. G.: Chimera: A Grid Embedding Technique. AEDC-TR-85-64, Arnold Air Force Station, Tenn., 1986.
36. Anderson, J. D.: Fundamentals of Aerodynamics. McGraw Hill Inc., 1991.
37. Levy, Y.; Degani, D.; and Seginer, A.: Graphical Visualization of Vortical Flows by Means of Helicity. AIAA J., vol. 28, no. 8, 1990, pp. 1347–1352.
38. Kramer, B. R.; Suárez, C. J.; Malcolm, G. N.; and James, K. D.: Forebody Vortex Control with Jet and Slot Blowing on an F/A-18. AIAA Paper 93-3449, Aug. 1993.
39. Wurtzler, K.: Numerical Analysis of a Chined Forebody with Asymmetric Slot Blowing. AIAA Paper 94-0171, Jan. 1994.
40. Boalbey, R. E.; Ely, W. L.; and Robinson, B. A.: A Sensitivity Study for Pneumatic Vortex Control on a Chined Forebody. AIAA Paper 93-0049, Jan. 1993.
41. Mansy, H. A.: Experimental and Numerical Analysis of the Novel Trapped-Vortex Pair and Coanda Type Fluidic Oscillations for Flow Rate Measurement. Doctor of Philosophy Thesis, Illinois Institute of Technology, 1990.
42. Pulliam, T. H.; Jespersen, D. C.; and Barth, T. J.: Navier–Stokes Computations for Circulation Controlled Airfoils. AIAA Paper 85-1587, July 1985.
43. Anderson, J. D.: Modern Compressible Flow. McGraw Hill, Inc., 1990.
44. Gee, K.; Tavella, D.; and Schiff, L. B.: Computational Investigation of a Pneumatic Forebody Flow Control Concept. J. Aircraft, vol. 30, no. 3, 1993, pp. 326–333.
45. Degani, D.; and Schiff, L. B.: Numerical Simulation of the Effect of Spatial Disturbances on Vortex Asymmetry. AIAA J., vol. 29, no. 3, 1991, pp. 344–352.

Table 5.1. List of numerical solutions and jet exit conditions; $M_\infty = 0.2$, $Re_d = 2.81 \times 10^5$

Surface	Slot	α	MFR ($\times 1000$)	\dot{m} ($\times 1000$ lbm/s)	c_μ	M_{jet}	P_{tot} (lb/in. ²)	T_{tot} (°R)	P_e/P_a
Top	Slot 1	30 deg	0	0	0	–	–	–	–
			0.232	0.417	0.042	0.57	5.05	545	0.94
			0.681	1.220	0.221	1.00	13.05	636	1.59
			1.490	2.670	0.483	1.00	28.51	636	3.47
		40 deg	0.000	0.000	0.000	–	–	–	–
			0.095	0.174	0.007	0.24	4.36	542	0.94
			0.232	0.417	0.042	0.57	5.05	639	0.94
			0.396	0.722	0.126	0.98	7.74	636	0.94
			0.681	1.220	0.221	1.00	13.05	636	1.59
			1.490	2.670	0.483	1.00	28.51	636	3.47
			2.360	4.310	0.761	1.00	46.03	636	5.47
			2.640	4.810	0.851	1.00	51.48	636	6.19
			3.270	5.950	1.053	1.00	63.66	636	7.56
			3.720	6.770	1.198	1.00	72.45	636	8.61
			4.170	7.600	1.344	1.00	81.25	636	9.66
	Slot 2	40 deg	0	0	0	–	–	–	–
			0.095	0.174	0.007	0.24	4.36	542	0.94
			0.232	0.417	0.042	0.57	5.05	639	0.94
			0.396	0.722	0.126	0.98	7.74	636	0.94
			0.681	1.220	0.221	1.00	13.05	636	1.59
			1.490	2.670	0.483	1.00	28.51	636	3.47
			2.360	4.310	0.761	1.00	46.03	636	5.47
Bottom	Slot 1	30 deg	0	0	0	–	–	–	–
			0.232	0.417	0.042	0.57	5.05	639	0.94
			0.396	0.722	0.126	0.98	7.74	636	0.94
			0.681	1.220	0.221	1.00	13.05	636	1.59
			1.040	1.900	0.337	1.00	20.34	636	2.42
			1.490	2.670	0.483	1.00	28.51	636	3.47
		40 deg	0	0	0	–	–	–	–
			0.232	0.417	0.042	0.57	5.05	545	0.94
			0.681	1.220	0.221	1.00	13.05	636	1.59
			1.490	2.670	0.483	1.00	28.51	636	3.47
			2.360	4.310	0.761	1.00	46.03	636	5.47

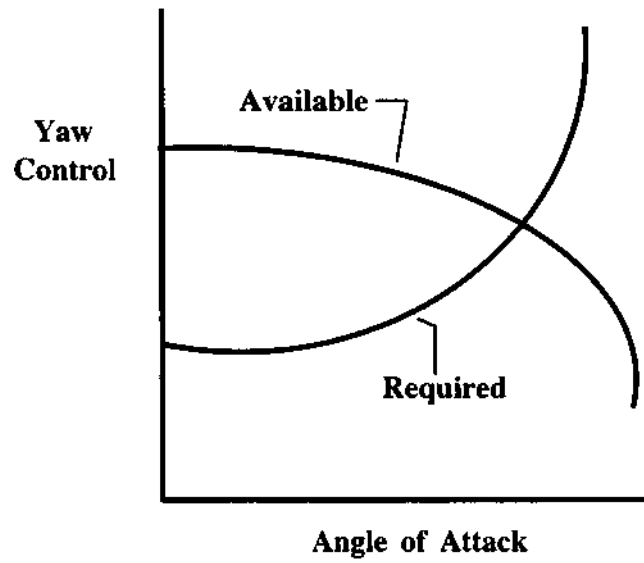


Figure 1.1. Yaw control power.

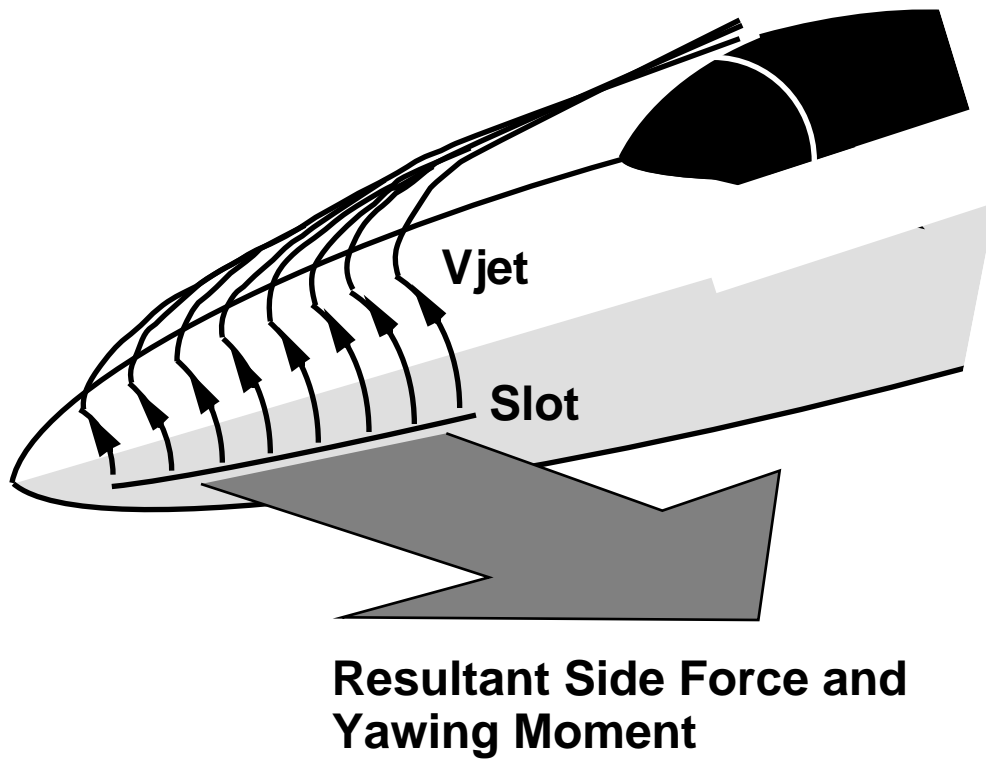
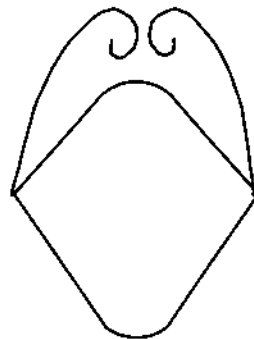
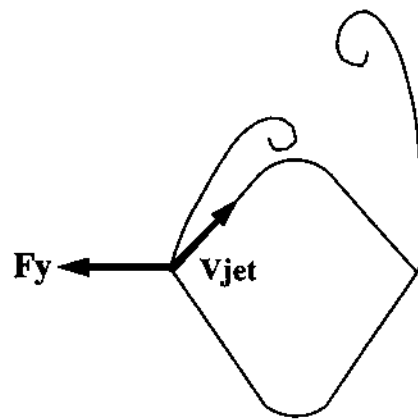


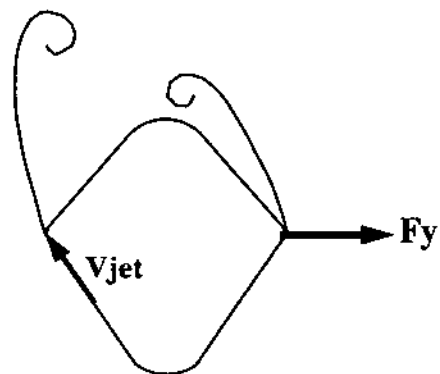
Figure 1.2. Forebody tangential slot blowing concept.



(a) No-blowing



(b) Blowing from the top surface



(c) Blowing from the bottom surface

Figure 1.3. Effects of tangential slot blowing on a chined forebody.

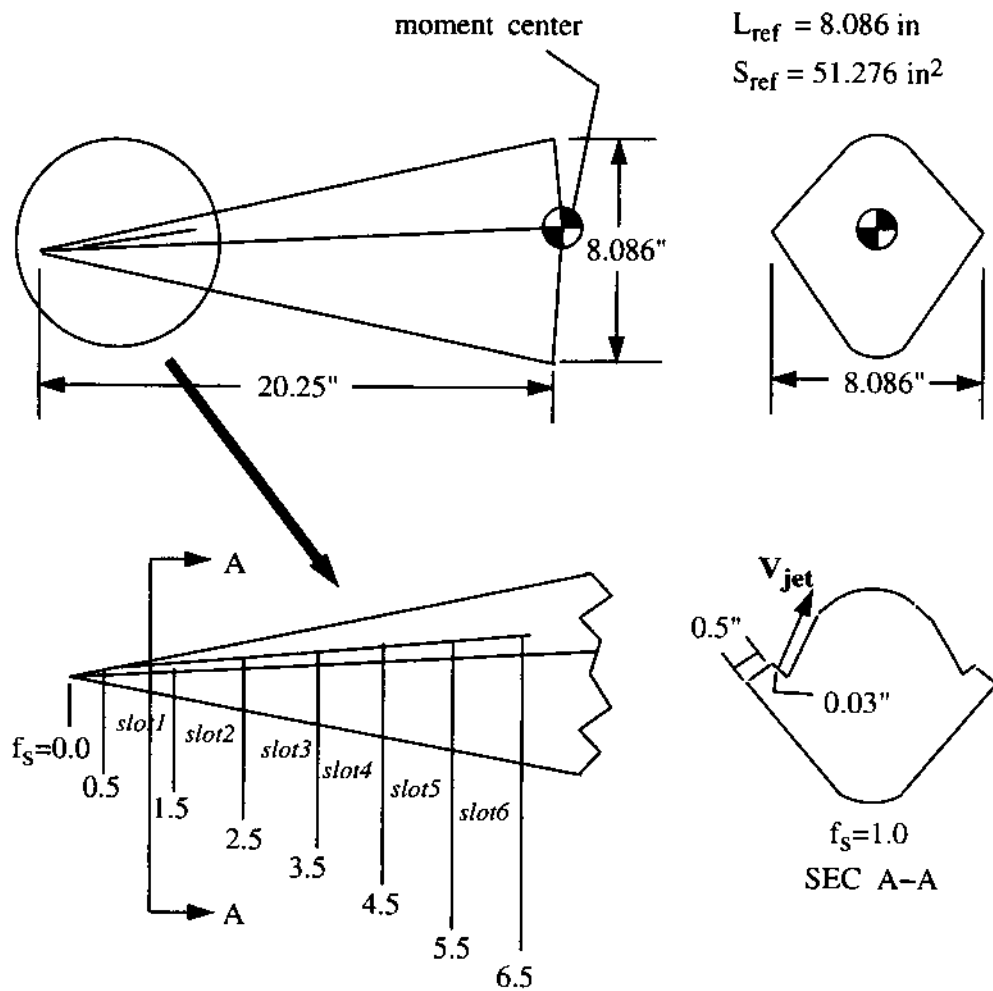


Figure 1.4. Dimensions of the generic chined forebody wind tunnel model.

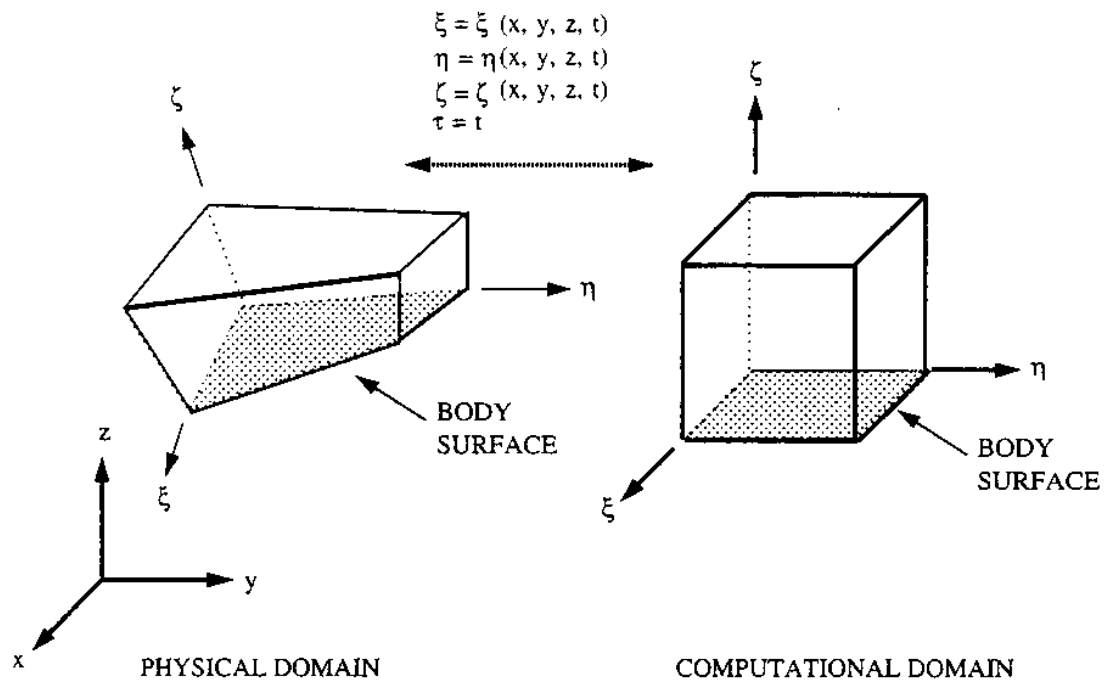


Figure 2.1. Generalized transformation from the physical domain to the computational domain.

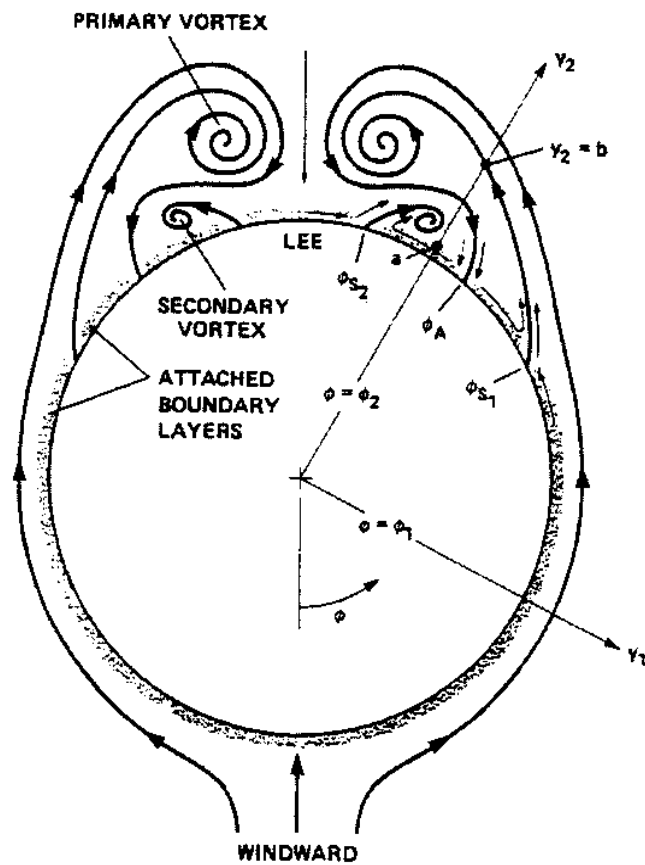
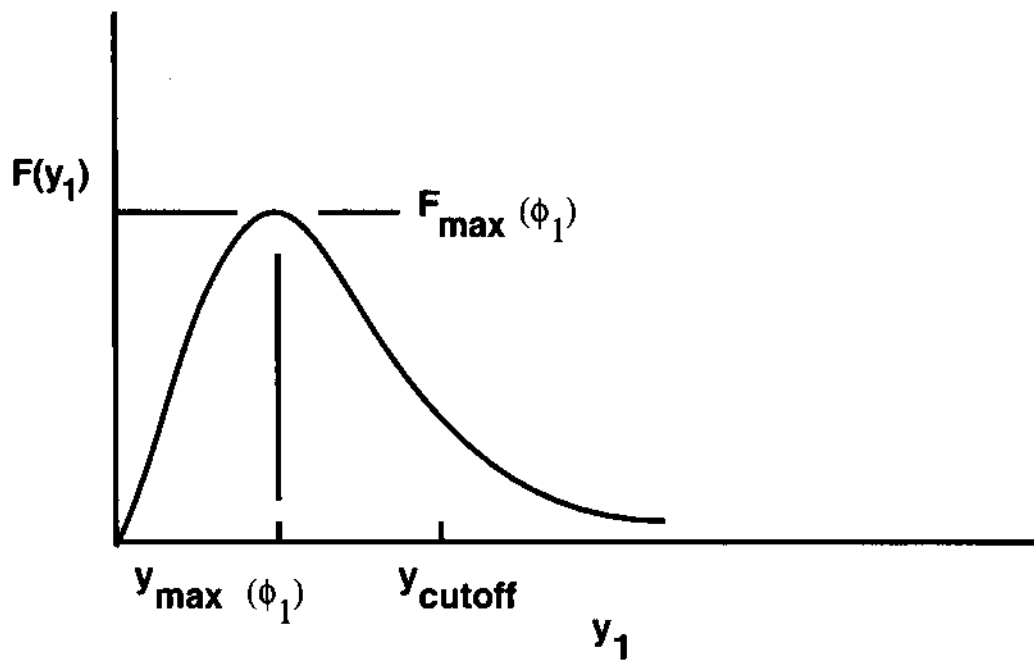
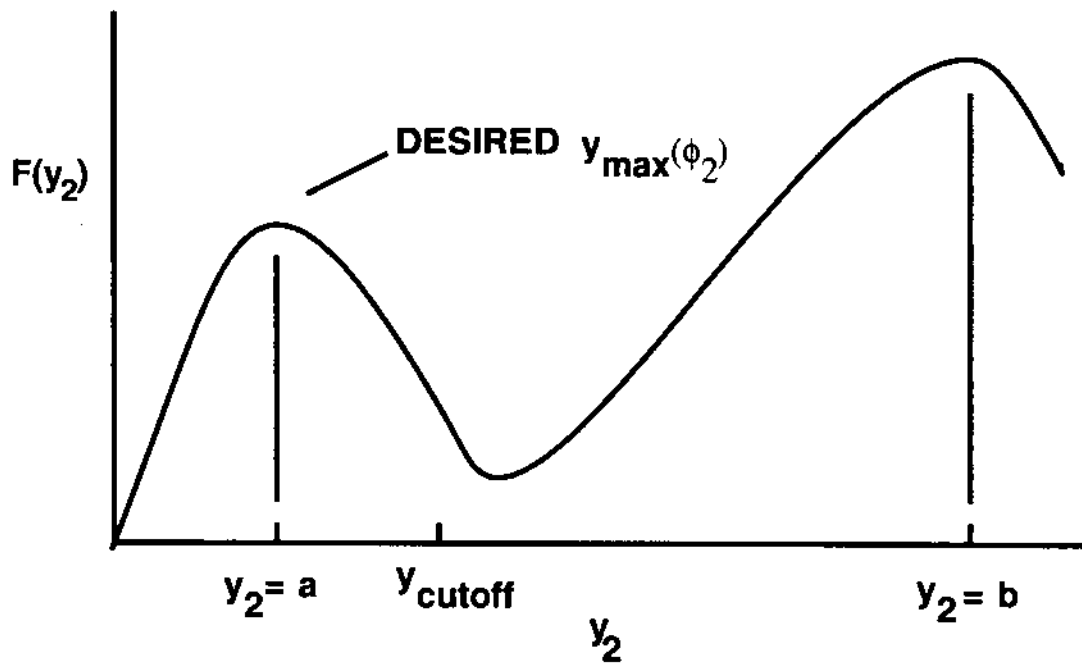


Figure 2.2. Flow structure in the cross-flow plane.

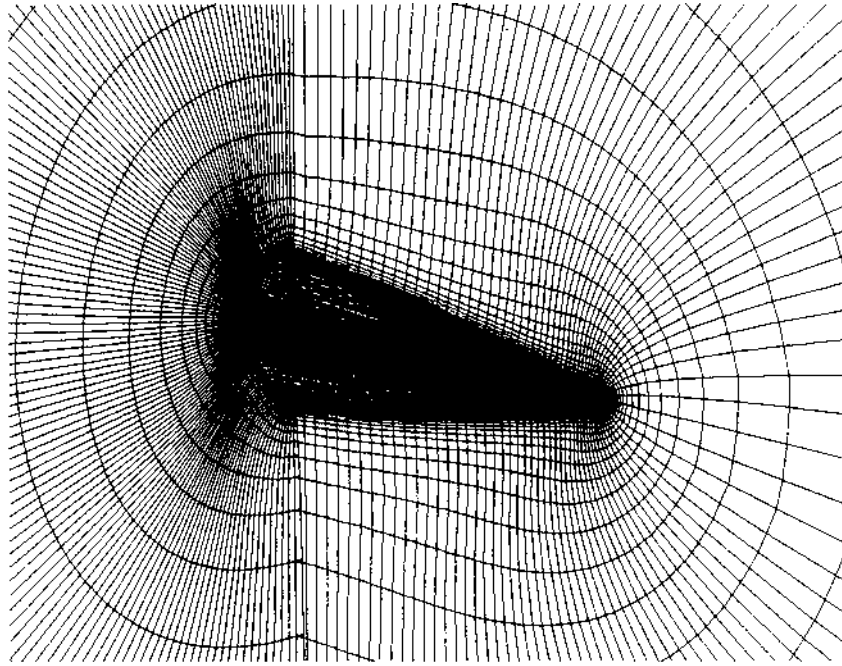


(a) Windward side ($\phi = \phi_1$)

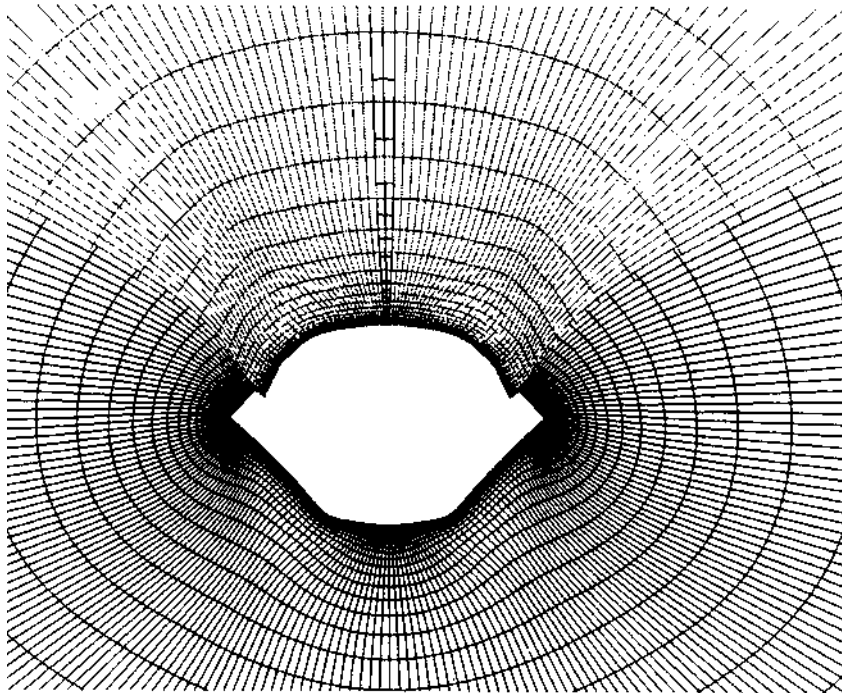


(b) Leeward side ($\phi = \phi_2$)

Figure 2.3. The behavior of $F(y)$ at large incidence.



(a) Portion of computational grid



(b) $f_s \approx 1.0$

Figure 4.1. Portion of grid modeling generic chined forebody (every other point shown for clarity).

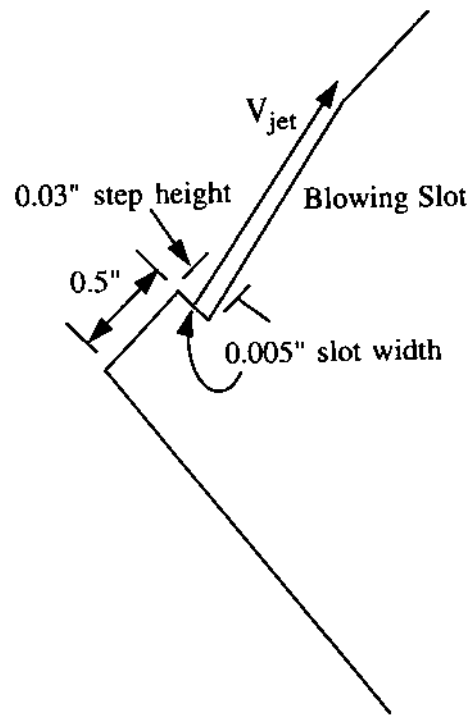


Figure 4.2. Cross-sectional view of blowing slot showing the backward facing step.

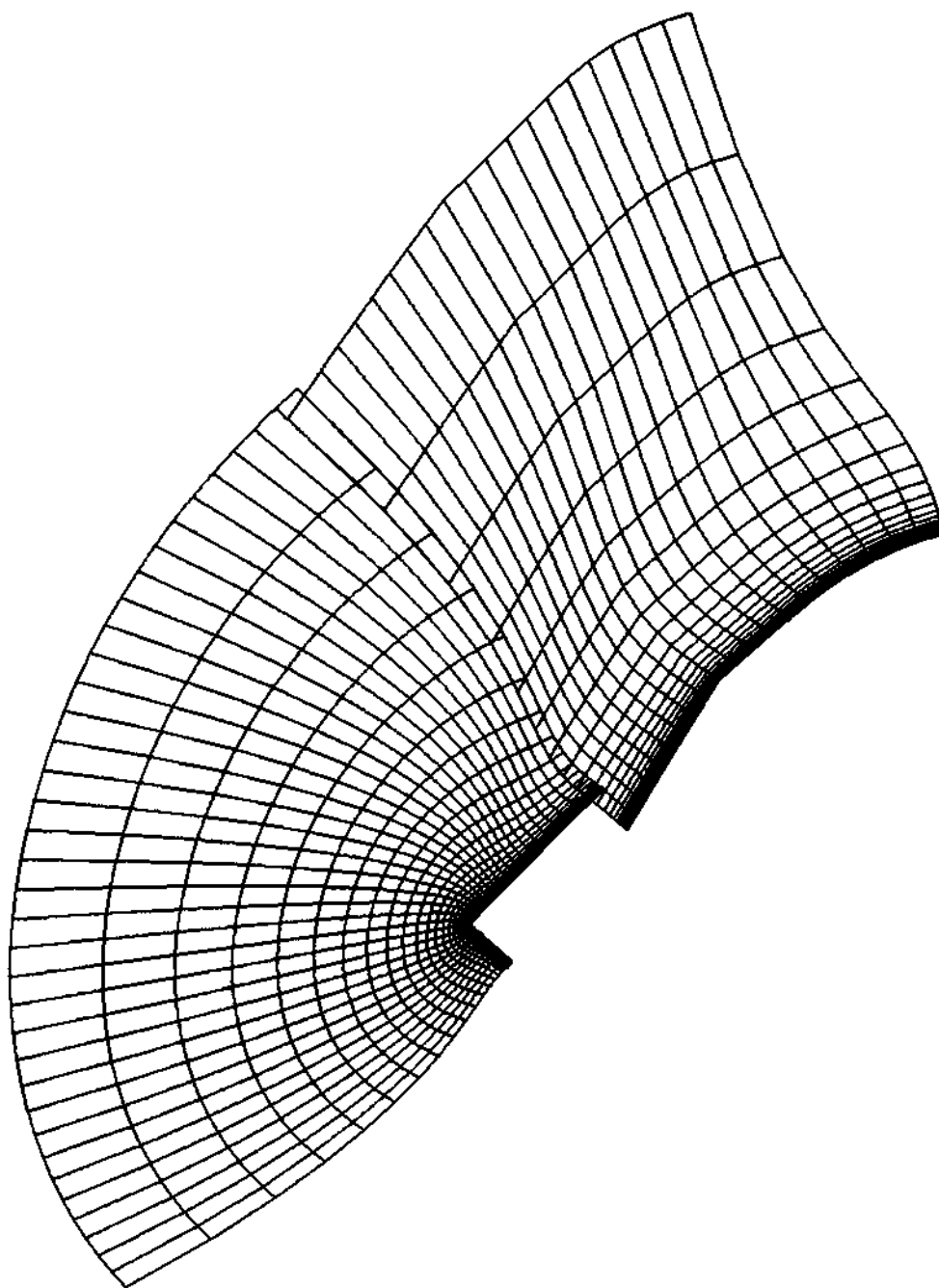
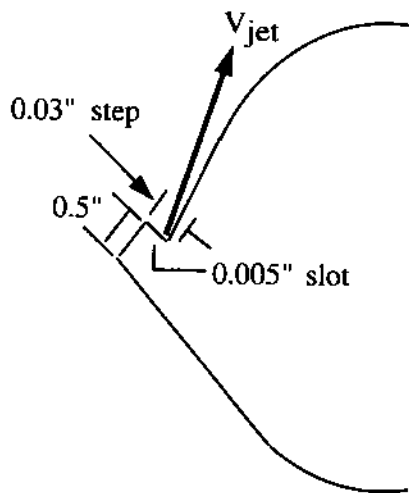
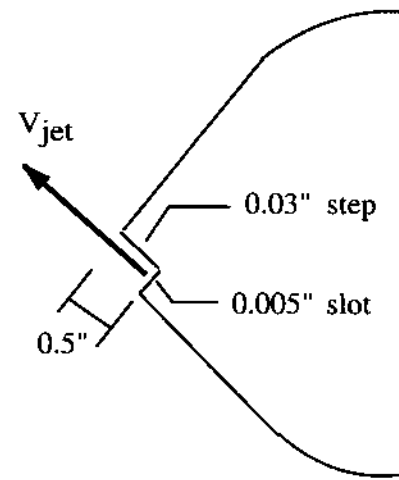


Figure 4.3. Cross section of forebody and slot grid overlap.



(a) Top slot blowing



(b) Bottom slot blowing

Figure 4.4. Slot configurations for top and bottom slot blowing.

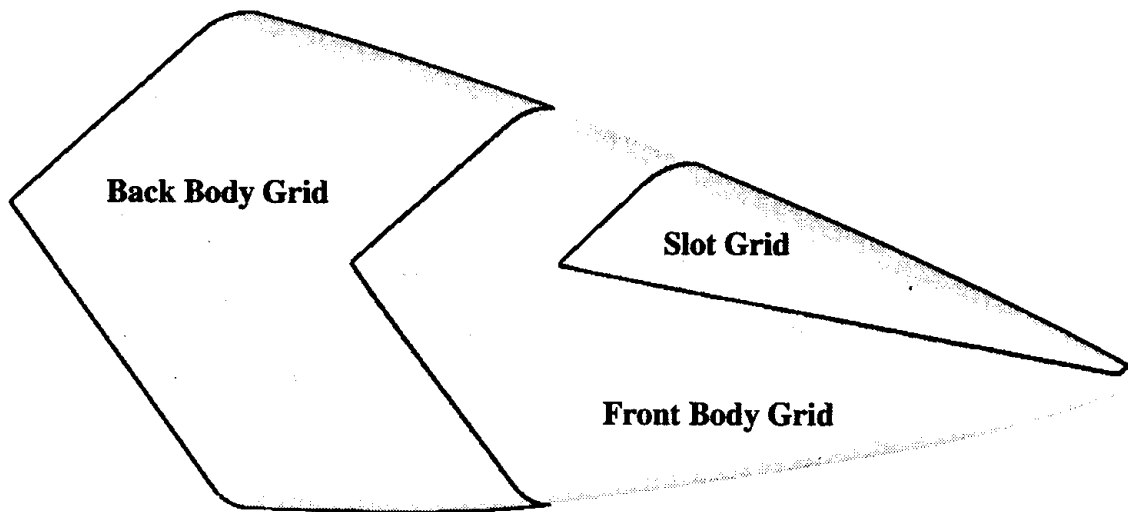
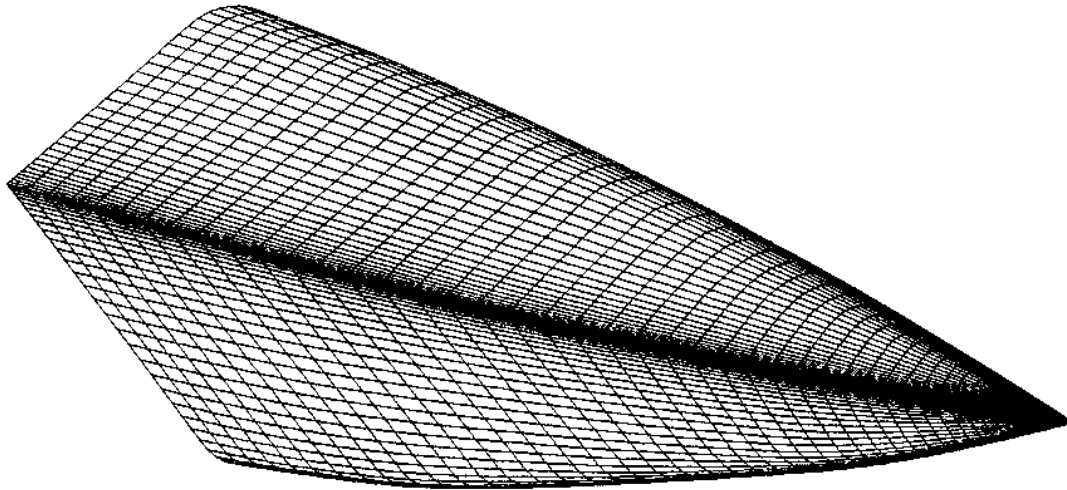
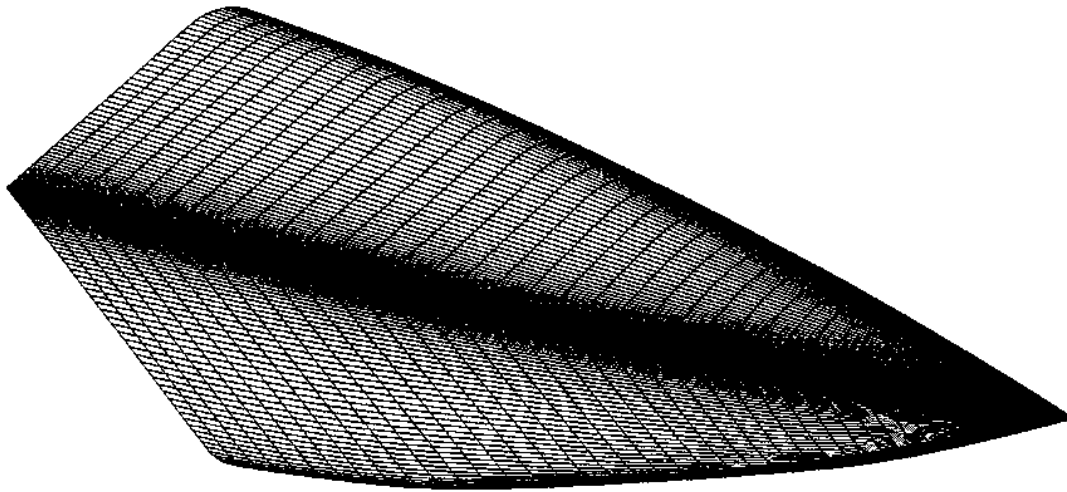


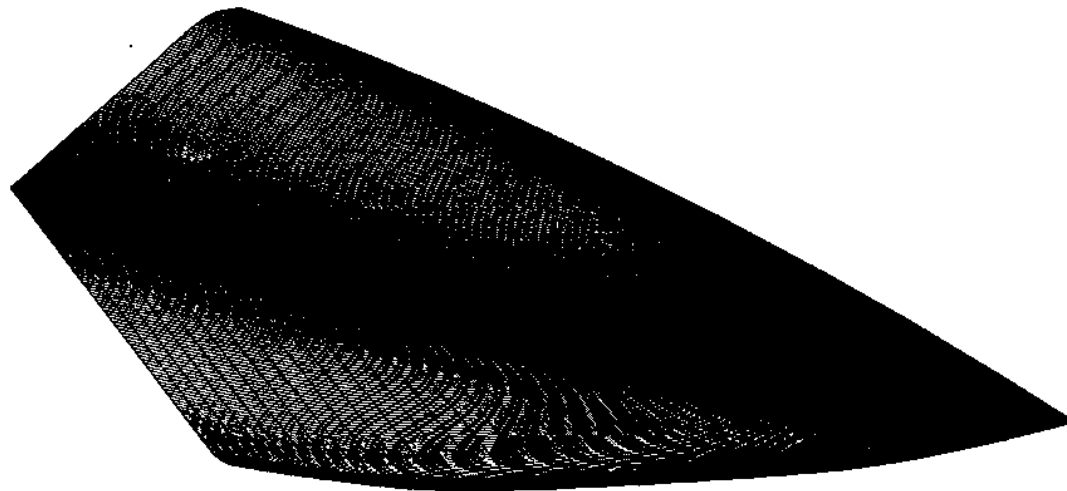
Figure 4.5. Grid boundaries on the starboard side of the forebody.



(a) Coarse density grid, $50 \times 63 \times 50$



(b) Medium density grid, $50 \times 123 \times 50$



(c) Fine density grid, $50 \times 243 \times 50$

Figure 5.1. Surface grid lines of the cases used in the grid sensitivity test.

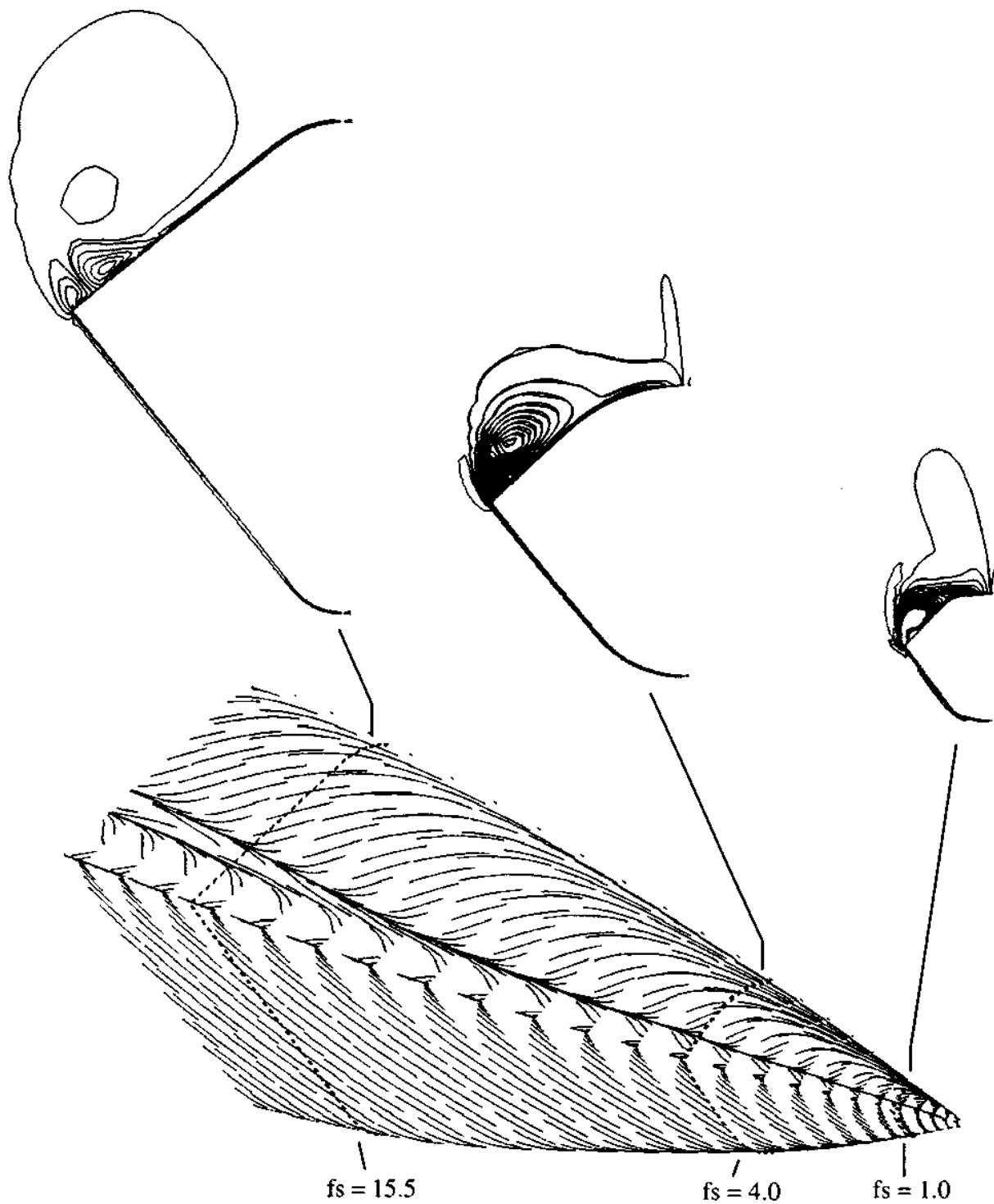


Figure 5.2. Computed surface flow patterns and helicity density contours, coarse density grid, $50 \times 63 \times 50$ points; $M_\infty = 0.2$, $\alpha = 30$ deg, $Re_d = 2.81 \times 10^5$.

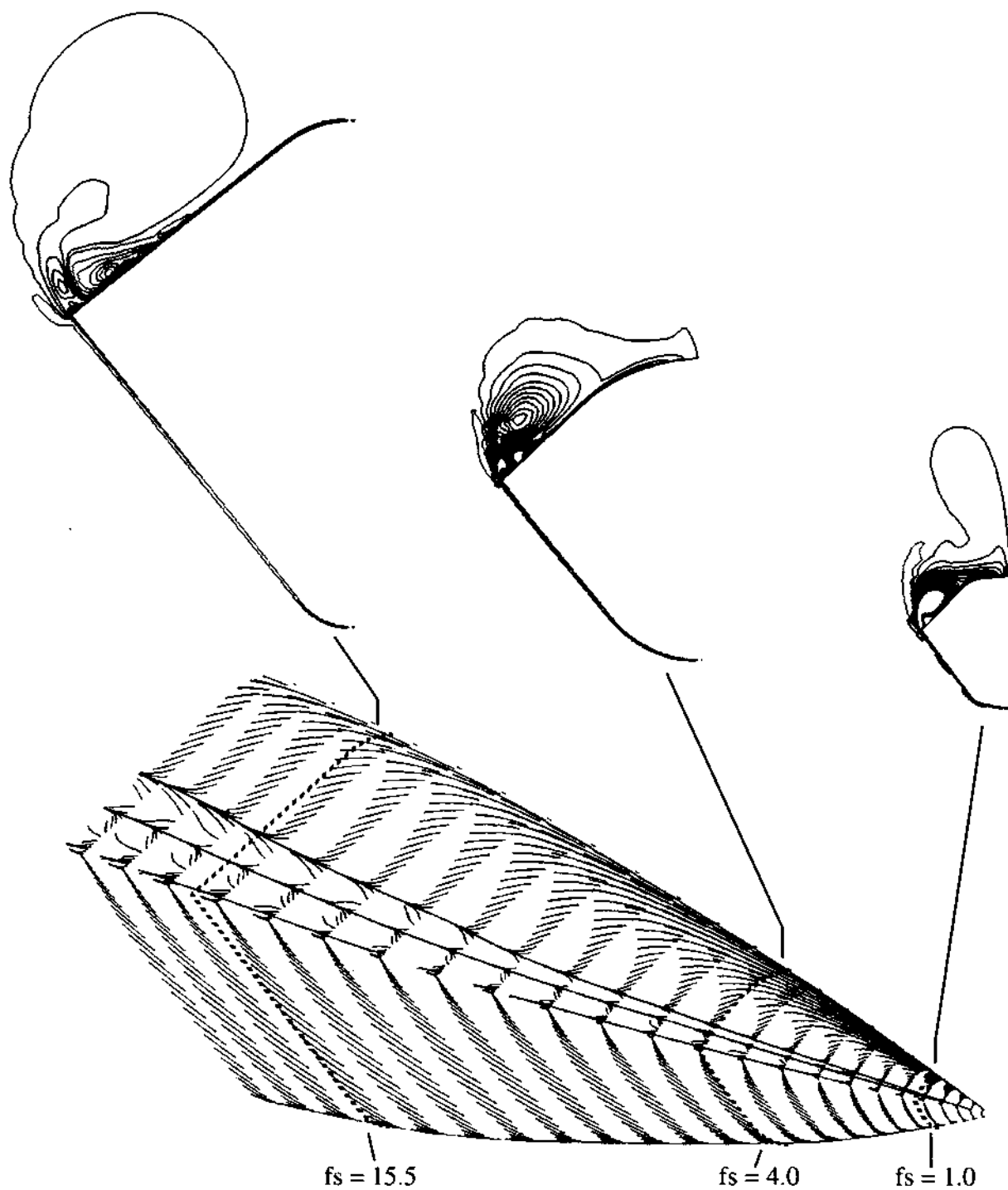


Figure 5.3. Computed surface flow patterns and helicity density contours, medium density grid, $50 \times 123 \times 50$ points; $M_\infty = 0.2$, $\alpha = 30$ deg, $Re_d = 2.81 \times 10^5$.

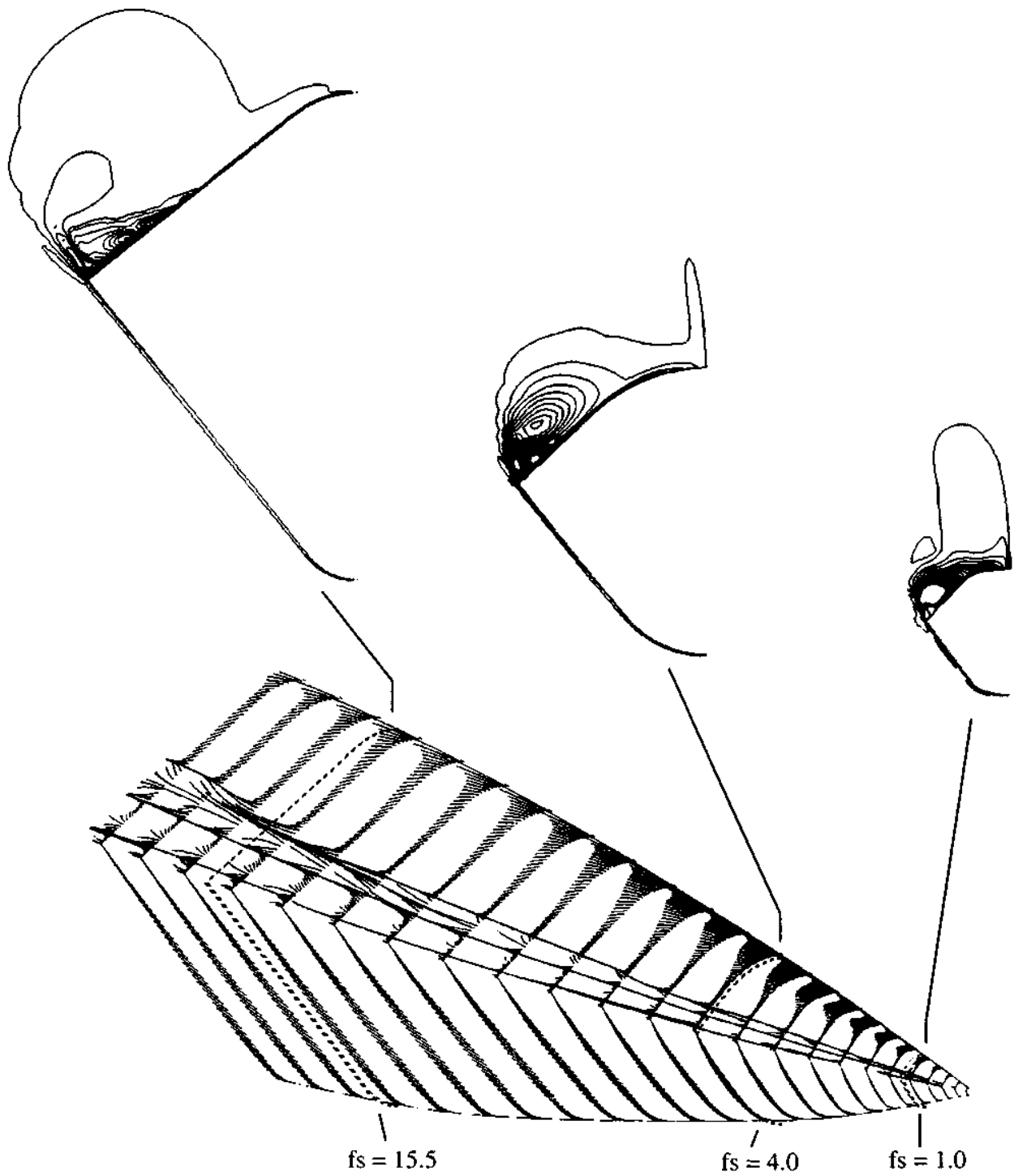


Figure 5.4. Computed surface flow patterns and helicity density contours, fine density grid, $50 \times 243 \times 50$ points; $M_\infty = 0.2$, $\alpha = 30$ deg, $Re_d = 2.81 \times 10^5$.

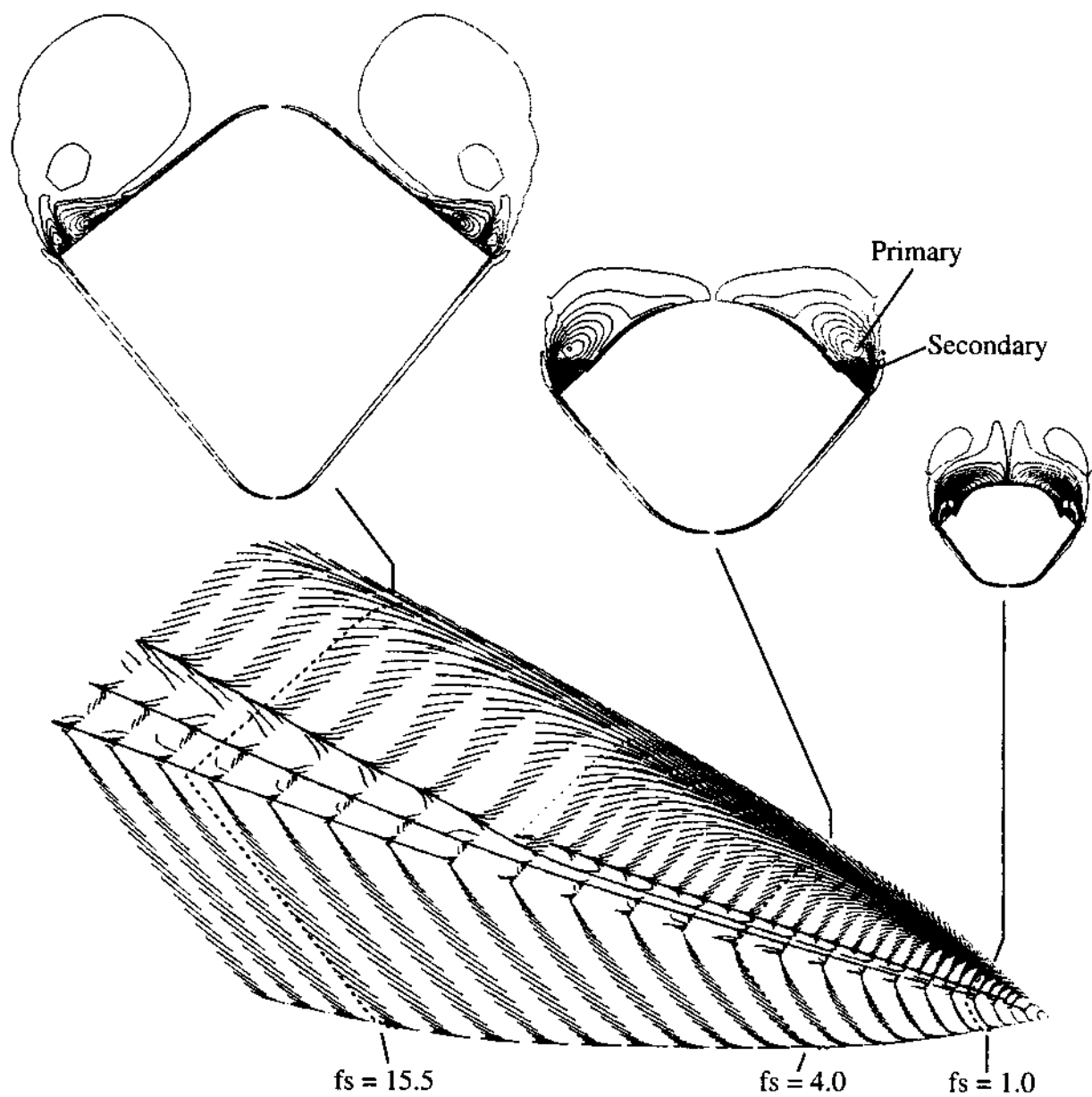


Figure 5.5. Computed surface flow patterns and helicity density contours, no-blowing; $M_\infty = 0.2$, $\alpha = 30$ deg, $Re_d = 2.81 \times 10^5$.

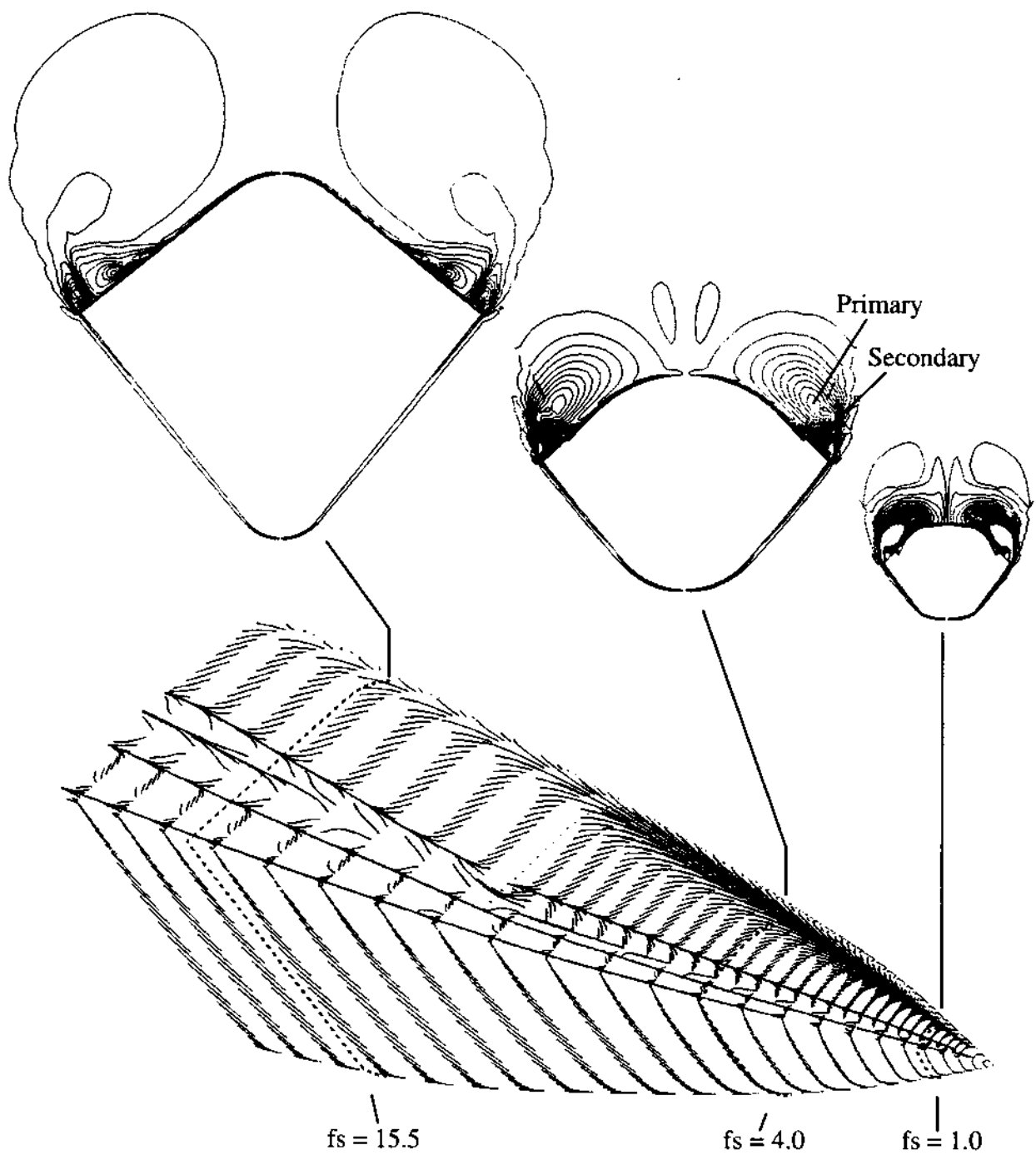


Figure 5.6. Computed surface flow patterns and helicity density contours, no-blowing; $M_\infty = 0.2$, $\alpha = 40$ deg, $Re_d = 2.81 \times 10^5$.

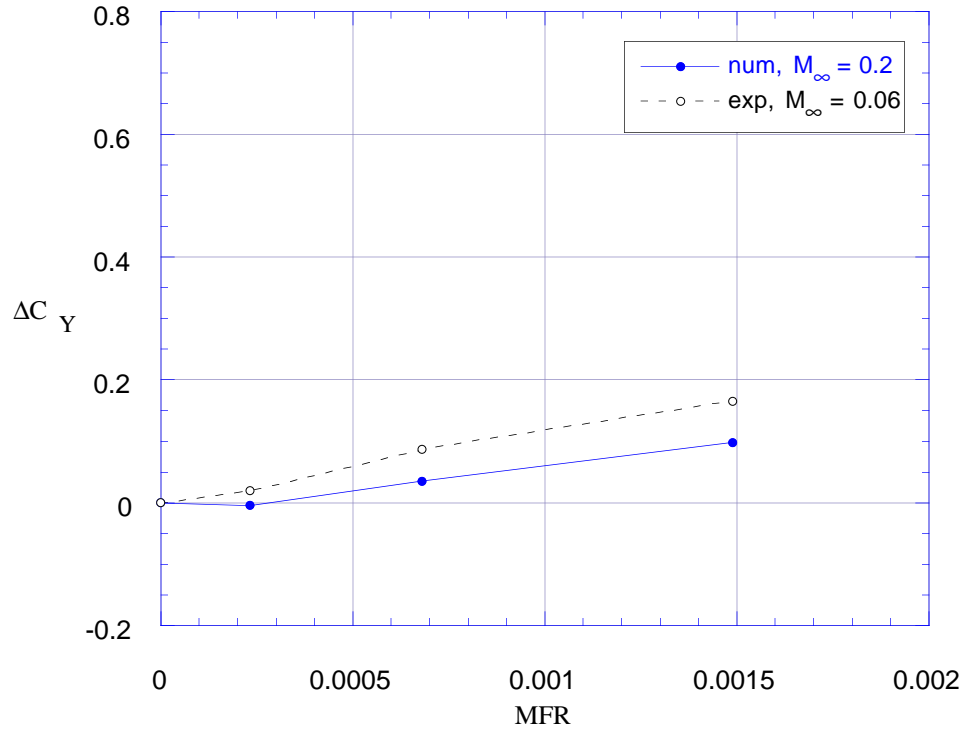


Figure 5.7. Comparison of numerical and experimental incremental side force data for Slot 1; $\alpha = 30$ deg, $Re_d = 2.81 \times 10^5$.

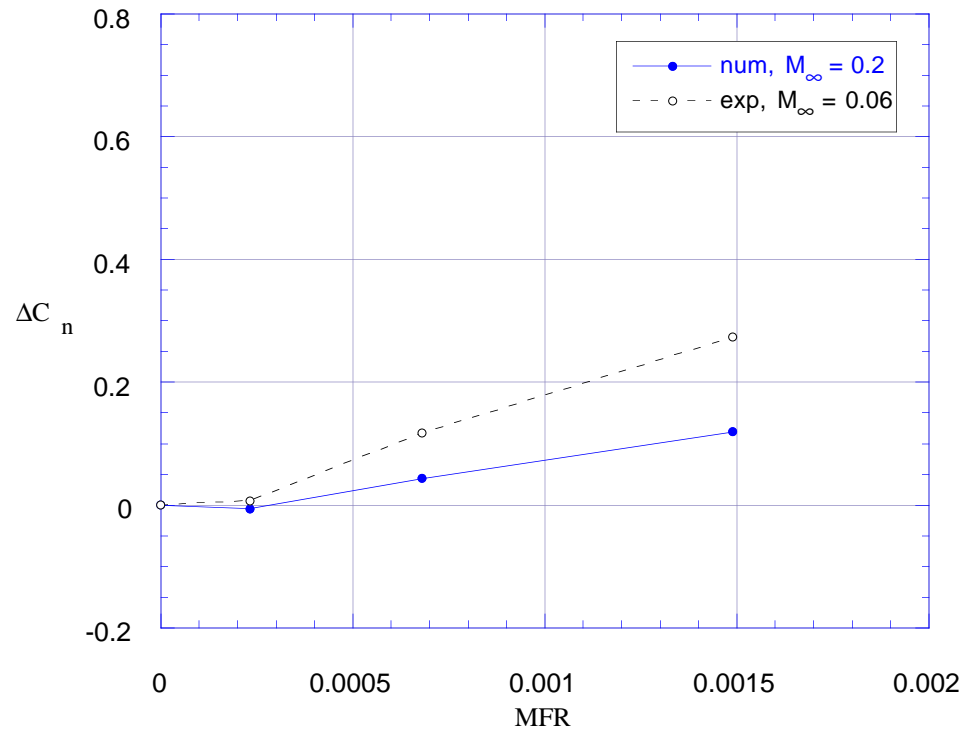


Figure 5.8. Comparison of numerical and experimental incremental yawing moment data for Slot 1; $\alpha = 30$ deg, $Re_d = 2.81 \times 10^5$.

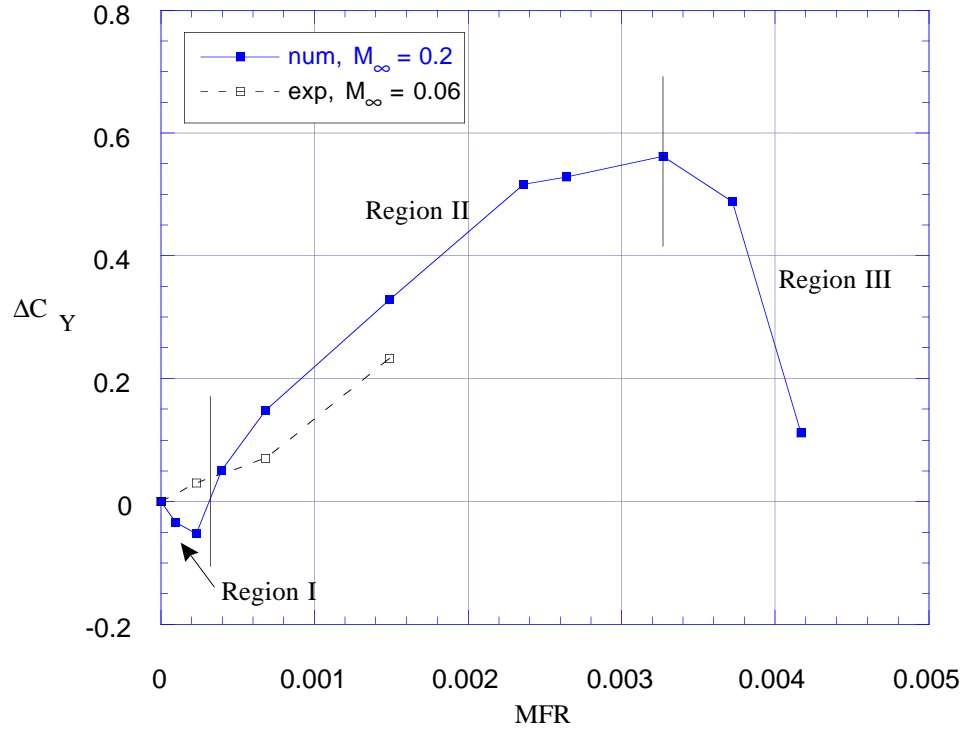


Figure 5.9. Comparison of numerical and experimental incremental side force data for Slot 1; $\alpha = 40$ deg, $Re_d = 2.81 \times 10^5$.

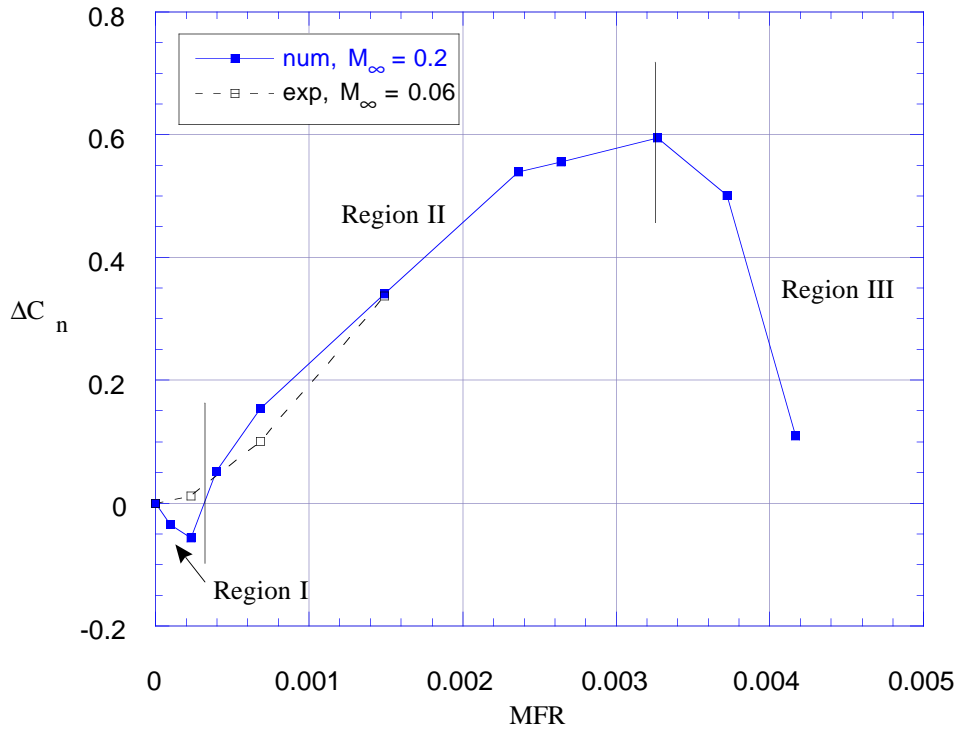


Figure 5.10. Comparison of numerical and experimental incremental yawing moment data for Slot 1; $\alpha = 40$ deg, $Re_d = 2.81 \times 10^5$.

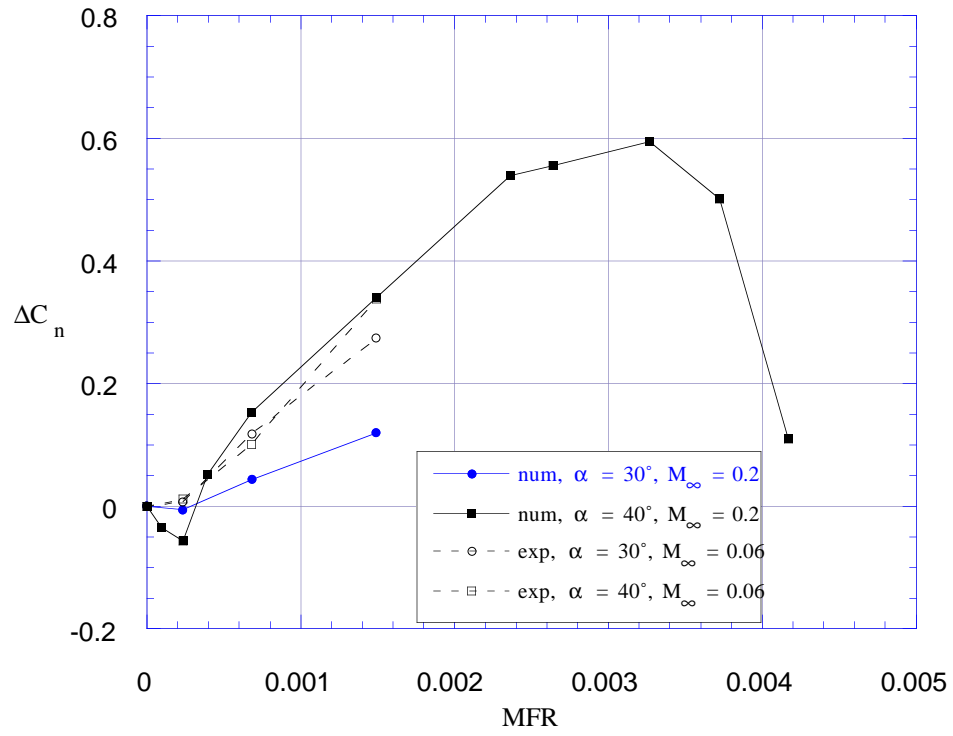
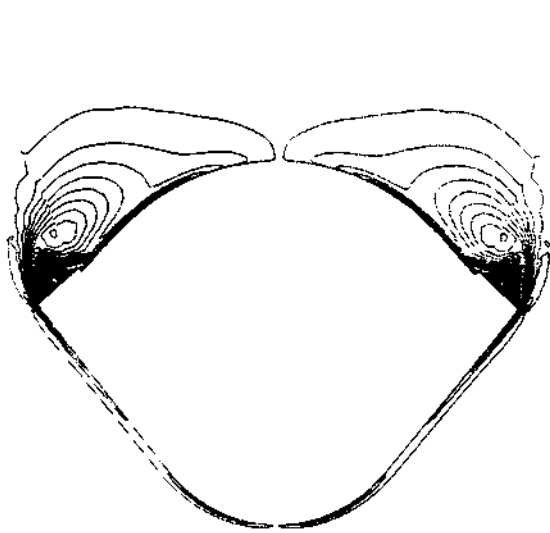
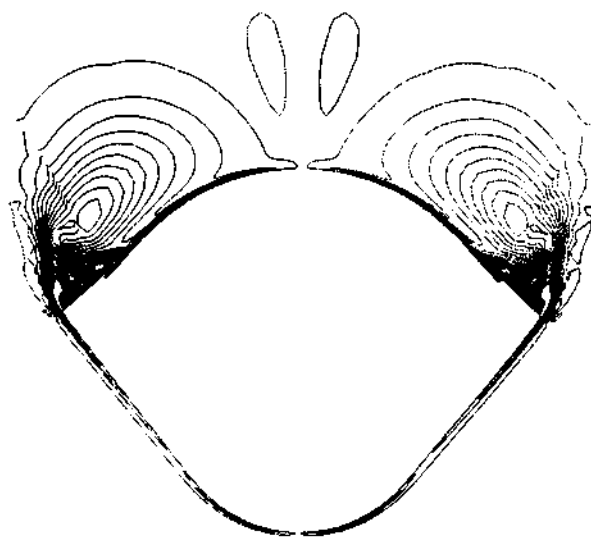


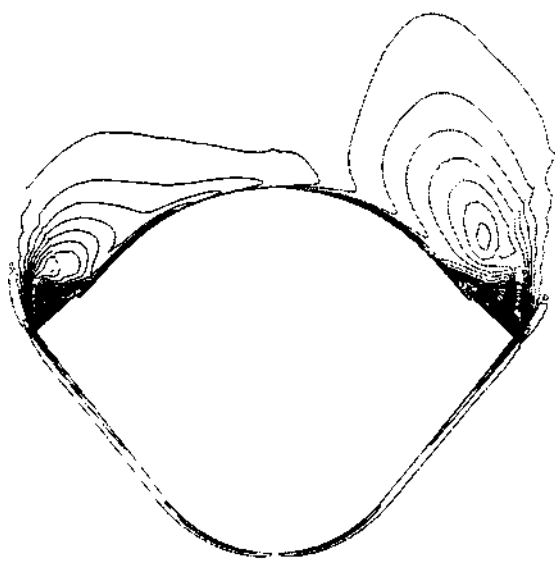
Figure 5.11. Effect of angle of attack on yawing moment produced by slot blowing; $Re_d = 2.81 \times 10^5$.



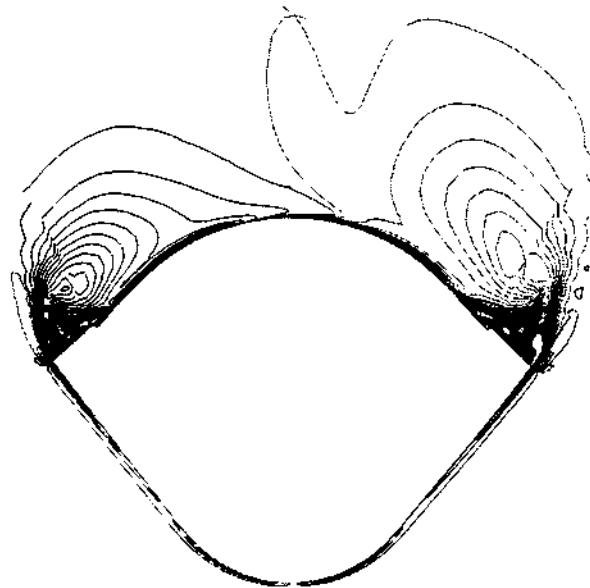
(a) No-blowing, $\alpha = 30$ deg



(b) No-blowing, $\alpha = 40$ deg



(c) $MFR = 1.49 \times 10^{-3}$, $\alpha = 30$ deg



(d) $MFR = 1.49 \times 10^{-3}$, $\alpha = 30$ deg

Figure 5.12. Computed helicity density contours at fuselage station $f_s = 4.0$; $M_\infty = 0.2$, $Re_d = 2.81 \times 10^5$.

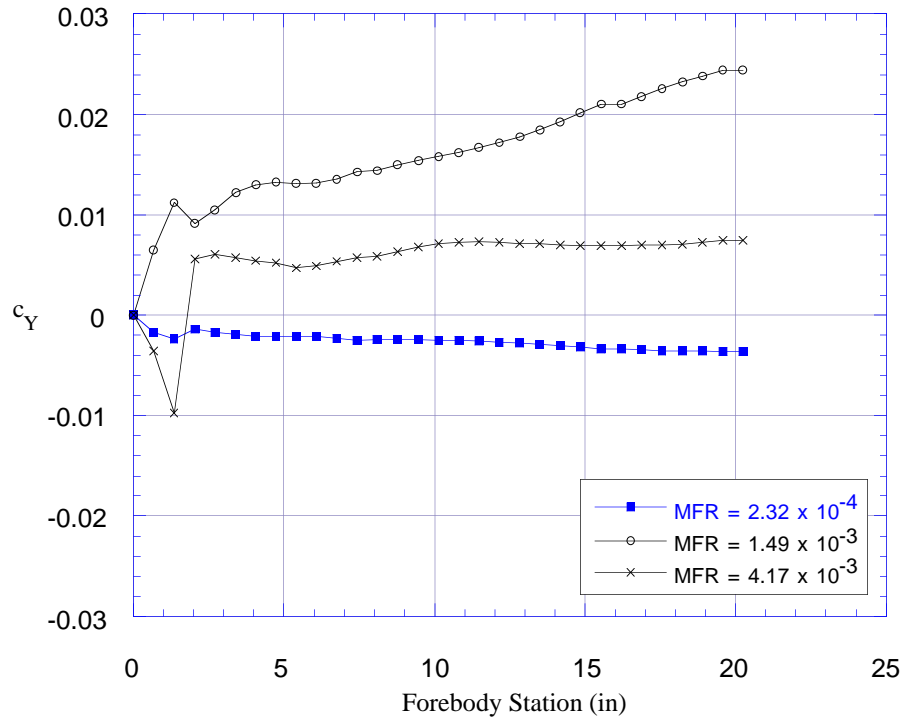


Figure 5.13. Distribution of computed sectional side-force coefficient along the body; $M_\infty = 0.2$, $\alpha = 40$ deg, $Re_d = 2.81 \times 10^5$.

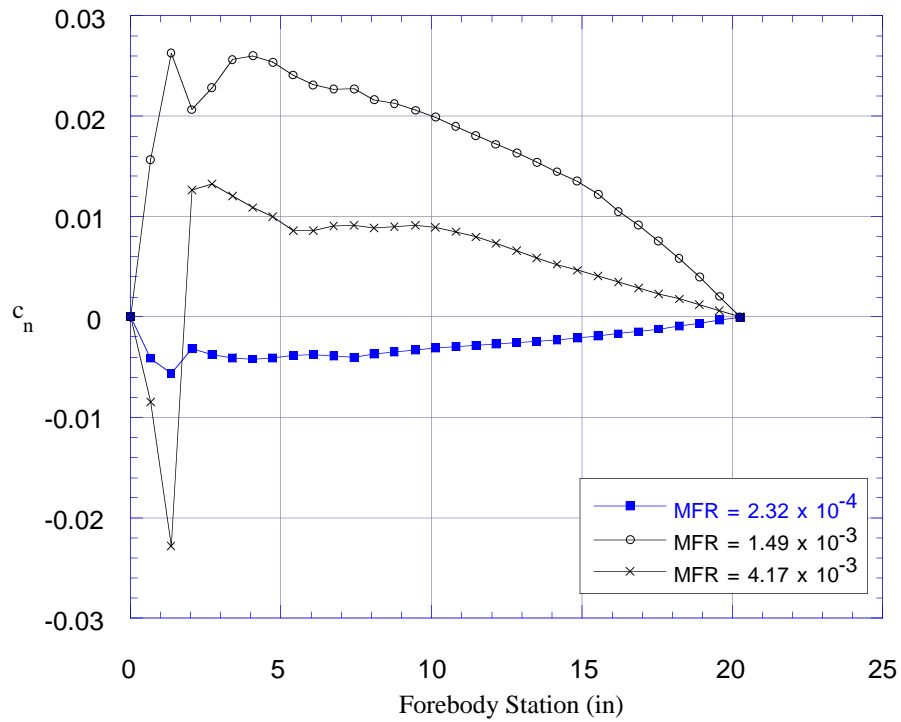


Figure 5.14. Distribution of computed sectional yawing-moment coefficient along the body; $M_\infty = 0.2$, $\alpha = 40$ deg, $Re_d = 2.81 \times 10^5$.

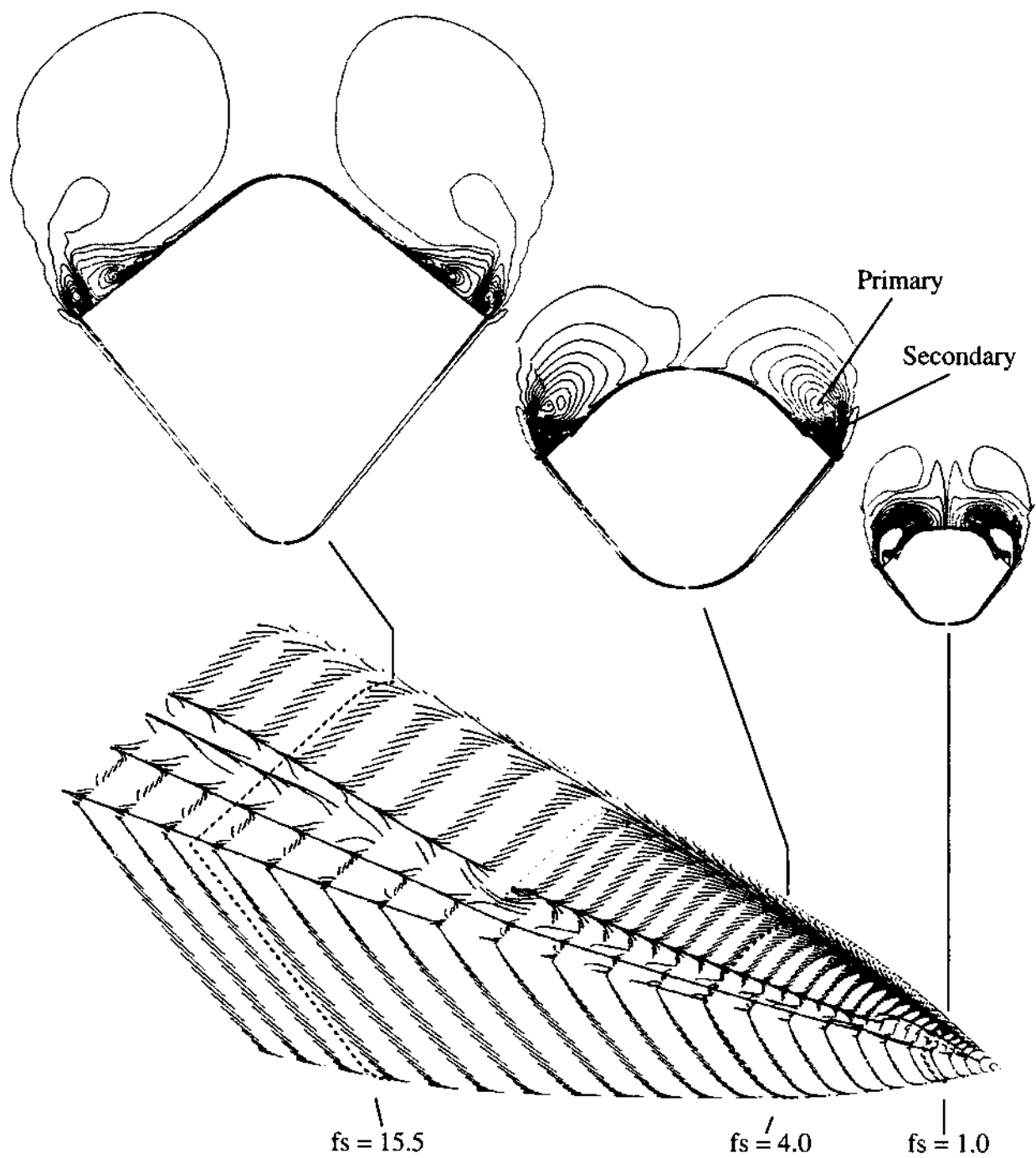


Figure 5.15. Computed surface flow patterns and helicity density contours; $M_\infty = 0.2$, $\alpha = 40$ deg, $Re_d = 2.81 \times 10^5$, $MFR = 0.23 \times 10^{-3}$.

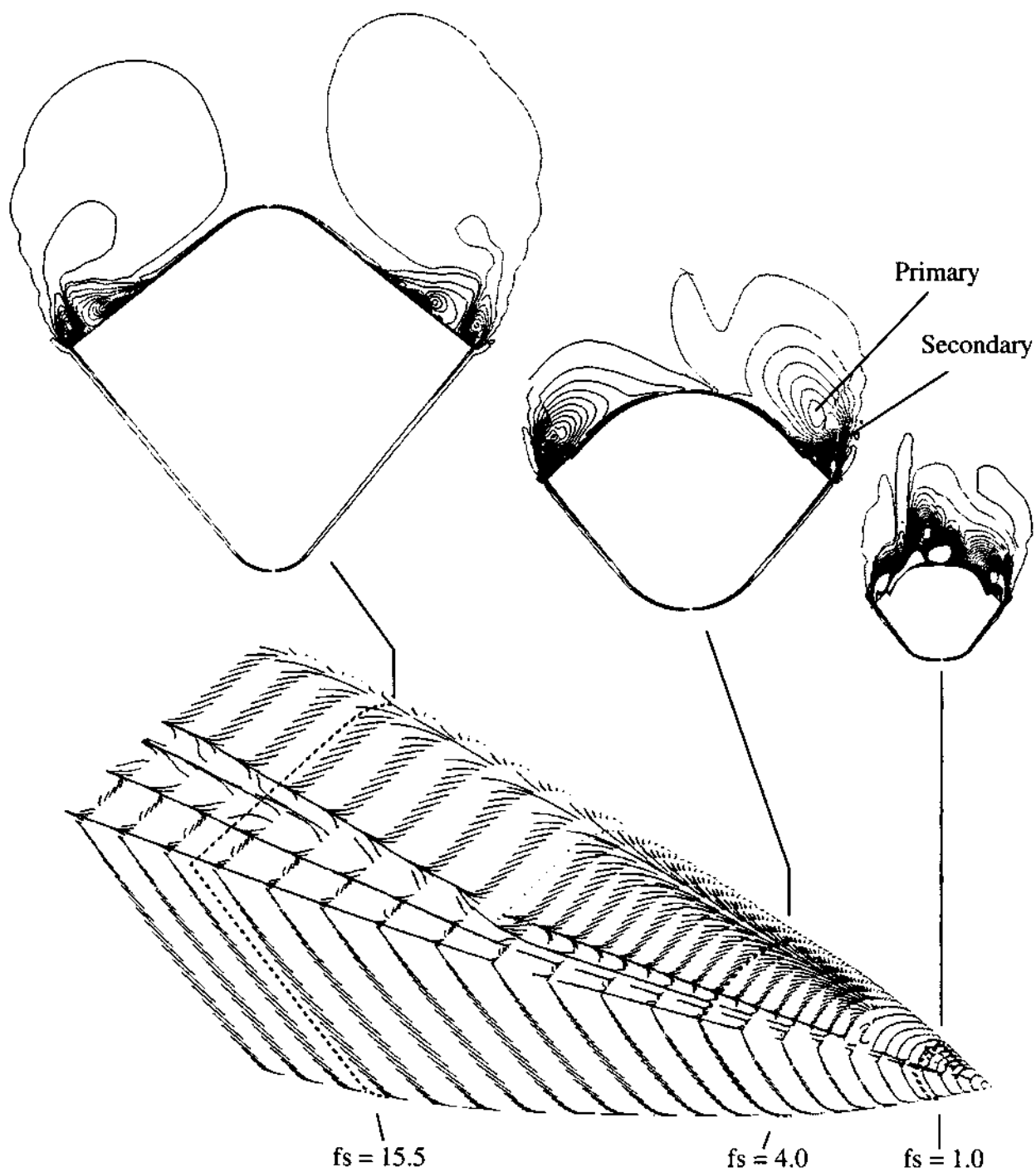


Figure 5.16. Computed surface flow patterns and helicity density contours; $M_\infty = 0.2$, $\alpha = 40$ deg, $Re_d = 2.81 \times 10^5$, $MFR = 1.49 \times 10^{-3}$.

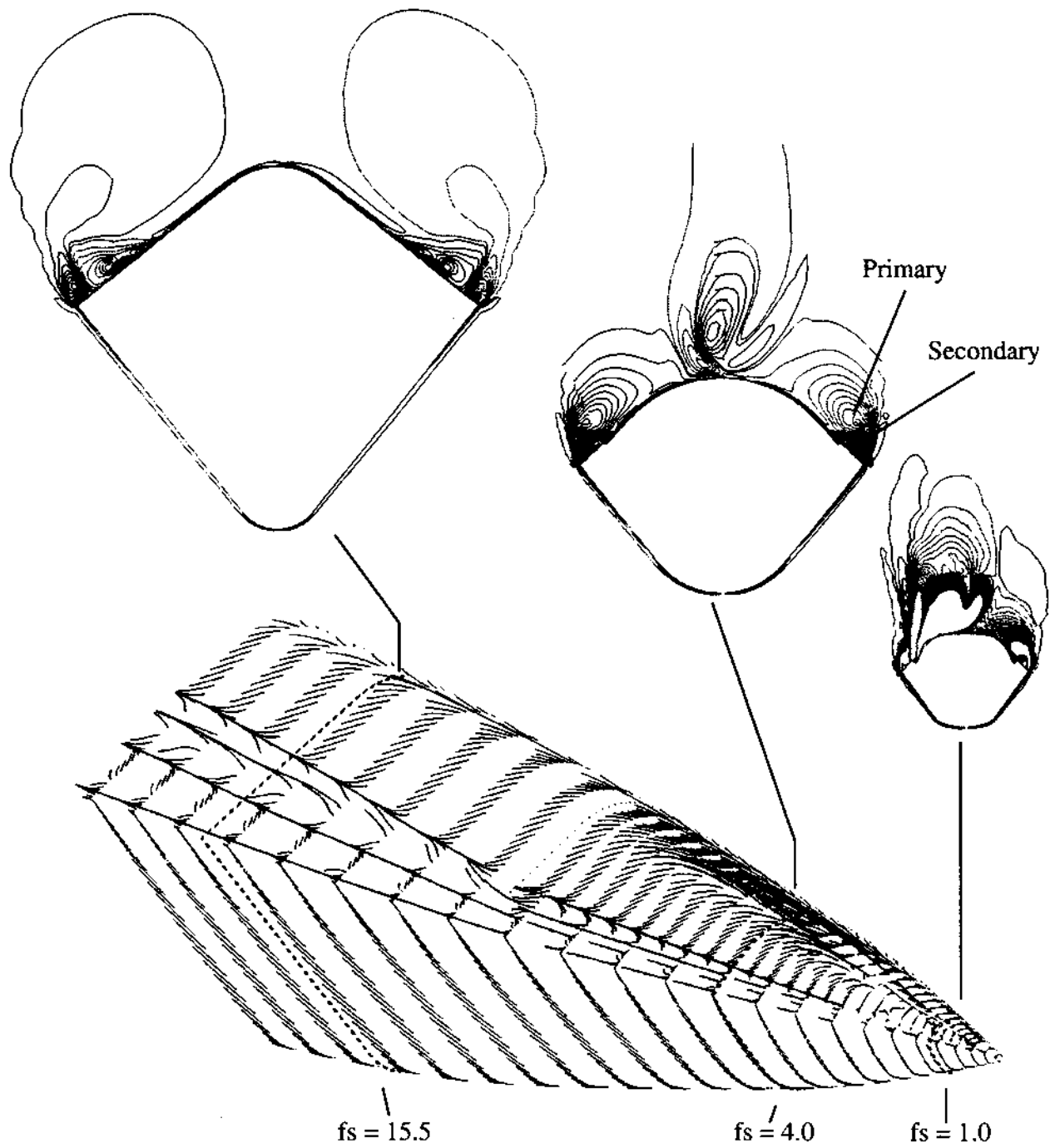
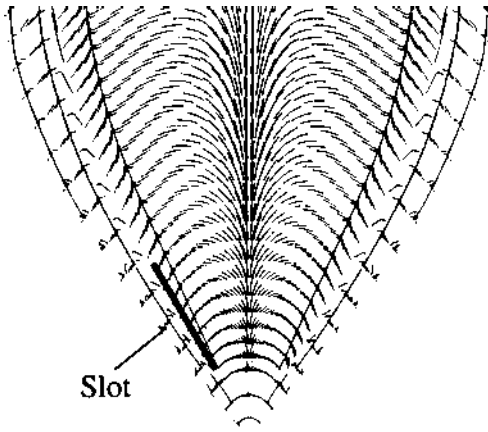
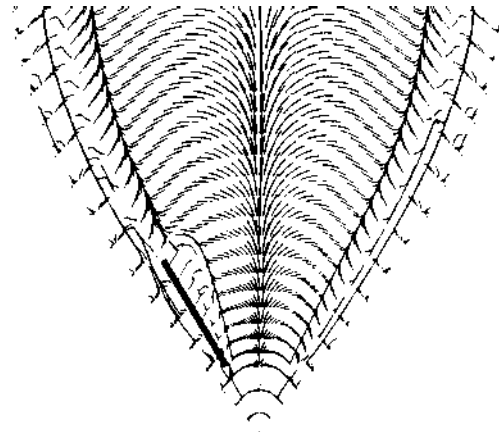


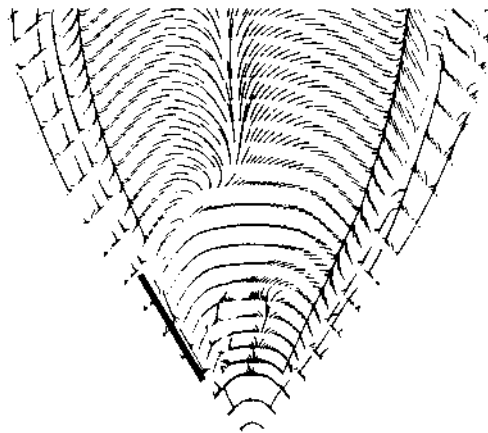
Figure 5.17. Computed surface flow patterns and helicity density contours; $M_\infty = 0.2$, $\alpha = 40^\circ$, $Re_d = 2.81 \times 10^5$, $MFR = 4.17 \times 10^{-3}$.



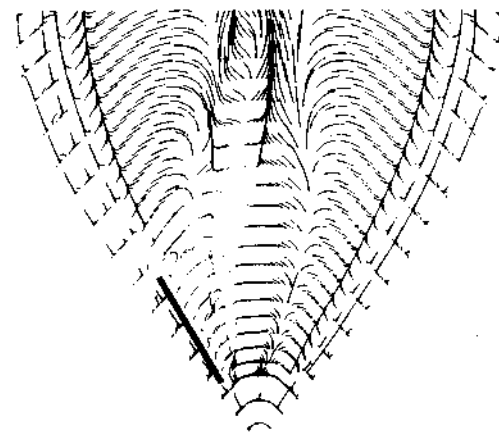
(a) No-blowing



(b) Region I, $MFR = 0.23 \times 10^{-3}$

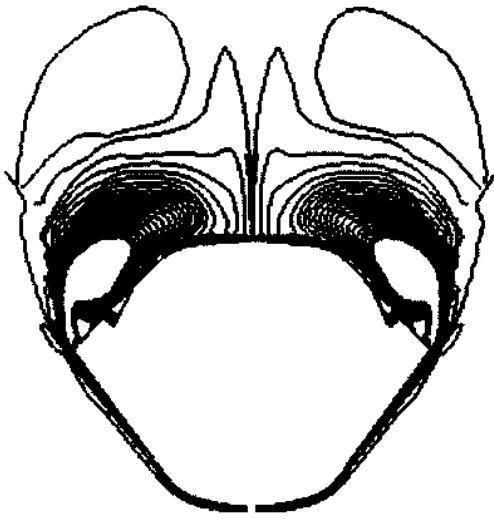


(c) Region II, $MFR = 1.49 \times 10^{-3}$

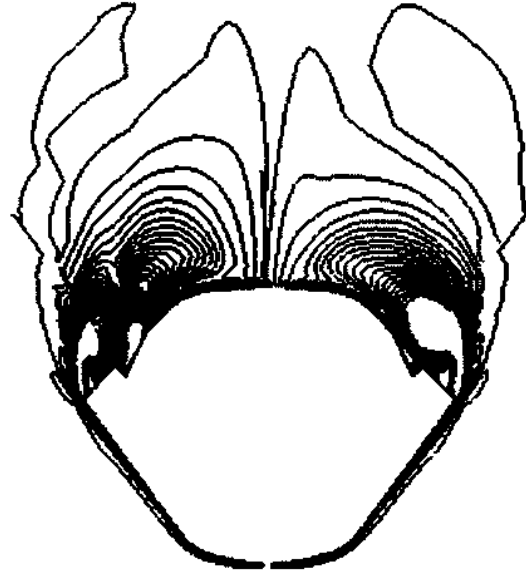


(d) Region III, $MFR = 4.17 \times 10^{-3}$

Figure 5.18. Surface flow patterns, $M_\infty = 0.2$, $\alpha = 40$ deg, $Re_d = 2.81 \times 10^5$.



(a) No-blowing



(b) Region I, $MFR = 0.23 \times 10^{-3}$

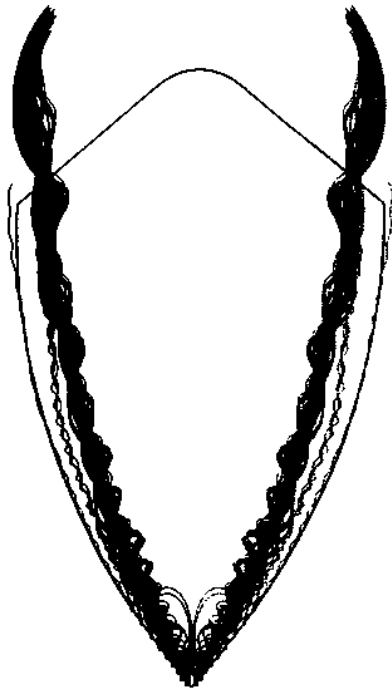


(c) Region II, $MFR = 1.49 \times 10^{-3}$

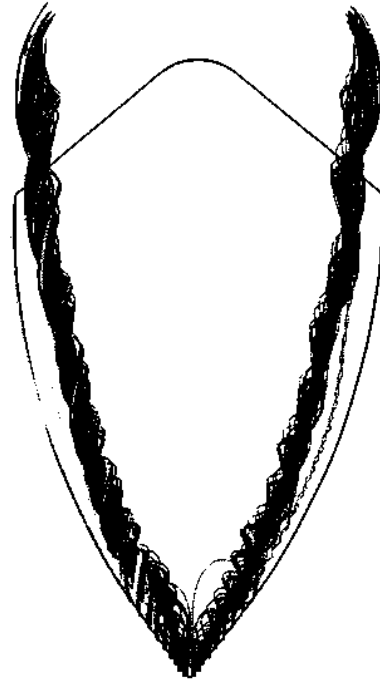


(d) Region III, $MFR = 4.17 \times 10^{-3}$

Figure 5.19. Computed helicity density contours at $f_s = 1.0$; $M_\infty = 0.2$, $\alpha = 40$ deg, $Re_d = 2.81 \times 10^5$.



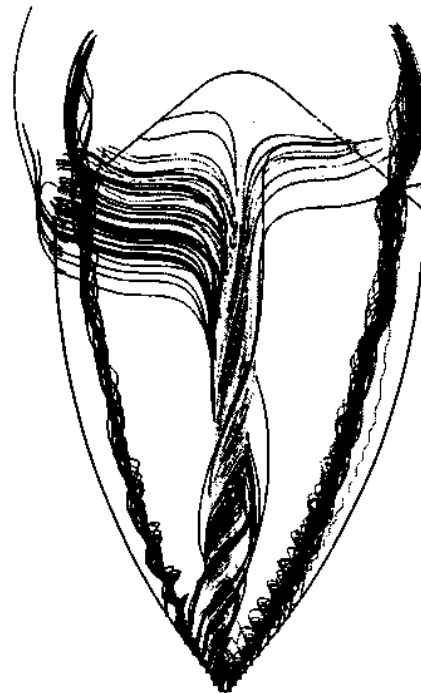
(a) No-blowing



(b) Region I, $MFR = 0.23 \times 10^{-3}$



(c) Region II, $MFR = 1.49 \times 10^{-3}$



(d) Region III, $MFR = 4.17 \times 10^{-3}$

Figure 5.20. Off-surface instantaneous streamlines; $M_\infty = 0.2$, $\alpha = 40$ deg, $Re_d = 2.81 \times 10^5$.

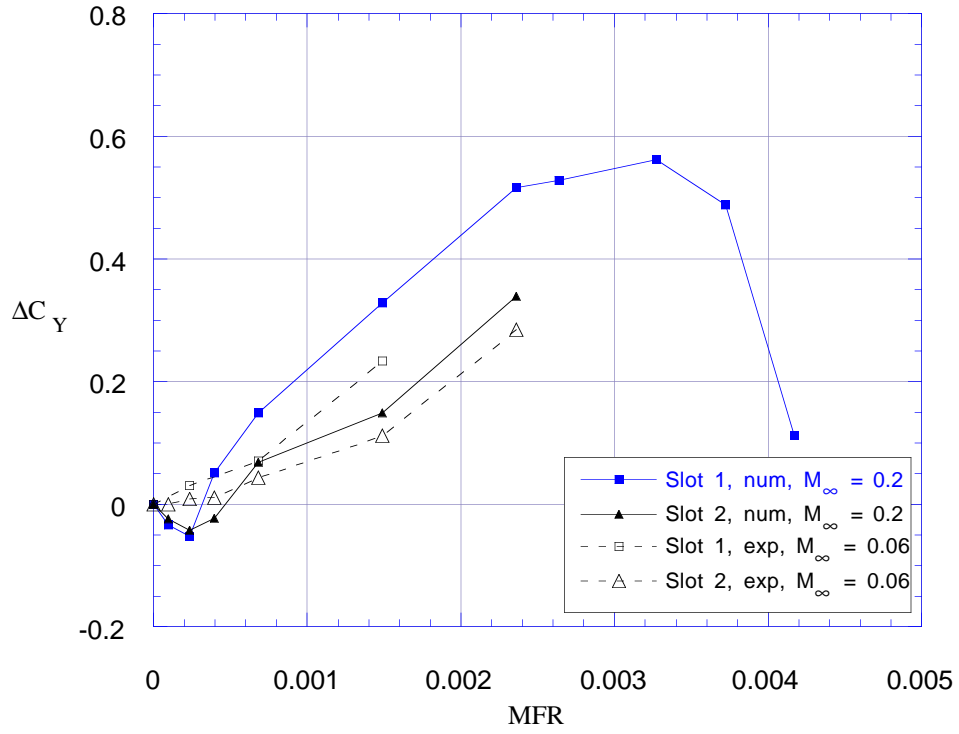


Figure 5.21. Comparison of numerical and experimental incremental side force data for Slot 1 and Slot 2; $Re_d = 2.81 \times 10^5$.

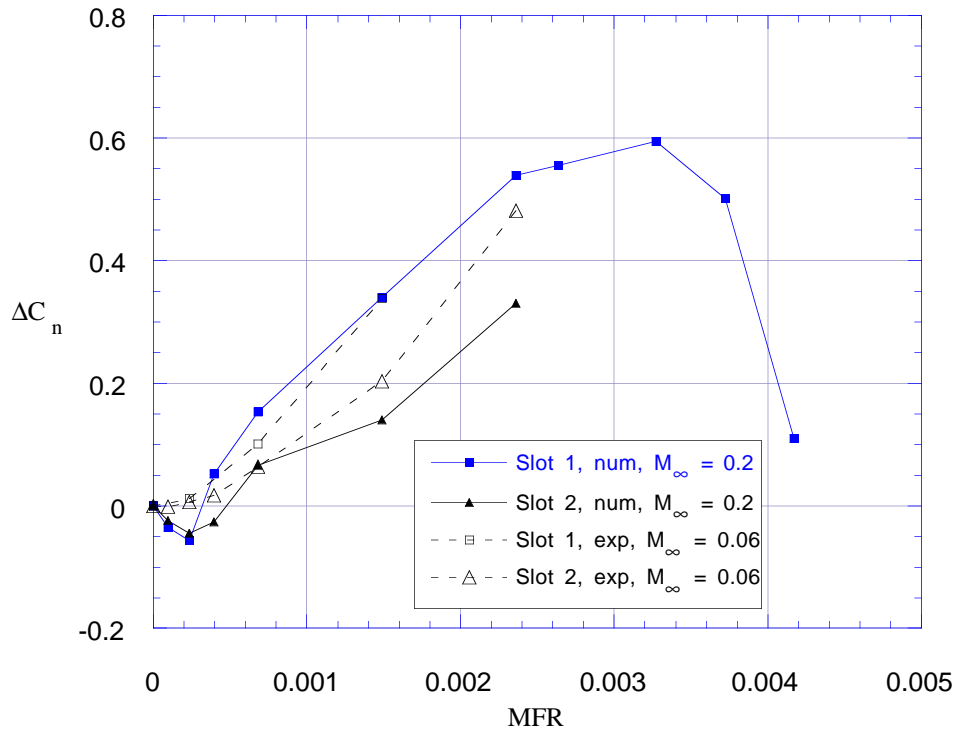


Figure 5.22. Comparison of numerical and experimental incremental yawing moment data for Slot 1 and Slot 2; $Re_d = 2.81 \times 10^5$.

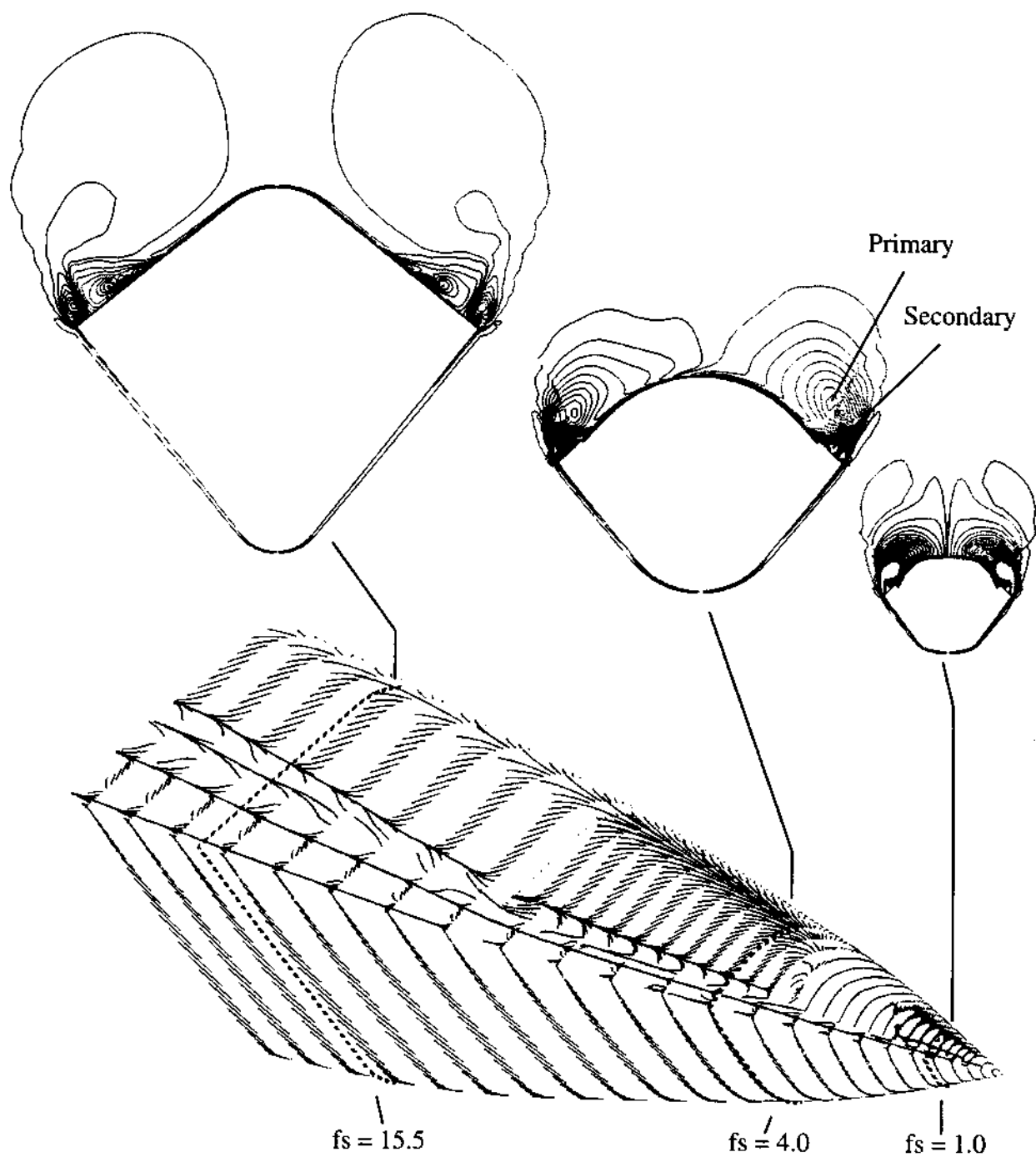


Figure 5.23. Computed surface flow patterns and helicity density contours, Slot 2; $M_\infty = 0.2$, $\alpha = 40^\circ$, $Re_d = 2.81 \times 10^6$, $MFR = 1.49 \times 10^{-3}$.

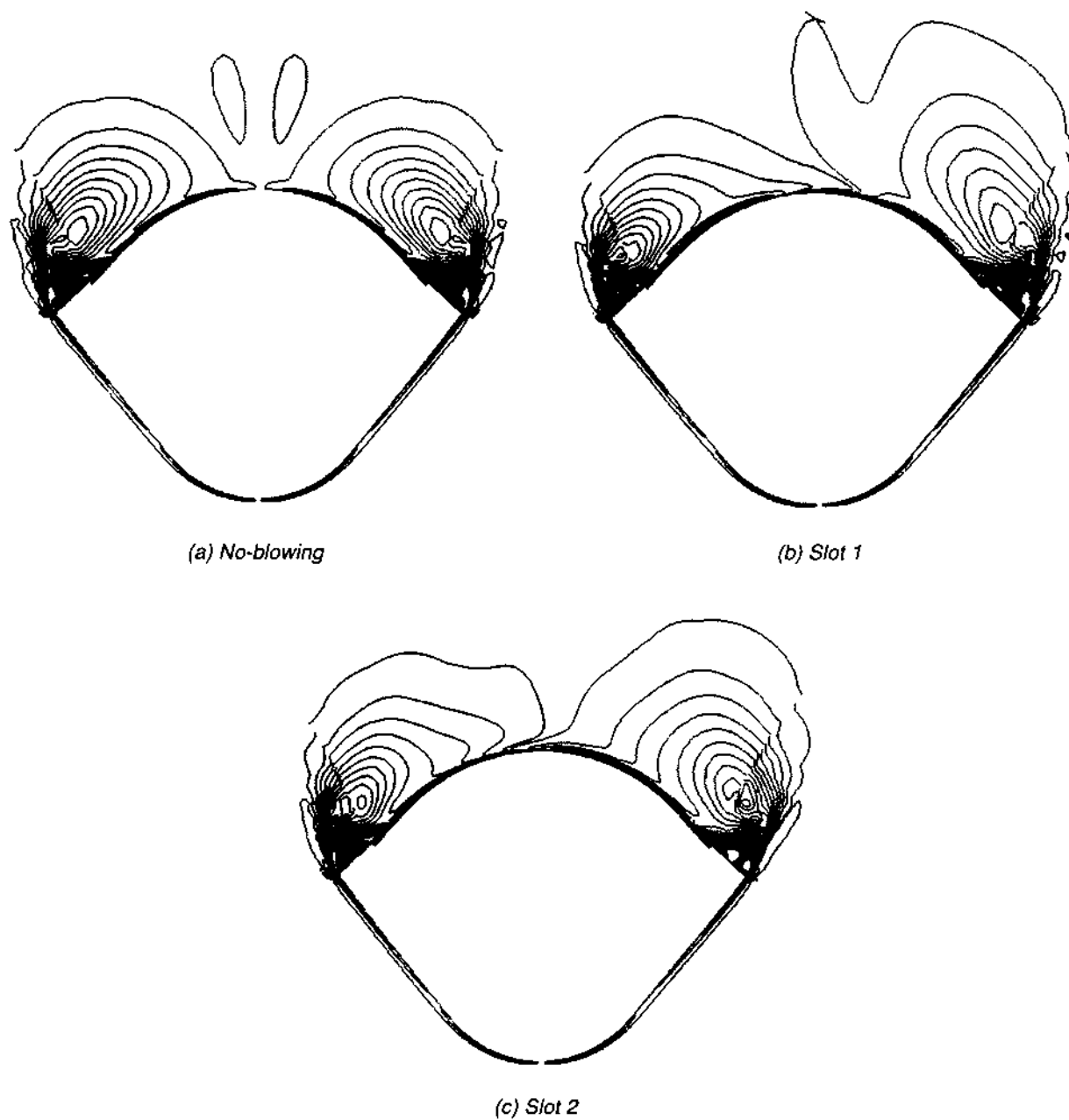


Figure 5.24. Computed helicity density contours at $f_s = 4.0$; $M_\infty = 0.2$, $\alpha = 40$ deg, $Re_d = 2.81 \times 10^5$, $MFR = 1.49 \times 10^{-3}$.

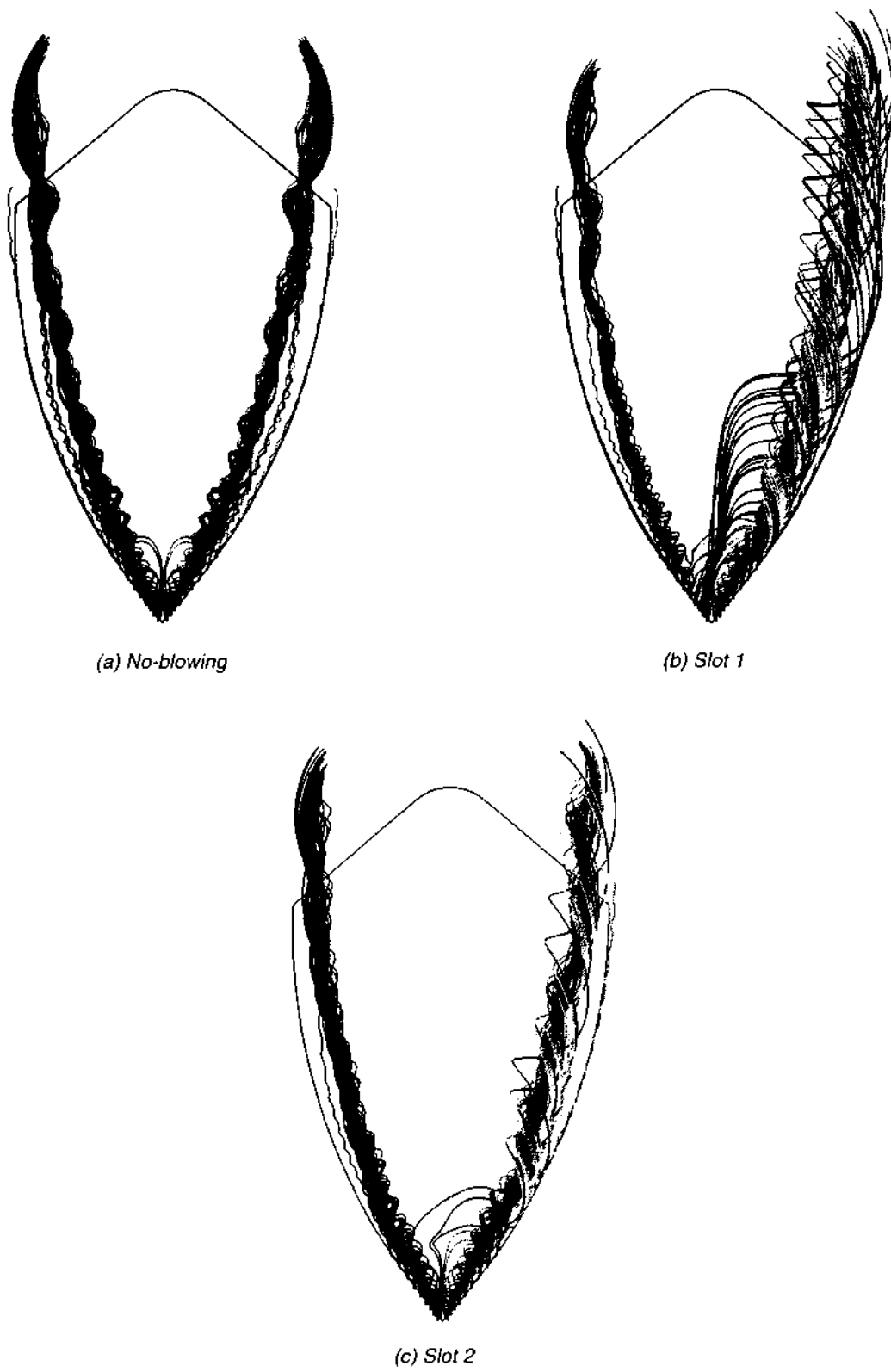


Figure 5.25. Instantaneous streamlines; $M_\infty = 0.2$, $\alpha = 40$ deg, $Re_d = 2.81 \times 10^5$, $MFR = 1.49 \times 10^{-3}$.

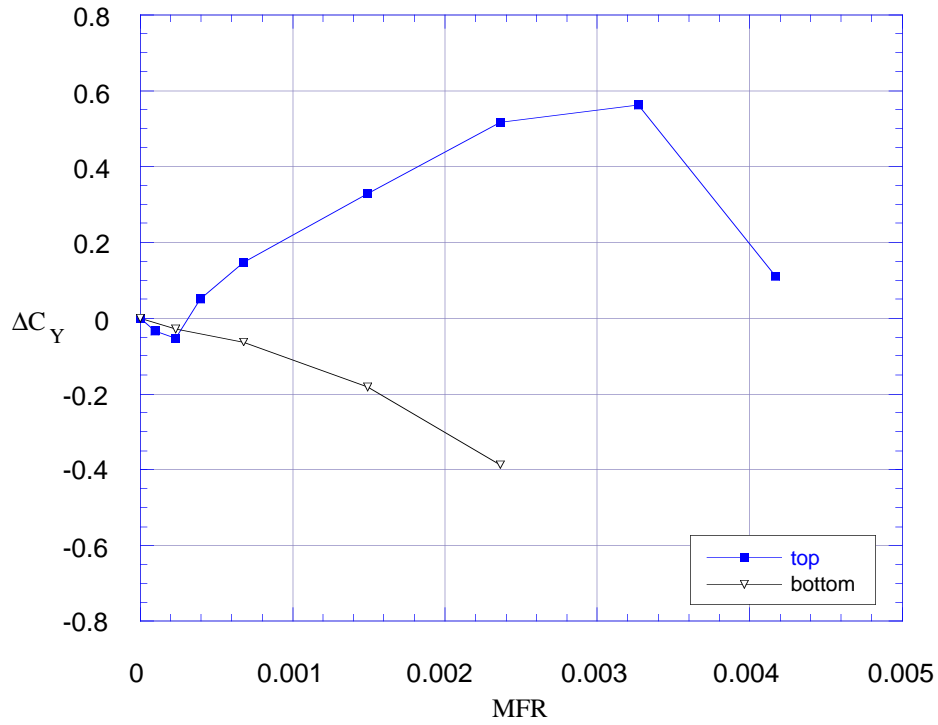


Figure 5.26. Comparison of numerical incremental side force data for blowing from the top surface and bottom surface, Slot 1; $M_\infty = 0.2$, $\alpha = 40$ deg, $Re_d = 2.81 \times 10^5$.

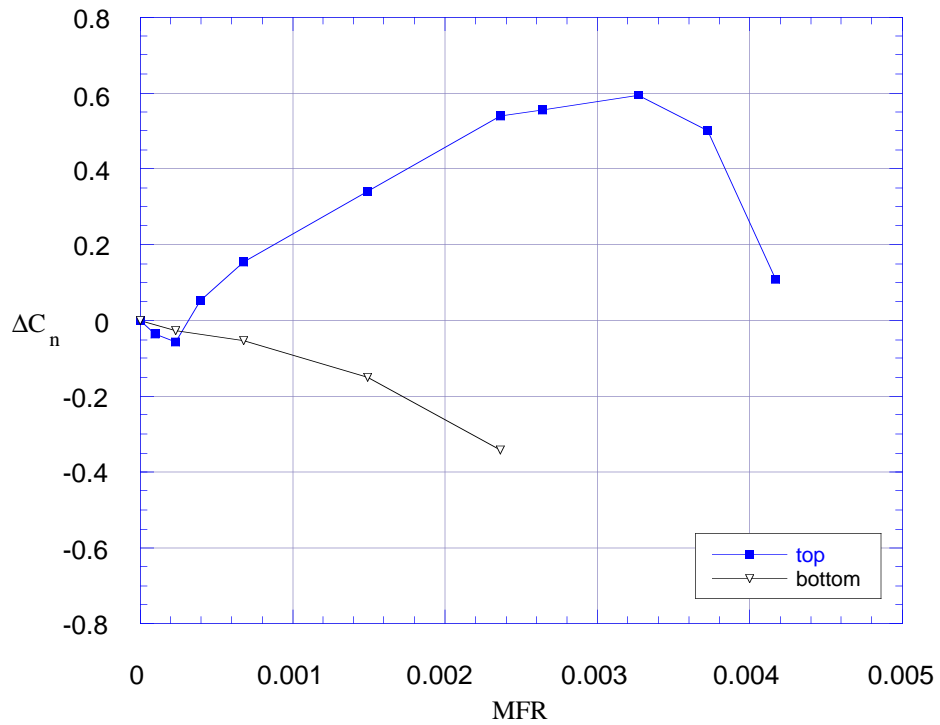


Figure 5.27. Comparison of numerical incremental yawing moment data for blowing from the top surface and bottom surface, Slot 1; $M_\infty = 0.2$, $\alpha = 40$ deg, $Re_d = 2.81 \times 10^5$.

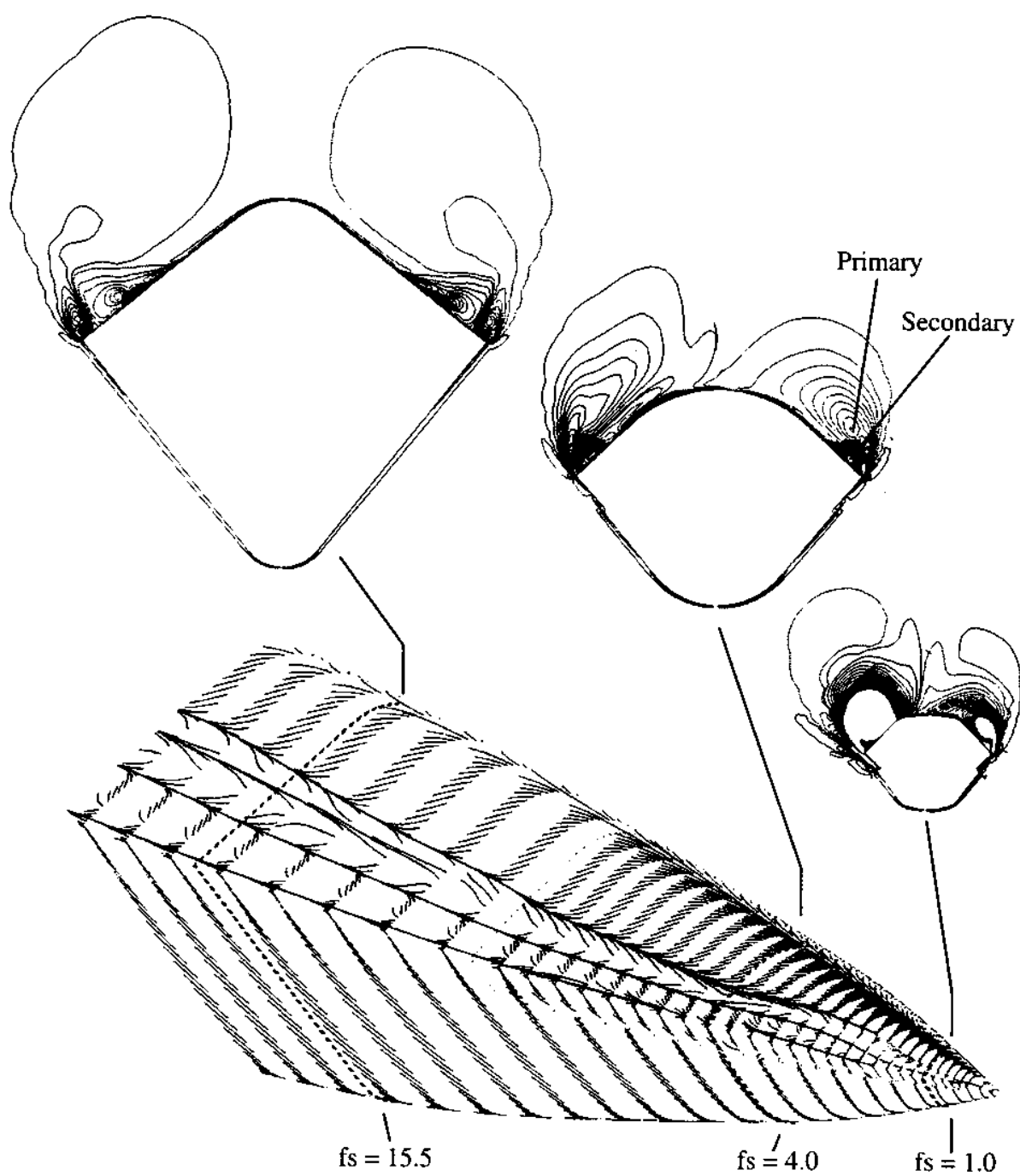


Figure 5.28. Computed surface flow patterns and helicity density contours, bottom blowing; $M_\infty = 0.2$, $\alpha = 40^\circ$, $Re_d = 2.81 \times 10^5$, $MFR = 1.49 \times 10^{-3}$.

REPORT DOCUMENTATION PAGE			Form Approved OMB No. 0704-0188	
Public reporting burden for this collection of information is estimated to average 1 hour per response, including the time for reviewing instructions, searching existing data sources, gathering and maintaining the data needed, and completing and reviewing the collection of information. Send comments regarding this burden estimate or any other aspect of this collection of information, including suggestions for reducing this burden, to Washington Headquarters Services, Directorate for Information Operations and Reports, 1215 Jefferson Davis Highway, Suite 1204, Arlington, VA 22202-4302, and to the Office of Management and Budget, Paperwork Reduction Project (0704-0188), Washington, DC 20503.				
1. AGENCY USE ONLY (Leave blank)		2. REPORT DATE September 1994		3. REPORT TYPE AND DATES COVERED Technical Memorandum
4. TITLE AND SUBTITLE Numerical Analysis of Tangential Slot Blowing on a Generic Chined Forebody			5. FUNDING NUMBERS 505-68	
6. AUTHOR(S) Roxana M. Agosta				
7. PERFORMING ORGANIZATION NAME(S) AND ADDRESS(ES) Ames Research Center Moffett Field, CA 94035-1000			8. PERFORMING ORGANIZATION REPORT NUMBER A-94125	
9. SPONSORING/MONITORING AGENCY NAME(S) AND ADDRESS(ES) National Aeronautics and Space Administration Washington, DC 20546-0001			10. SPONSORING/MONITORING AGENCY REPORT NUMBER NASA TM-108845	
11. SUPPLEMENTARY NOTES Point of Contact: Roxana M. Agosta, Ames Research Center, MS 258-1, Moffett Field, CA 94035-1000 (415) 604-3997				
12a. DISTRIBUTION/AVAILABILITY STATEMENT Unclassified — Unlimited Subject Category 02			12b. DISTRIBUTION CODE	
13. ABSTRACT (Maximum 200 words) A numerical study is performed to investigate the effects of tangential slot blowing on a generic chined forebody. The Reynolds-averaged, thin-layer, Navier–Stokes equations are solved to obtain the high-angle-of-attack viscous flow field about a generic chined forebody. Tangential slot blowing is investigated as a means of forebody flow control to generate side force and yawing moment on the forebody. The effects of jet mass flow ratios, angle of attack, and blowing slot location in the axial and circumferential directions are studied. The computed results are compared with available wind tunnel experimental data. The solutions with and without blowing are also analyzed using helicity density contours, surface flow patterns, and off-surface instantaneous streamlines. The results of this analysis provide details of the flow field about the generic chined forebody, as well as show that tangential slot blowing can be used as a means of forebody flow control to generate side force and yawing moment.				
14. SUBJECT TERMS Chined forebody, Tangential slot blowing, Outward blowing			15. NUMBER OF PAGES 62	
			16. PRICE CODE A04	
17. SECURITY CLASSIFICATION OF REPORT Unclassified	18. SECURITY CLASSIFICATION OF THIS PAGE Unclassified	19. SECURITY CLASSIFICATION OF ABSTRACT	20. LIMITATION OF ABSTRACT	